AD NUMBER:	AD0817973

LIMITATION CHANGES

TO:

Approved for public release; distribution is unlimited.

FROM:

Distribution authorized to U.S. Gov't. agencies and their contractors; Administrative/Operational Use; 1 Jun 1967. Other requests shall be referred to Air Force Inst. of Technology, Wright-Patterson AFB, OH

AUTHORITY

AFIT ltr 22 Jul 1971

AIR FORCE INSTITUTE OF TECHNOLOGY

AIR UNIVERSITY
UNITED STATES AIR FORCE

AN INVESTIGATION OF THE DEBRIS CLOUD
PRODUCED BY THE IMPACT OF SPHERES
ON THIN METAL SHEETS

THESIS

GSF/Mech 67-1   Donald Albert Carey
Captain   USAF

SCHOOL OF ENGINEERING

WRIGHT—PATTERSON AIR FORCE BASE, OHIO

AN INVESTIGATION OF THE DEBRIS CLOUD
PRODUCED BY THE IMPACT OF SPHERES
ON THIN METAL SHEETS

THESIS

GSF/Mech 67-1   Donald Albert Carey
                 Captain   USAF

AN INVESTIGATION OF THE DEBRIS CLOUD

PRODUCED BY THE IMPACT OF SPHERES ON THIN METAL SHEETS

THESIS

Presented to the Faculty of the School of Engineering of

the Air Force Institute of Technology

Air University

in Partial Fulfillment of the

Requirements for the Degree of

Master of Science

By

Donald Albert Carey, B.S.
Captain   USAF

Graduate Space Facilities

June 1967

Preface

This report is a result of my attempts to contribute
to the development of the theory of the debris cloud for-
mation caused by hypervelocity spheres impacting thin
metal sheets. The area of investigation is confined to
the physics of the debris cloud produced by such impacts
in the belief that fundamental facts may be established
about the behavior of the sphere and metal sheet upon
impact.

The author is deeply indebted to many persons who
gave valuable assistance in the accomplishment of this
study. I wish to thank Mr. Alan K. Hopkins of the Air
Force Materials Laboratory who assisted greatly with
suggestions and made all necessary equipment available;
Mr. Hallock F. Swift of the University of Dayton Research
Institute for his inspiration, imagination, and ingenuity
which were instrumental in the guidance of the investigation;
the faculty members of my thesis committee for their en-
couragement and interest; the gun crew and the technicians,
Lew Shiverdecker, Ed Strader, and Mark Hurst, for meeting
exacting experimental parameters in a short period of time;
and my wife, Christa, for her encouragement and typing of
the report.

<div align="right">Donald A. Carey</div>

Contents

Page

List of Figures

List of Tables

AN INVESTIGATION OF THE DEBRIS CLOUD PRODUCED BY THE IM-
PACT OF SPHERES ON THIN METAL SHEETS

Capt. Donald A. Carey

Abstract of Thesis:

An experimental investigation of the debris cloud
produced by the impact of 1/8" diameter spheres of cop-
per and cadmium on 1/16" sheets of like materials was
conducted. Calculations of the energy delivered to cop-
per witness plates by solid and liquid phases of the
debris cloud were made using volume-energy relationships.
Velocity of the cloud front was determined through use
of sequential flash x-rays. Phases of the cloud were
determined by employing a combination of photographic,
radiographic, and crater measurement techniques. Varia-
tions in the phase of the cloud with three selected velo-
cities for each bumper-projectile combination were com-
pared with the predicted phase in the velocity range of
23000 to 3000 ft/sec. Energy, energy density, momentum,
and mass delivered to witness plates are determined as
a function of cone angle.

AN INVESTIGATION OF THE DEBRIS CLOUD
PRODUCED BY THE IMPACT OF SPHERES ON THIN METAL SHEETS

I. Introduction

Man is preparing to explore the Moon and planets.
Space travelers will be exposed to many hazards uncommon
to the Earth's environment. Prominent among these is the
danger of spacecraft collisions with meteoroids and micro-
meteoroids. This study will concentrate upon one of the
devices proposed for spacecraft protection during the
extended flights required for interplanetary and orbital
flights.

Background

The "meteoroid bumper", as first proposed by F. L.
Whipple, is somewhat of a misnomer (Ref 26). Meteoroids
are not deflected or prevented from striking a spacecraft
hull in the sense that an automobile bumper is intended.
Rather, the "bumper" is a sacrificial shield employed to
disrupt the point loading effect of the impact of a fast
moving particle. The bumper is shown in Figure 1. A thin
metallic sheet is spaced a few inches from the spacecraft
hull. An incoming meteoroid striking this "bumper" sheet
experiences severe shock loading, and disintegrates if
shock pressures exceed the strength of the projectile.
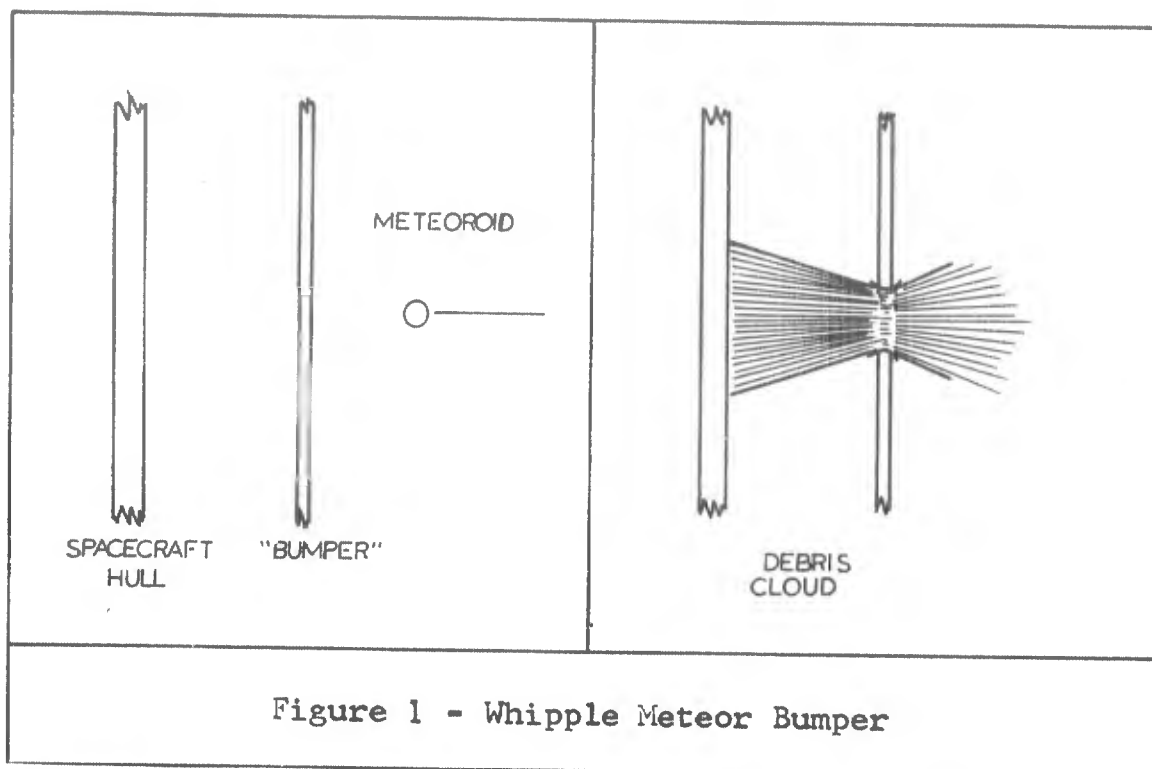
Figure 1 - Whipple Meteor Bumper

The debris from such an impact, including material from
both the meteoroid and the bumper, proceeds on to the
spacecraft hull in an expanding "bubble", approximating
an ellipsoid of revolution at full development. Hopefully,
the spacecraft hull will not be penetrated by the debris.
The impact has been changed drastically from that of a
single relatively high energy projectile striking a loca-
lized area, to many small lower energy particles impacting
a larger area.

The bumper concept has received much attention in the
laboratory and has been demonstrated to be feasible (Ref
12 and 18). However, major difficulties are involved in
the laboratory simulation of meteoroid velocities, com-
position, and densities. Meteoroid velocities are esti-
mated at 11 to 72 km/sec with respect to the Earth (Ref

19:1). The estimates of meteoroid densities have ranged
from .05 gm/cm^3 to 8.5 gm/cm^3. The flux rates for ex-
pected meteoroid impacts of given masses have and are now
being determined by satellite-borne experiments. Although
a complete knowledge of the meteoroid environment is un-
available, several design criteria have been adopted. For
an Apollo mission of 14 days, protection should be provided
against meteoroid masses up to 1.48×10^{-3} grams for a
0.999 probability of no puncture (Ref 19:2). This was
based on an isotropic flux-mass relationship published
in 1965 (Ref 3).

Several problems limit the experimental determination
of the optimum design for bumper configuration for an
Apollo or other extended mission. Mass acceleration de-
vices are presently limited to less than 15 km/sec velo-
cities for projectiles of known mass and configuration
(Ref 12:1584). Also, the high acceleration rates achieved
during launch of such projectiles may permanently deform
low density materials. The experimental approach, then,
has been to accelerate high density materials (usually
metallic) to the maximum attainable velocities in the hope
of achieving energies comparable to the encounter of a
low density, high velocity particle with a spacecraft.
The critical mass of the meteoroid in the Apollo design
study, for example, corresponds to a spherical meteoroid
1.78 mm in diameter with a density of 0.5 g/cc. This may

3

be approximated in mass by an aluminum sphere (density 2.7 gm/cc) of 1.02 mm diameter (Ref 19:2). Laboratory efforts have concentrated on the determination of optimum projectile, bumper, and spacing combinations as well as on providing data necessary for the development of an impact model that will fully explain the experimental results. This study of the dynamics of the debris cloud is intended to help in the development of an impact model.

The impact of a meteoroid (simulated by a metallic sphere) on a thin sheet of the same material is depicted in Figure 2.

| AT IMPACT | SPALL FORMATION | DEVELOPED CLOUD |

Figure 2 - Sequence of Perforation of a Thin Sheet
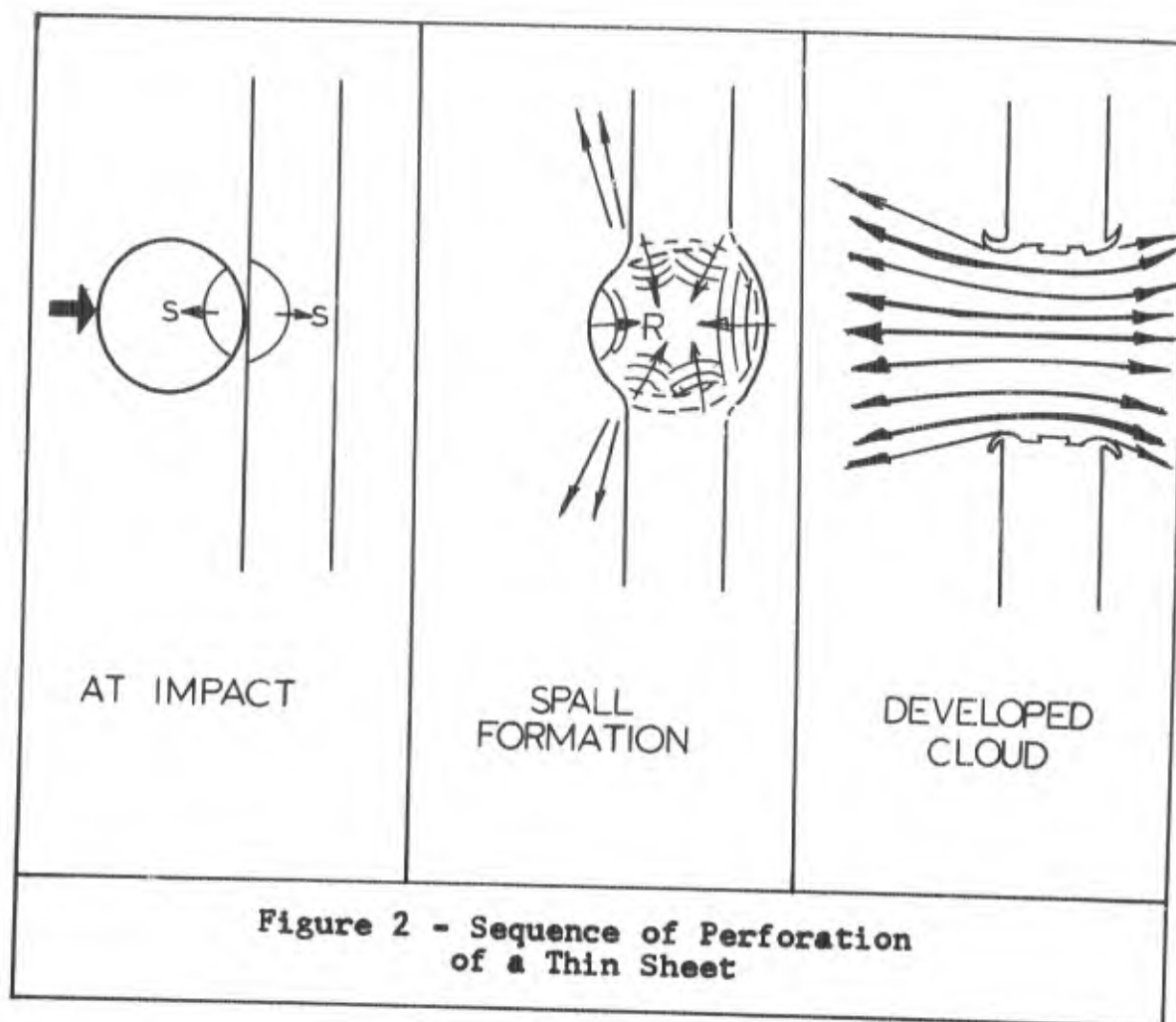
At impact, shock waves are propagated into the bumper material and into the projectile. When material behind the shocks is compressed to such pressures that material strengths are greatly exceeded, the flow of material may be regarded as that of an inviscid fluid (Ref 27:85). The shock waves in the bumper and projectile propagate at velocities S until they strike the rear surface of the bumper and surface of the sphere, respectively. The shocks are reflected from these free surfaces as tension or rarefaction waves. Relaxation of the compressed shocked states begins at this point. The rarefaction waves move at the speed of sound in the shocked material. Particle velocities will be in the opposite direction to the rarefaction wave. In the meantime, if the tensile stress produced by the rarefaction exceeds the material fracture strength, rupture occurs. Each element of a projectile-bumper combination is shocked to a degree dependent upon the impact energy and then is brought to ambient pressure conditions by relaxation waves. The kinetic energy of impact is assumed to be partially transferred into the kinetic energy of the shattered bumper-projectile fragments in the affected region, and partially into residual heating of this same region.

Consideration of the conservation of mass, momentum, and energy across the shock front leads to the following equations:

$$\rho_0 U_s = \rho_1 (U_s - U_p) \qquad (1)$$

$$P_1 - P_0 = \rho_0 U_s U_p \qquad (2)$$

$$E_1 - E_0 = \frac{1}{2}(P_1 + P_0)(V_0 - V_1) \qquad (3)$$

where U_s = shock front velocity

ρ_0 = density in unshocked material

ρ_1 = density in shocked material

U_p = particle velocity behind the shock

P_0 = pressure in unshocked material

P_1 = pressure in shocked material

E_0 = specific internal energy in unshocked material

E_1 = specific internal energy in shocked material

V_0 = specific volume of unshocked material

V_1 = specific volume of shocked material

These are expressions for conservation of mass, momentum, and energy across the shock front (Ref 10:8). When equation (3) is combined with the equation of state of the material, a relation between P and V is obtained. In the P, V plane, this expression (known as the Rankine-Hugoniot curve) defines a unique curve of all, P, V, E states attainable by a single shock compression from an initial state P_0, V_0, E_0 (Ref 5:49). Equation (3) appears in plotted form in Figure 3. Since pressures on the order of a few megabars may be achieved, P_0 is negligible, and will be assumed to be zero.
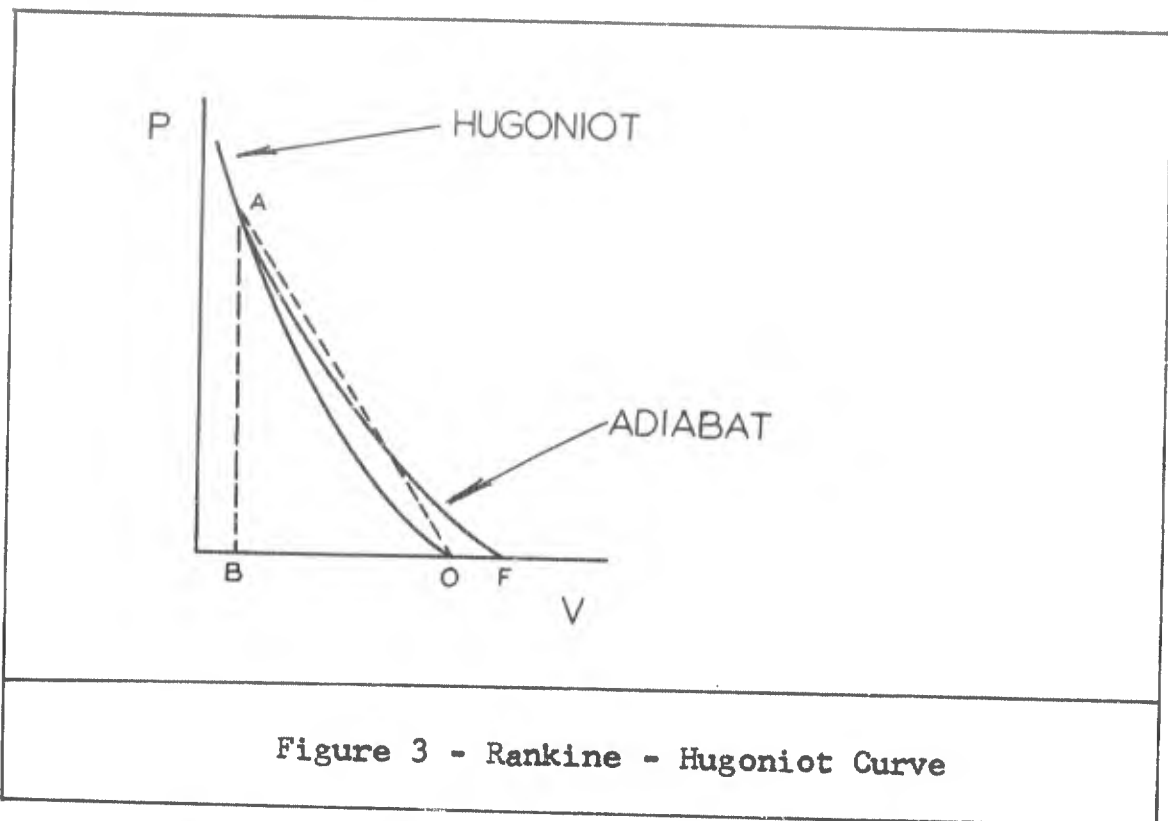
Figure 3 - Rankine - Hugoniot Curve

Equation (3) expresses the energy acquired through shock compression as the area of triangle OAB. The release of the material by the rarefaction wave is an isentropic process indicated by the adiabat AF. Thus, the energy returned to the material in pressure-volume expansion work is represented area under the adiabat curve AF. This reversible work is less than the energy acquired by the material in shock compression, so the total entropy of the system has been increased. As the shock strength is increased, the difference in these energies will increase. The entropy increase is manifested by residual heating of the material. The greater the shock pressures attained then, the more residual heating possessed by the shocked material. In a thin metal sheet, if sufficient

shock strengths are achieved, melting, vaporization or superheated vapor states could be present in the debris cloud.

Purpose

The purpose of this study was to develop a technique for determining the state of the debris cloud at varying peak pressures for a given bumper-projectile combination. This technique was used to determine the velocity of the cloud front as a function of cone angle. The energy, energy density, mass, and momentum delivered witness plates by the solid and liquid phases of the cloud at two different spacing distances are also determined as a function of cone angle. Since present day launch techniques limit velocities to the very low range of meteoroid velocities, a complete understanding of debris cloud formation may permit speculative extrapolations of resulting spacecraft damage by the impacts of meteoroids.

II. Procedure and Experimental Method

Approach to the Problem

To develop the technique outlined in the Introduction, a pilot program was conducted. The details of the experiments making direct contributions to this study are contained in Appendix B. The approach took advantage of several phenomena observed in the preliminary tests. Metallic vapors appeared to be transparent to X-rays. These same vapors can be photographed. Simultaneous radiographs and photographs might reveal the presence of solid liquid, and/or vapor states in the cloud. To aid this approach, it was decided to pass the debris cloud over a sharp barrier. Solid and liquid particles would move in straight lines past such a barrier, while vapors in the cloud might deviate from straight line travel and permit detection of this phase. It was also thought that gaseous phases would inflict minimal damage on witness plates placed in the debris cloud as opposed to the cratering effects of liquid and solid phases. Finally, evidence of liquid droplets might be indicated by a dimishing crater size resulting from impacts of these particles with plates having increased spacing from the bumper. This approach required that any tumbling motion experienced by cloud fragments would be more likely to break up liquid droplets than solid particles.

It should be noted here, however, that no available ex-
perimental data suggests that the particles do experience
tumbling.

The second objective involved measuring the maximum
velocity attained by the cloud front as a function of cone
angle. This was accomplished by taking sequential radio-
graphs a specified time interval apart, and superimposing
radiographs on a grid of known dimensions. The technique
is depicted in Figure 4. The two curved lines represent
the cloud configuration at known times after impact. Wit-
ness plates were placed in the cloud trajectory to inter-
cept portions of the debris at two known distances from the
bumper (see Figure 5). The patterns of impact on these
plates contained craters of varying size and shape. The
craters near the cloud trajectory symmetry axis were gener-
ally hemispherical, but as the distance from the axis in-
creased, a point was noted beyond which the craters did not
approximate hemispheres. Lines may be constructed from
these limits of hemispherical cratering on the witness
plates placed at different distances from the bumper. Since
the particles which made the craters traveled in straight
paths, the constructed lines fall on particle trajectories.
The intersection of these lines with the projectile trajec-
tory locates the point Q in Figure 4. For normal impacts,
Q is the vertex of a right circular cone. The axis of
symmetry coincides with the projectile trajectory. Lines
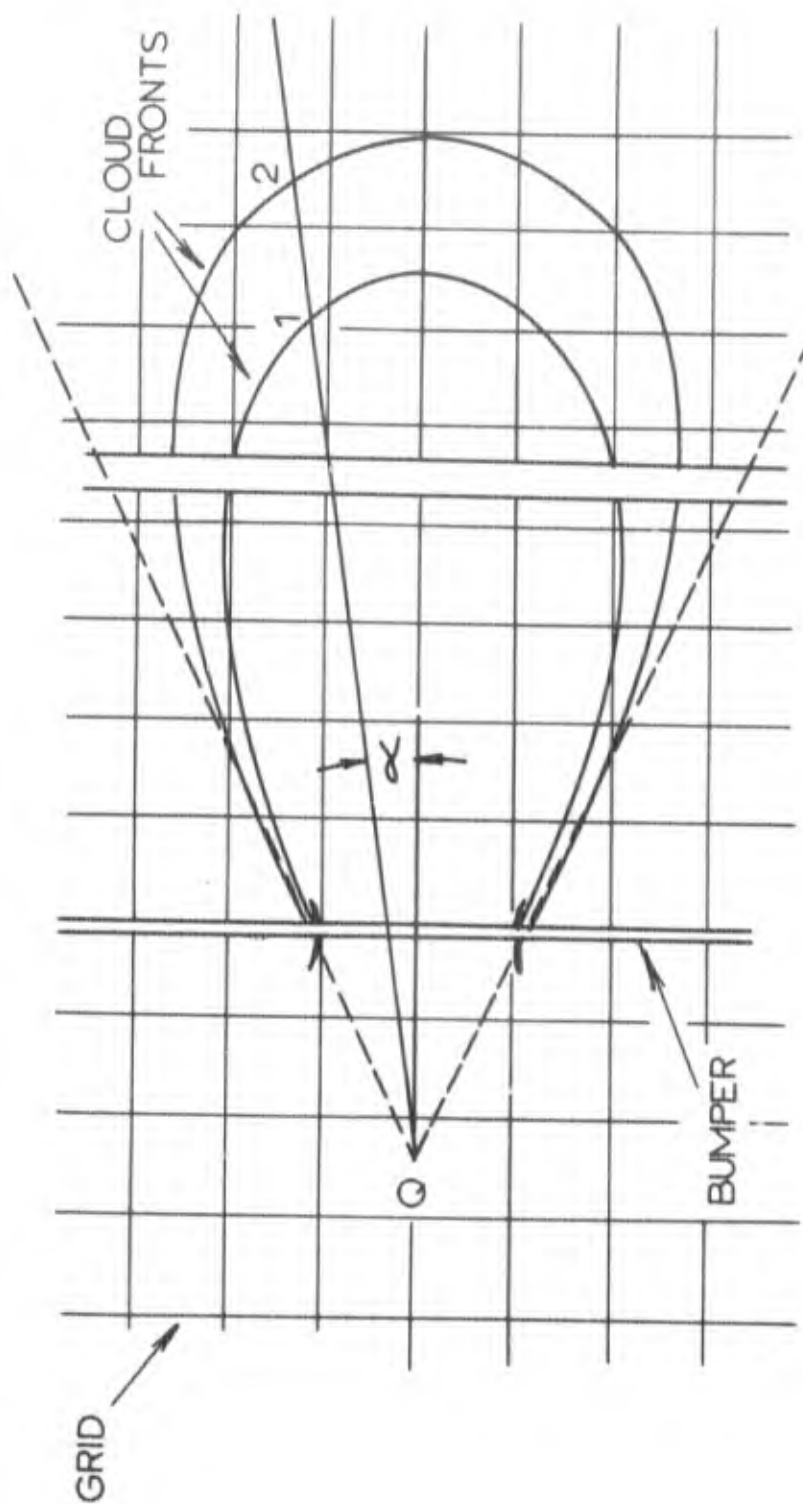
Figure 4 - Sequential X-ray Technique
of Computing Cloud Velocity

11
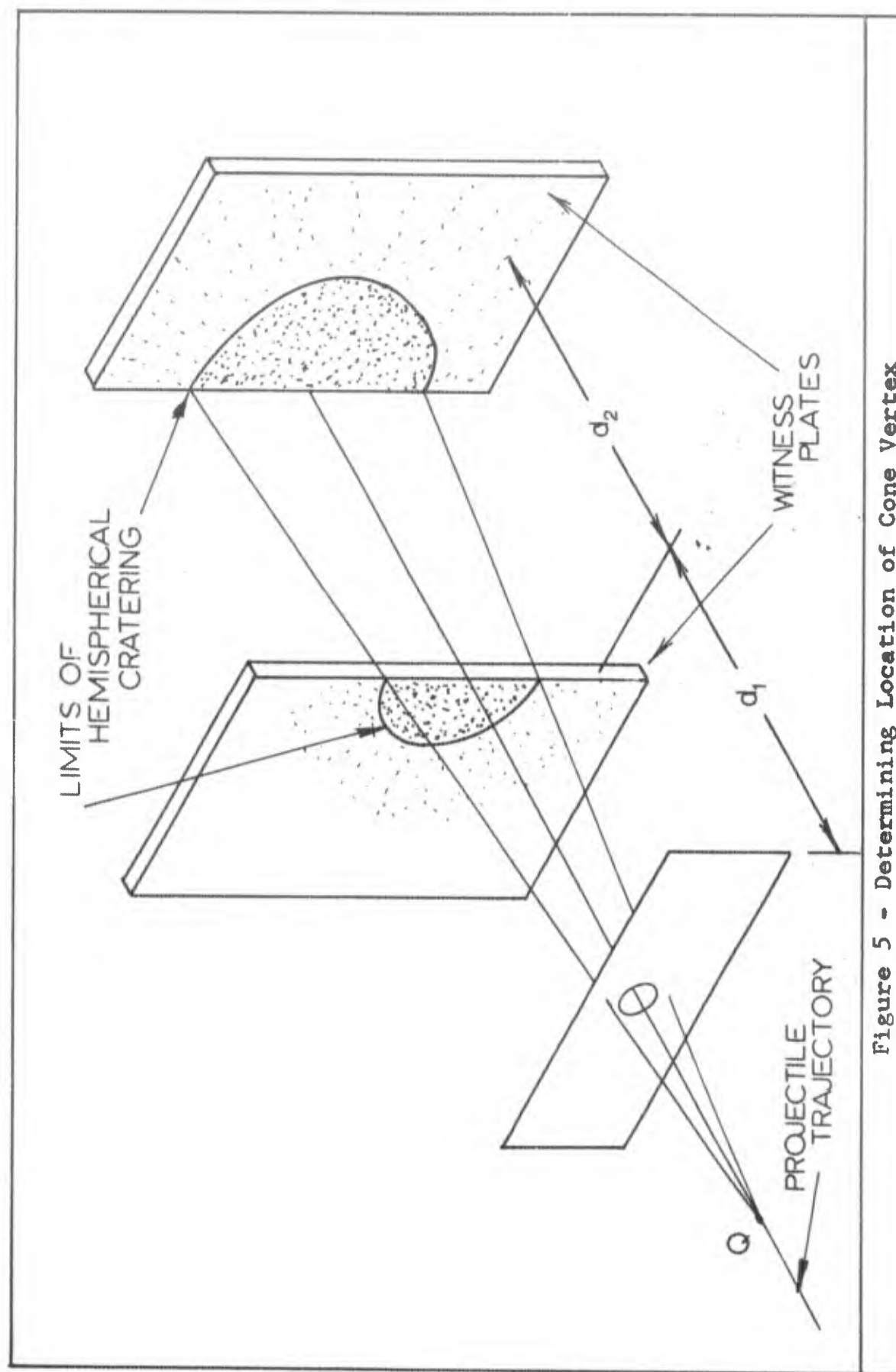
Figure 5 - Determining Location of Cone Vertex

were constructed from Q through the cloud fronts, along particle trajectories at varying values of cone angle α. The distance between the cloud fronts was measured using the grid background. Since the time of particle travel was known, velocity of the cloud front as a function of cone angle was determined.

Thirdly, energy delivered to the witness plates by solid and liquid phases of the cloud was measured. The key to this measurement was a relationship between the energy of an impacting projectile and the volume of the resulting crater. A data base line was established by firing projectiles of known mass and velocity at thick targets of the same material as the witness plates. The volumes of the craters were measured by a technique utilizing penetrating oil (see Appendix C). The relationship of volume and energy was established for a projectile-target combination. The volumes of the craters on the witness plates were calculated by first measuring the crater diameters. Assuming that the craters were hemispherical, the diameters were used as a basis for computing volume. The energy of the impacting particle was determined from the previously established volume-energy relationship. Energy delivered to areas of the witness plates were calculated by adding the energies corresponding to the craters within that area.

Finally, the mass and momentum as a function of cone

angle was determined. Calculations were made by combining the results of the energy and velocity determinations.

Application of the Technique

The peak pressures generated by the collision of spheres with metal sheets may be varied by varying the impact velocities. The debris cloud resulting from normal impacts of spheres of two selected materials, copper and cadmium, upon like material bumpers was examined for state variation with differing impact velocities. These materials were selected because they have greatly differing thermal properties but almost identical densities. The spheres impacted like metals, so that all the debris produced would be the same material. Maiden tabulated the peak pressures required to melt copper and cadmium, and to vaporize cadmium (see Table I).

| Material | Melting Temp(^{o}C) | Vaporization Temp (^{o}C) | Pressure (Mb) | | |
			Incipient Melting	Complete Melting	Vaporization
Cadmium	321	767	0.4	0.46	0.8
Copper	1,083	2,336	1.4	1.5	-

(Ref 19:6)

Shock Heating Properties

Table I

No data was available on the pressure required to vaporize copper. A graphical technique was used to compute the impact velocities required to achieve pressure which could

14

change the state of the debris cloud. The method is
presented in Appendix C. The results of the calculations
are presented in Table II.

Materials	Solid		Liquid		Vapor	
	ft/sec	km/sec	ft/sec	km/sec	ft/sec	km/sec
Cd-Cd	6,500	1.98	10,000 6,500	3.05 1.98	11,000	3.35
Cu-Cu	14,300	4.35	20,000 15,000	6.10 4.57	-	-

Computed Velocities and Expected Cloud Phases

Table II

The velocity ranges determined give the expected states of
the debris cloud. For example, a Cd-Cd impact at 8,000
ft/sec should produce liquid and solid debris while a
16,000 ft/sec impact should have solid, liquid, and gaseous
debris. Since the pressure required to vaporize copper
was not available, it was decided to fire a copper sphere
at a copper bumper at the maximum velocity of the facility
(approximately 23,000 ft/sec). The pressures generated in
such an impact are 2.78 Mb (see Appendix C). The effect
was expected to be more melting than occurred in the 15-
20,000 ft/sec range. Bjork lists impact velocities re-
quired by impacts of copper and cadmium on like materials
to produce a melted phase (see Table III). Note that peak
pressures for incipient melting of cadmium and complete

melting of copper differ from those listed in Table I.
However, the impact velocity ranges computed in Table II
for melting include those listed by Bjork.

Material	Shock Pressure (Mb) Incipient	Complete	Impact Velocity (km/sec) Incipient	Complete
Cadmium	0.33	0.46	1.90	2.40
Copper	1.40	1.84[a]	4.36	5.2[a]

[a] - Estimated   (Ref 2:1)

Shock Melting Properties

Table III

The firing mode of the gun was modified as described in
Appendix A to achieve the different velocity ranges.

Thick Target Tests. To establish the volume-energy
relationship, 1/8" spheres of copper and cadmium were fired
into 4" diameter copper billet material. At least one
shot was fired at each of the velocity ranges listed in
Table II. The test numbers and the impact velocities are
shown in Table IV.

Shot No.	Projectile Diameter	Target Thickness	Velocity ft/sec
2197	1/8" Cu	2.0" Cu	22,404
2203	1/8" Cu	1.5" Cu	16,147
1021	1/8" Cu	1.0" Cu	7,064
2196	1/8" Cd	1.5" Cu	22,523
2207	1/8" Cd	1.5" Cu	13,593
1015	1/8" Cd	1.0" Cu	5,901
1018	1/8" Cd	1.0" Cu	4,792

Results of Thick Target Tests

Table IV

Bumper Target System. The test setup for the debris
cloud study is illustrated in Figure 6. The bumper was a
1/16" thick plate of copper or cadmium. A "cloud splitter"
plate was spaced 1-3/8" from the bumper. This plate was
made of 1/4" steel. A slot 4 inches long and 1/4" wide
was cut in the plate to permit a portion of the cloud to
pass through. Two additional 1/4" steel plates were po-
sitioned normal to the range axis to intercept the sliced
cloud (see Figure 7). The triangular shaped plate was
positioned 5-3/16" from the bumper to intercept the right
half of the debris slice. The T-shaped plate was spaced
9-61/64" from the bumper and intercepted the left half of
the sliced cloud. The dotted lines indicate positions at

17
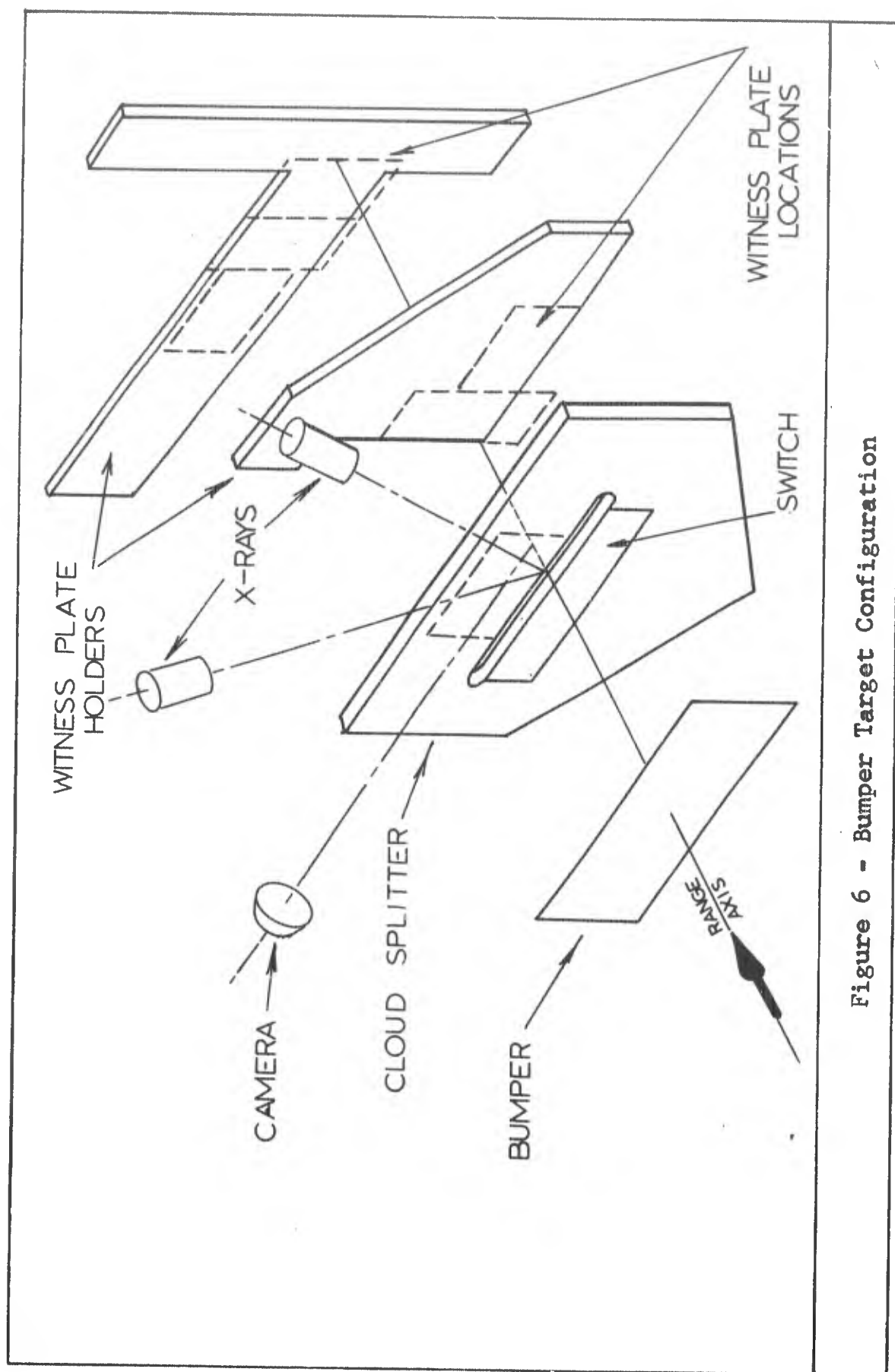
Figure 6 - Bumper Target Configuration
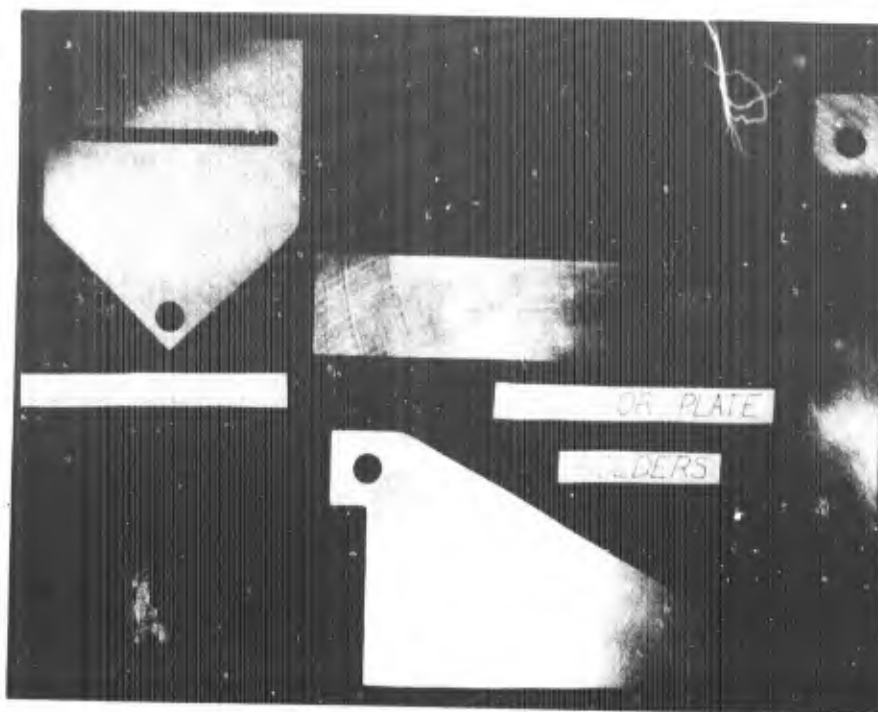
Figure 7 - Witness Plate Holders
and Cloud Splitter
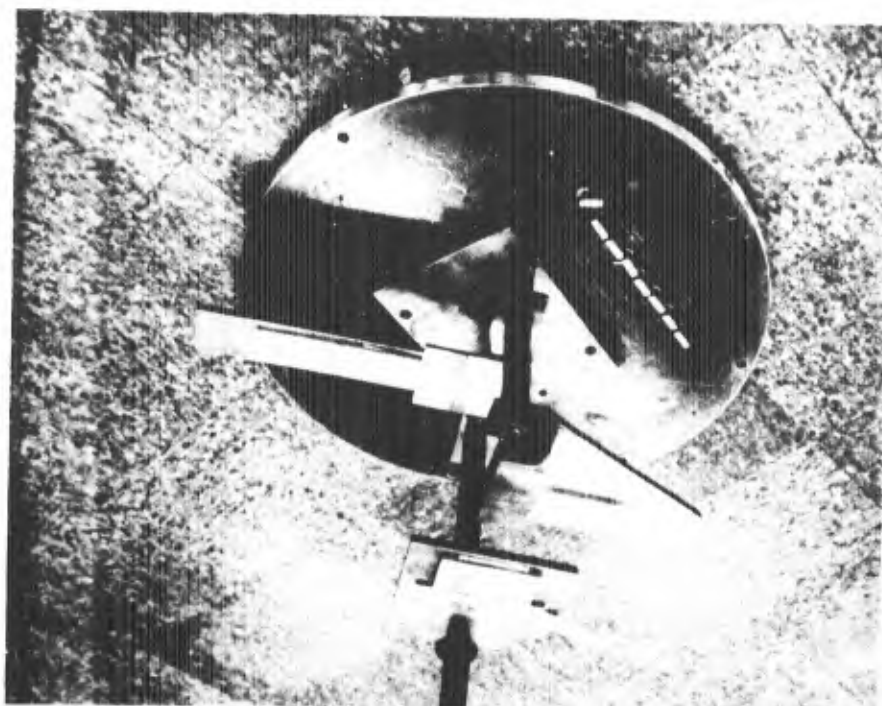
Figure 8 - Mounted Target

which 3/16" thick copper witness plates were placed. The
target system was mounted on 1/2" All-thread holders
(see Figure 8) and aligned with the range axis by an op-
tical sighting system. The target was aligned so that the
range axis passed through the center of the splitter slot.
The advantage of this setup was that only the bumper and
witness plates required changing between test shots. The
steel plates were not removed from the mounts between
shots, so target geometry remained constant. Two 105 KV
X-ray sources were positioned as shown in Figure 6. The
axes of the X-ray heads intersected the range axis in the
plane of the cloud splitter. The cloud splitter presented
a minimum profile in this configuration. Film holders
were placed normal to the tube axes 4" from the range
axis (see Figure 9). A 6-1/2" x 15" port was cut in the
top of the target box. Placement of the X-ray heads was
made so that the edge of the port allowed each X-ray
source to expose only one film (see Figure 9 and 10).

Optical Camera System. An image converter camera
was positioned to photograph the cloud slice emerging
through the splitter plate. A spark-gap light source
was synchronized with the 10 nanosecond shutter speed.
The field of view of the camera was 3" along the range
axis.

The entire experimental instrumentation setup is
shown schematically in Figure 11. (For details of equip-
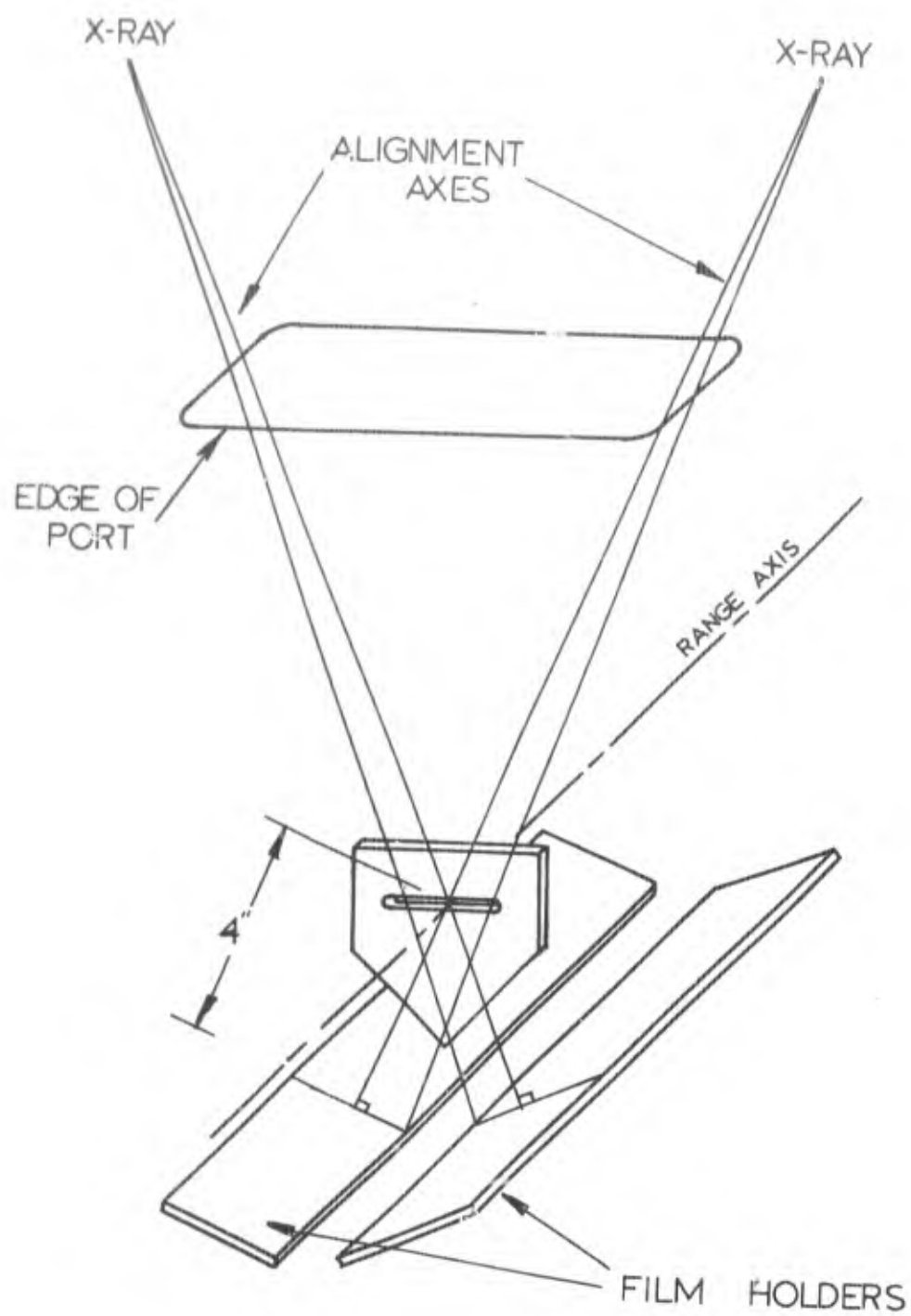
Figure 9 - X-Ray Geometry
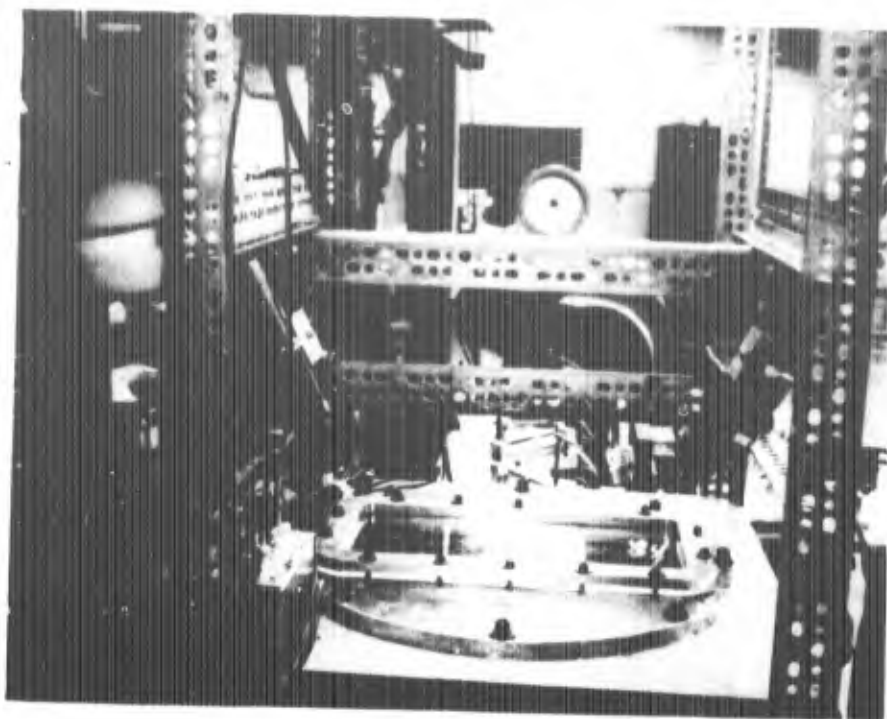
Figure 10 - X-Ray Heads Mounted
on Top of Target Box

ment mentioned here, (see Appendix A). An image converter-
camera checked projectile integrity prior to impact. After
projectile-bumper impact, the debris cloud impacted the
switch on the face of the splitter plate which initiated
two time delay generators. One was set at a short time
delay from cloud-switch impact and allowed the cloud to
advance approximately 1" through the splitter slot before
X-ray 1 fired. The second generator was set for a longer
time after switch impact to allow cloud advancement an
additional inch before X-ray 2 and the second image con-
verter camera were triggered simultaneously. The camera-
winker system records the time sequence of events as des-
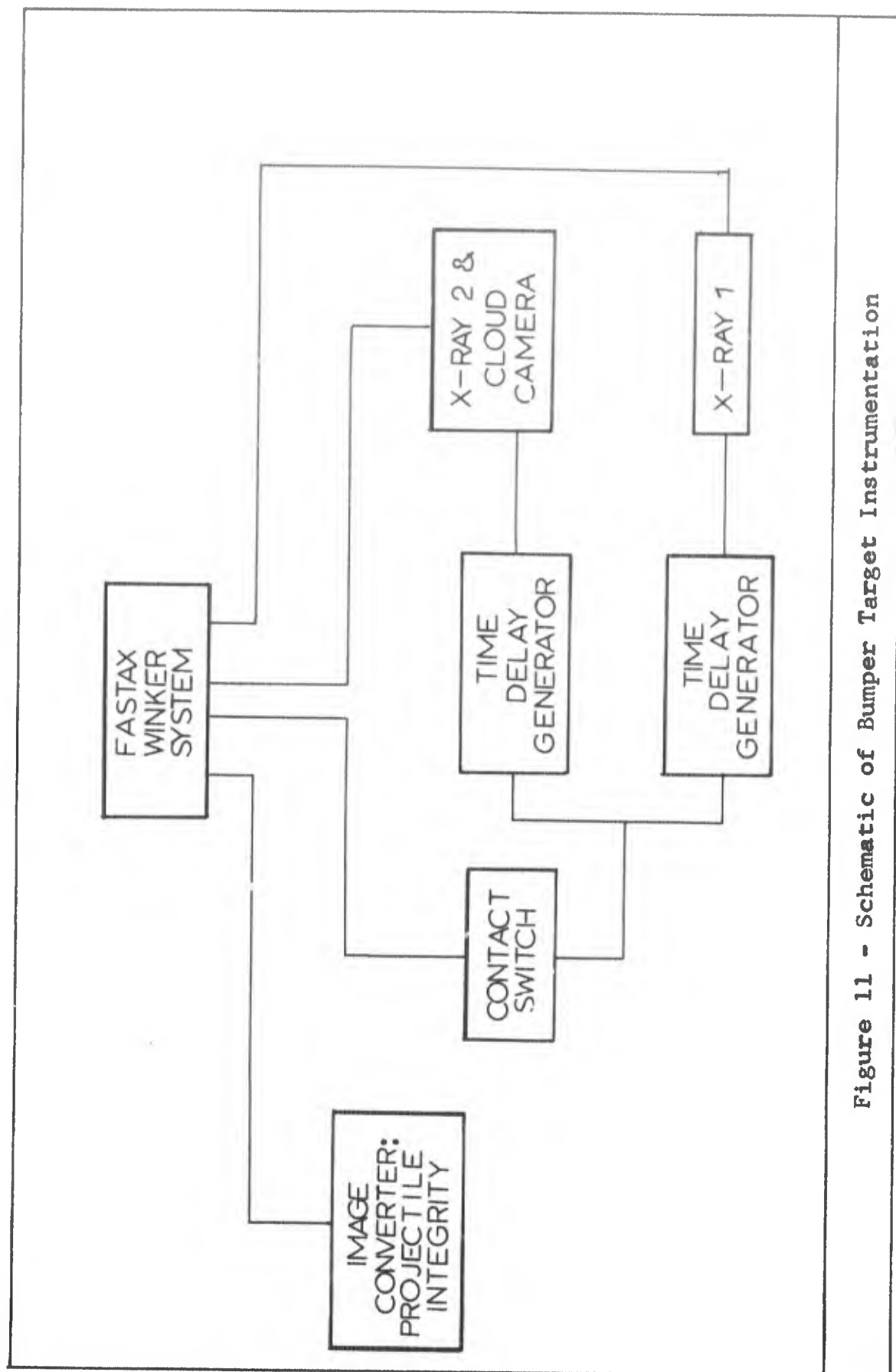
Figure 11 - Schematic of Bumper Target Instrumentation

cribed in Appendix A.

The test series consisted of six shots, three cadmium-cadmium impacts and three copper-copper impacts. For each projectile-bumper combination, one shot was fired for each of the three velocity ranges specified in Table II. The shot numbers and the resulting velocities are listed in Table V.

Shot No.	Projectile Diameter	Bumper Thickness	Velocity ft/sec
2209	1/8" Cu	1/16" Cu	21,345
2205	1/8" Cu	1/16" Cu	14,615
1022	1/8" Cu	1/16" Cu	6,560
2199	1/8" Cd	1/16" Cd	21,990
2214	1/8" Cd	1/16"Cd	10,481
1026	1/8" Cd	1/16" Cd	3,336

Results of Bumper-Witness Plate Tests

Table V

Results

Thick Target Tests. The craters in the thick targets are illustrated in Figures 12 and 13. Volumes, depths, and diameters of the craters were measured using techniques outlined in Appendix C. The impact energies were computed using the known mass and velocity of the spheres. The

GSF/Mech 67-1
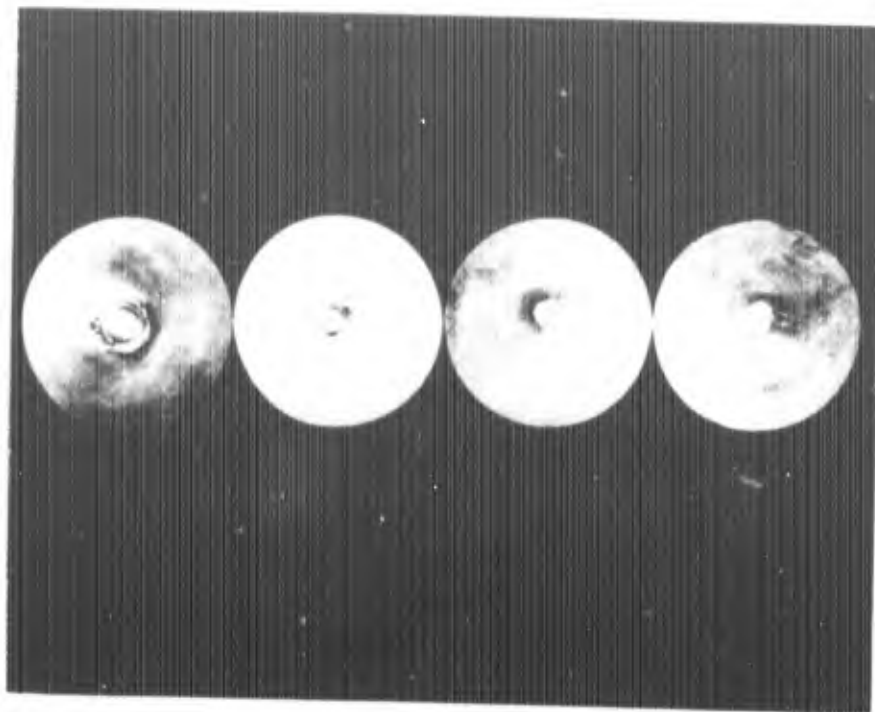
Figure 12 - Thick Copper Targets Impacted
by Cadmium Spheres
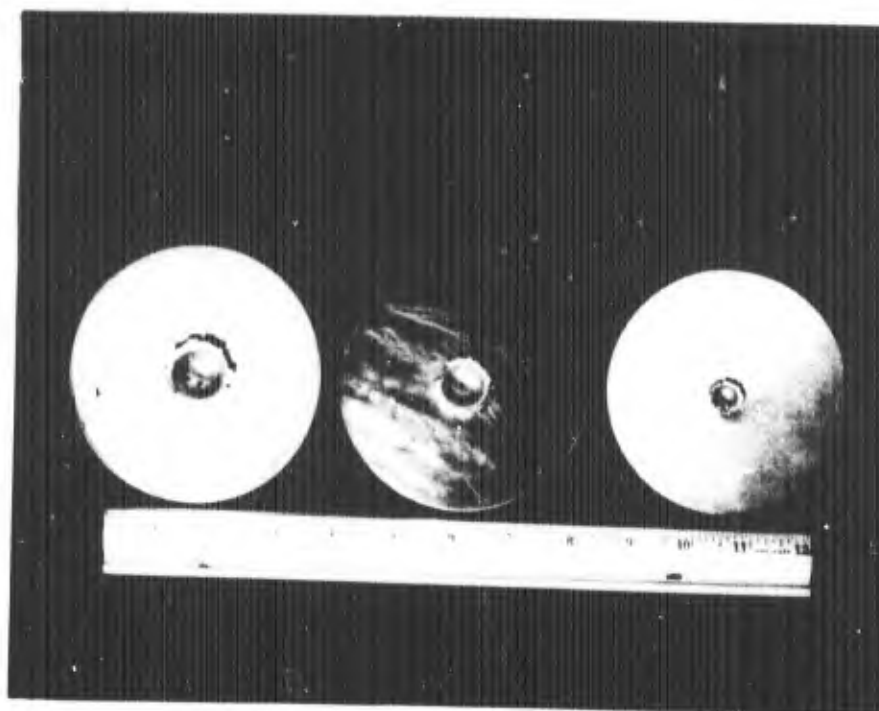
Figure 13 - Thick Copper Targets Impacted
by Copper Spheres

results of this test series are presented in Table VI.
The values of volume and energy were plotted in Figure
14. Figure 15 shows the data points on log-log axes.
The equations of the volume energy relationship were
determined to be:

$$Cu \rightarrow Cu: \quad V = 2.62 \times 10^{-3} E^{.802} \tag{4}$$

$$Cd \rightarrow Cu: \quad V = 2.85 \times 10^{-3} E^{.783} \tag{5}$$

where V and E are measured in cubic centimeters and joules,
respectively.

Bumper-Witness Plate Series. To demonstrate the
techniques used to acquire data, a complete analysis of
shot 2209 will be described in detail. A full scale
drawing was made to help in determining the alignment of
the impact point with the cloud splitter slot. A side
view of such a drawing is shown in Figure 16. The impact
zones are easily recognized on the copper witness sheets.
Lines constructed from the limits of damage on the left
and right hand witness plates were extended through the
splitter slot. The intersection point was on the uprange
side of the bumper. A line constructed normal to the bum-
per through this point located the projectile trajectory.
In this case, the projectile trajectory was seen to coin-
cide with the range axis. Since the splitter slot was also
on this axis, the sliced cloud traveled horizontally to the

26

Shot No.	Projectile	Velocity (ft/sec)	Mass (mg)	Energy (Joules)	Crater Depth (in)	Crater Diameter (in)	Crater Velocity (cc)
1018	Cd	4,792	150.1	160.1	0.1513	0.296	0.17
1015	Cd	5,901	148.5	240.2	0.1855	0.338	0.22
2207	Cd	13,593	150.5	1291.7	0.3022	0.554	0.85
2896	Cd	22,523	148.8	3513.4	0.3845	0.700	1.69
1021	Cu	7,064	152.4	353.2	0.1889	0.370	0.29
2203	Cu	16,147	152.3	1844.4	0.3212	0.587	1.09
2197	Cu	22,404	142.5	3322.4	0.3860	0.685	1.61

Results of Thick Target Shots

Table VI
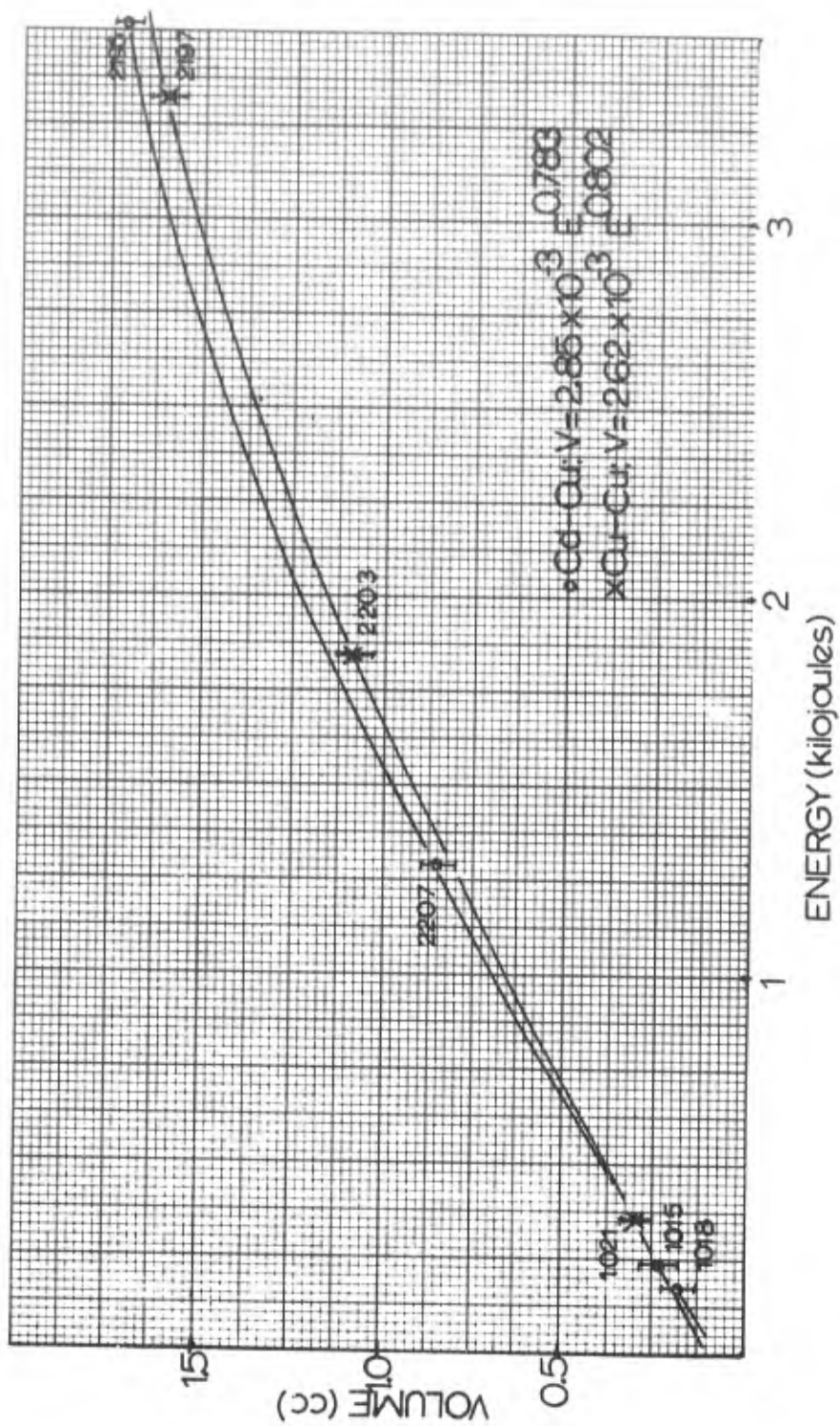
Figure 14 - Volume-Energy Plot for Thick Target Series
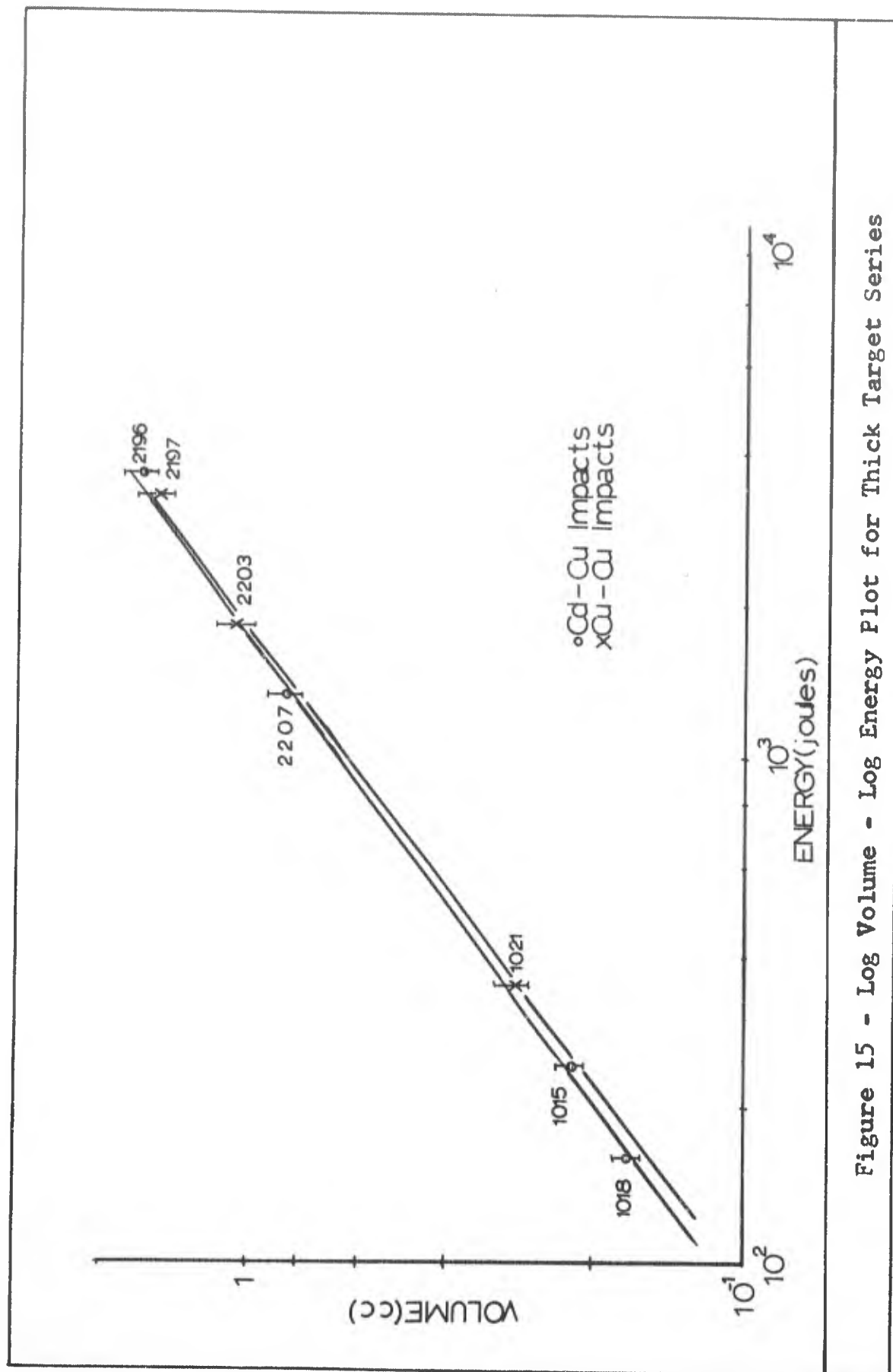
Figure 15 - Log Volume - Log Energy Plot for Thick Target Series
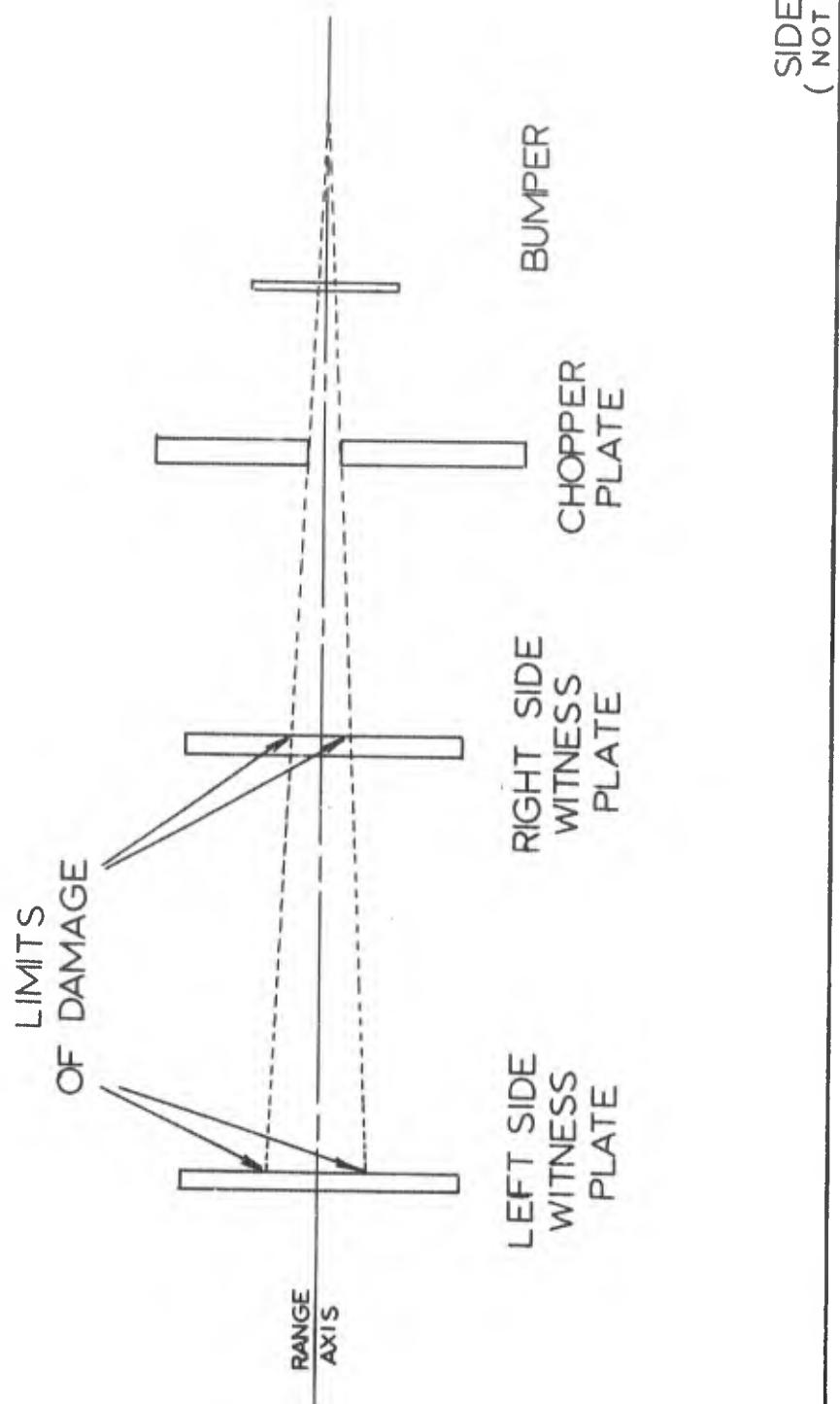
Figure 16 - Technique to Determine Impact Point-Cloud Splitter Slot Alignment

SIDE VIEW
(NOT TO SCALE)

witness plates. Radiographs of the debris cloud taken at
a 3.72 microsec interval are shown in Figure 17. A grid
was used to determine the distance traveled by the cloud
between radiographs. The grid was constructed by milling
0.010 inch grooves in one face of a 4-1/2" x 17" piece of
1/4" thick plexiglas (see Figure 18) Seven grooves 0.030
inch deep were milled along the length and 23 grooves
across the width were 0.018 inch deep. The grooves were
spaced one-half inch (±0.001") apart. Copper wire 0.010
inch in diameter was forced into the grooves. The result
was a system of 1/2" squares that were used to calibrate
distances in radiographs. The grid was suspended in the
same plane in the target tank as the sliced cloud was de-
termined to have traveled. Radiographs were made by both
X-ray channels with the grid in this position. Distortions
in the radiographs of the cloud slice due to the geometry
of the system also appeared in the radiographs of the grid.
To calibrate the portion of the debris cloud that was un-
sliced, the same grid was suspended parallel to the film
holders with one of the 17" long copper wires on the pro-
jectile trajectory. Radiographs were taken of the grid in
this position by each X-ray channel. The cloud radiographs
were placed over the calibration radiographs on a light
table. The true positions of the clouds in space were
transferred to an undistorted 1/2" grid system as in Figure
19.
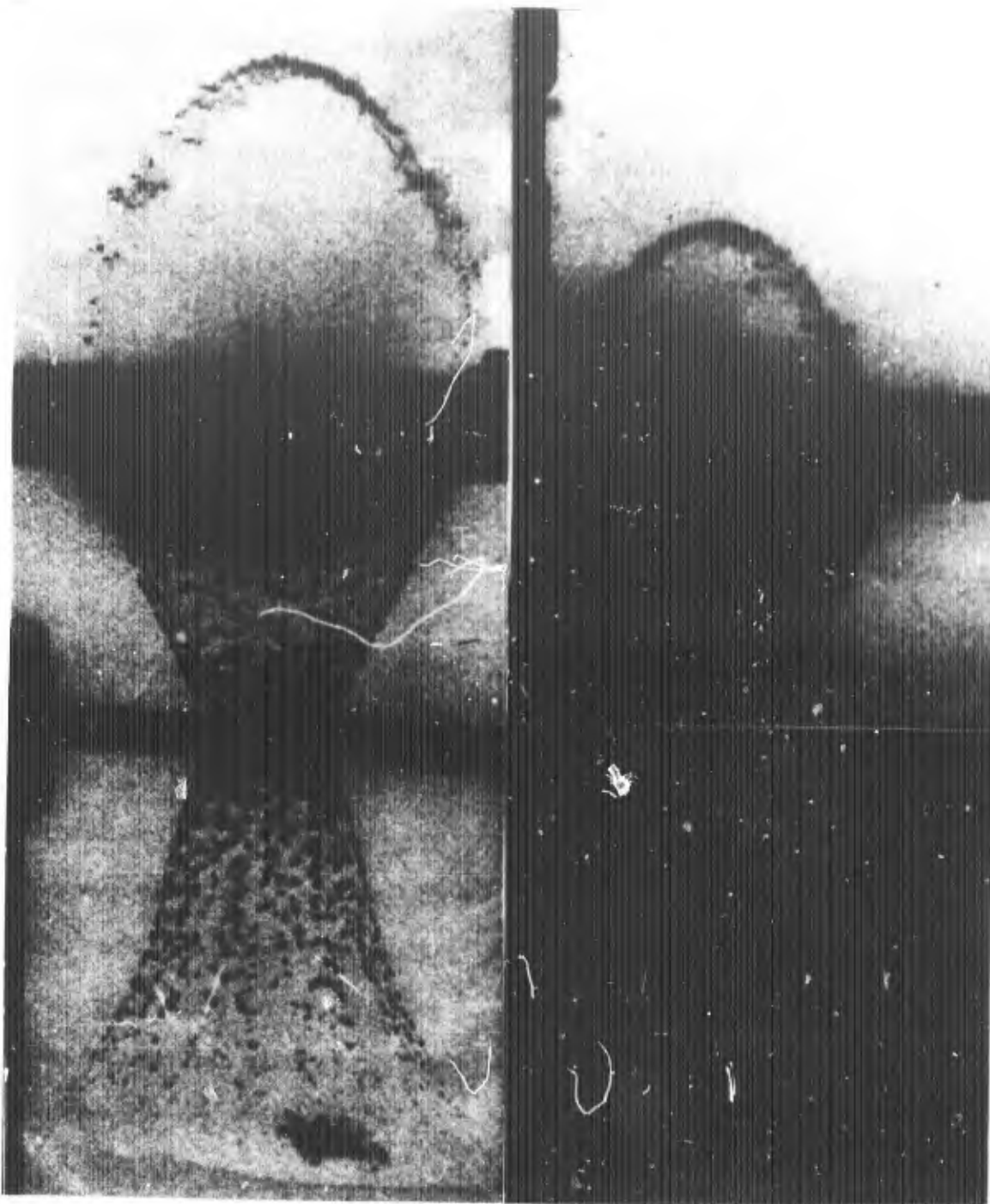
Figure 17 - Sequential Radiographs of
AFML Shot 2209
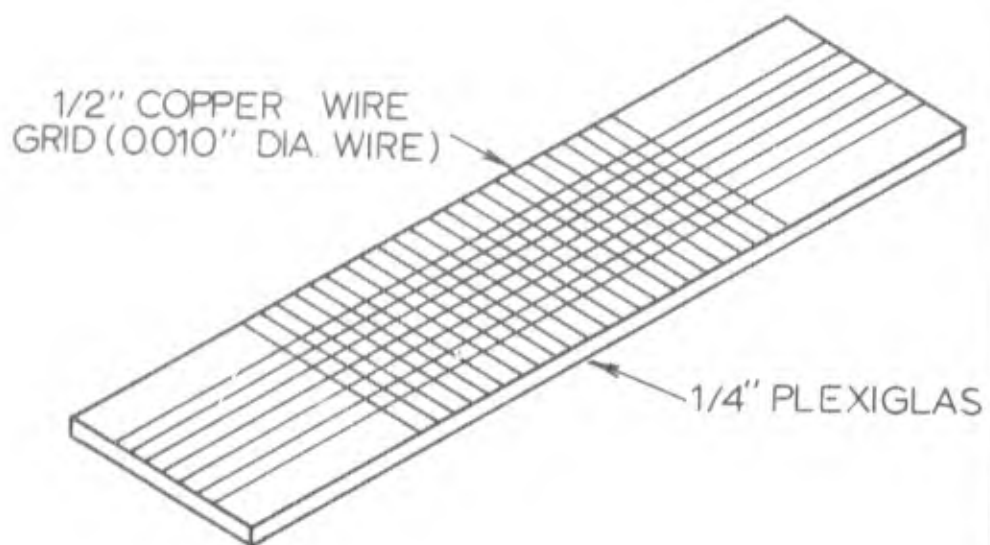
Figure 18 - X-Ray Calibration Grid
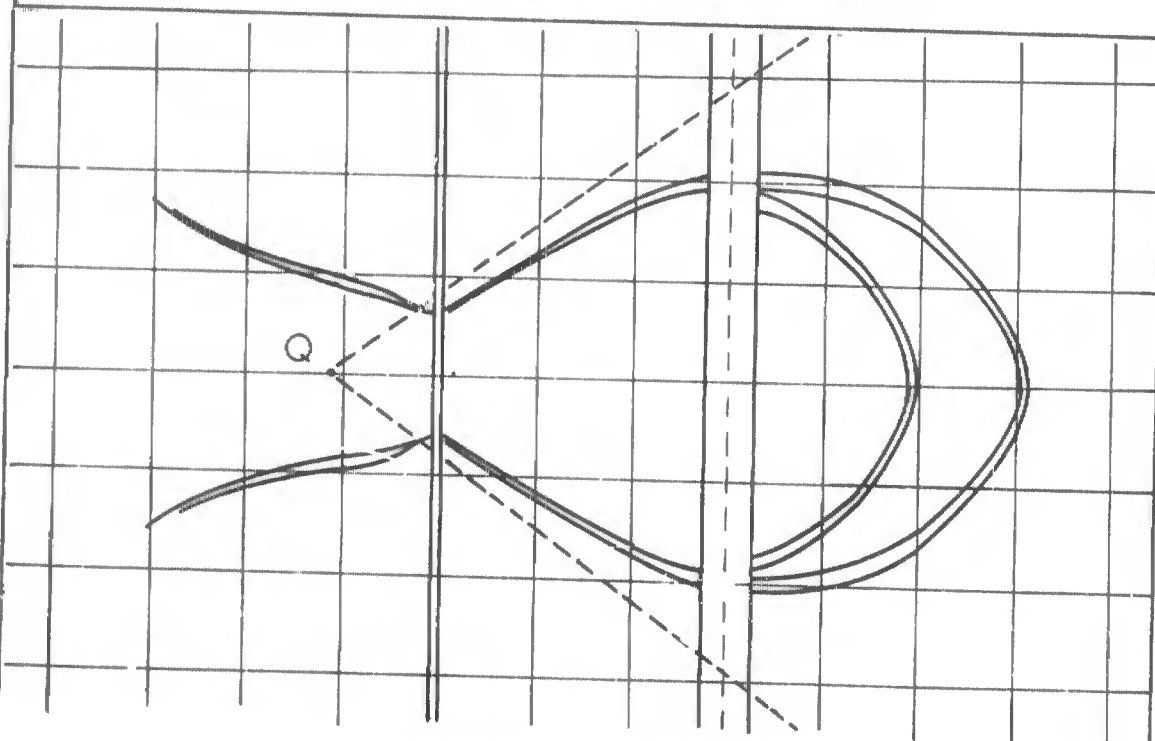
Figure 19 - Corrected Geometry of Debris Clouds
AFML Shot# 2209

Point Q was located by constructing a line between the limits of hemispherical cratering on the witness plate above the slot and the plates intersecting the right half of the cloud (see Figure 20).
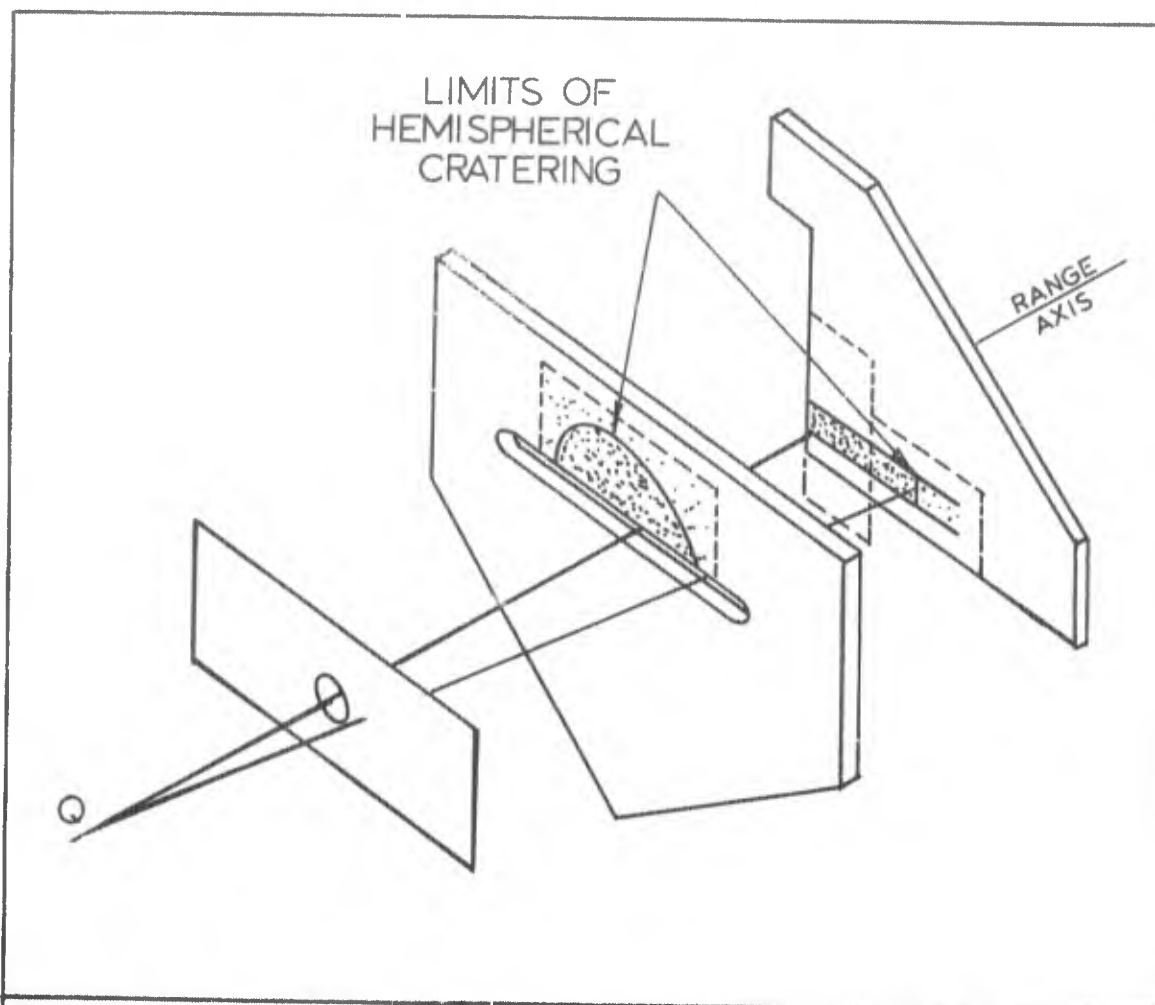
Figure 20 - Determination of Q Point for Bumper Targets

The point of intersection of this line and the range axis located Q. A full scale top view of the target geometry was required to determine α. The impact zone on the plates on the right hand side was divided into seven zones, each 3/8" in width. A line constructed from Q to the boundary of a zone intersected the projectile trajectory at an

TOP VIEW
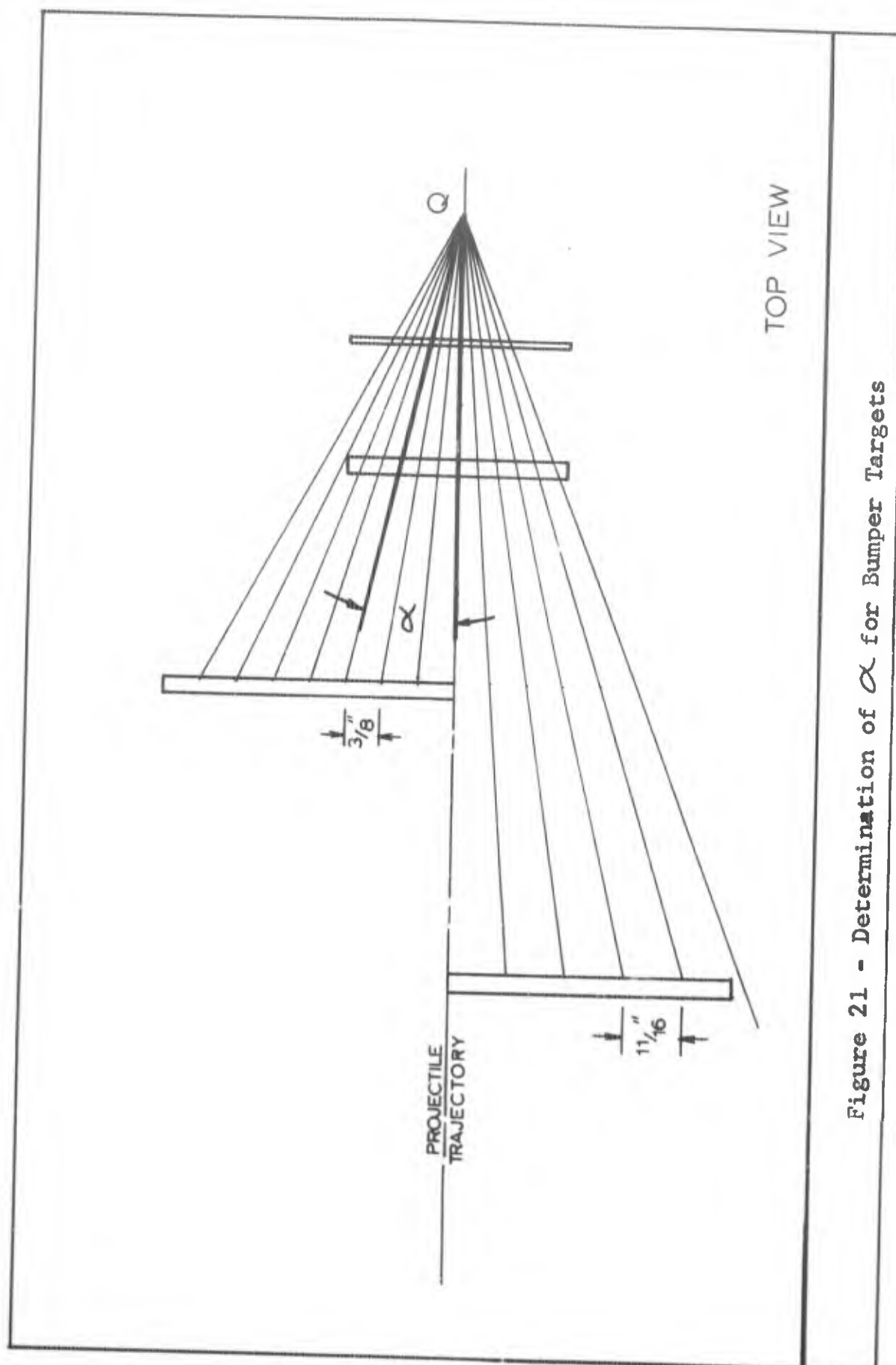
Figure 21 - Determination of α for Bumper Targets

angle α (see Figure 21). Eight particle trajectories were
determined in this manner for the right side of the cloud
slice. Lines constructed from Q at corresponding angles
left of the projectile axis divided the impact zone on the
left side into seven corresponding zones. The zones on
this side of the axis were 11/16" wide. Figure 19 was
placed on top of Figure 21 on a light table. The dis-
tances traveled by particles along the designated trajec-
tories were measured. The velocity of the particles was
computed by dividing the distance traveled by the time
between radiographs (3.72 microseconds). The results are
presented in Table VII.

α	Distance Traveled (in)	Velocity (ft/sec)
0	0.593	16.166
3.9°	0.562	12.591
7.5°	0.531	11.891
11.3°	0.468	10.483
15.4°	0.437	9.783
18.5°	0.375	8.400
21.6°	0.312	6.991
25.7°	0.156	3.495

Results of Cloud Velocity Determination
AFML Shot# 2209

Table VII

36

Due to the symmetry of the cloud, the values are the same for the right and left halves of the cloud slice. The velocities were normalized by dividing by the projectile velocity and plotted as a function of cone angle in Figure 22.

Figure 22 - V Cloud/ V Projectile vs. α
AFML Shot# 2209
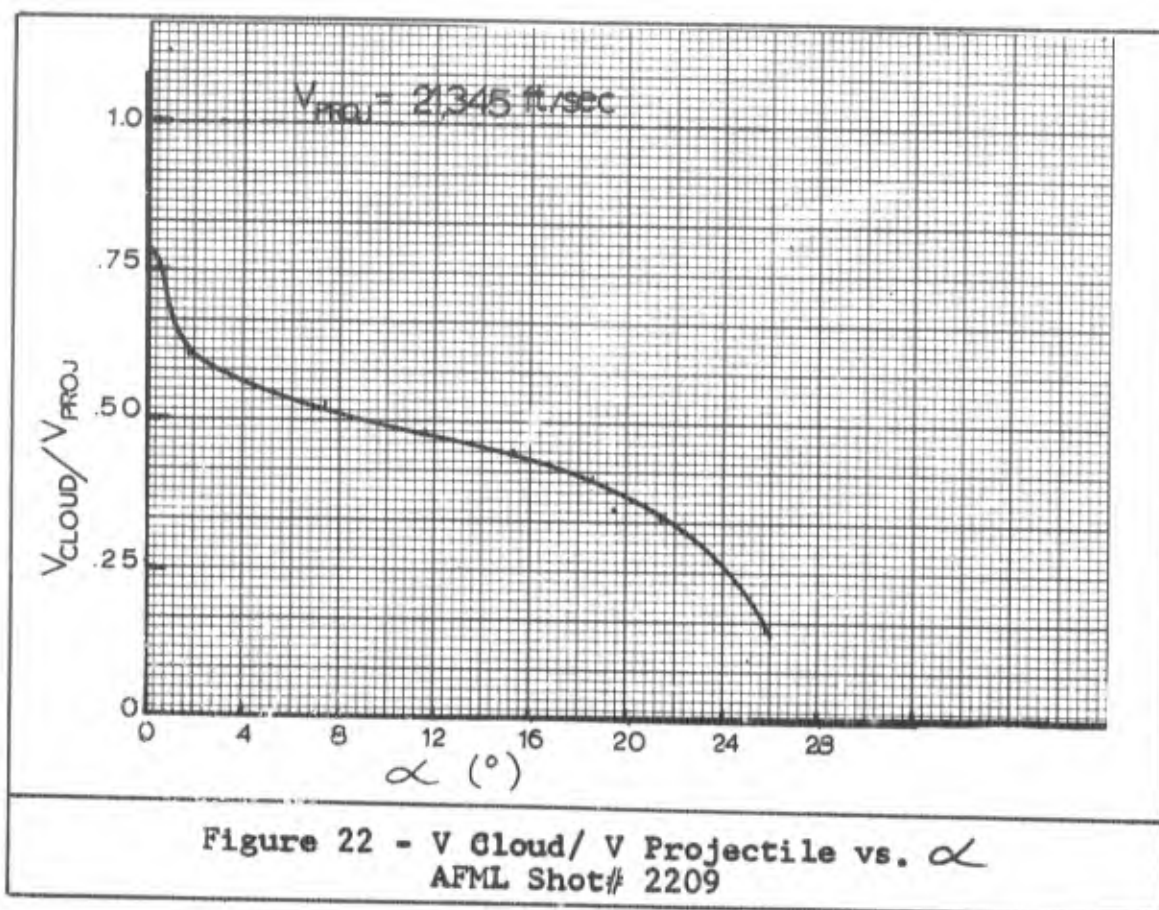
The impact zones on the witness plates were divided into sectors corresponding to the zones mentioned above. Figure 23 shows the witness plates as seen looking down-range along the range axis. Concentric circles centered at the range axis were constructed on the witness plates. Horizontal lines were also constructed along the limits of cratering. Radii drawn from the range axis to the inter-
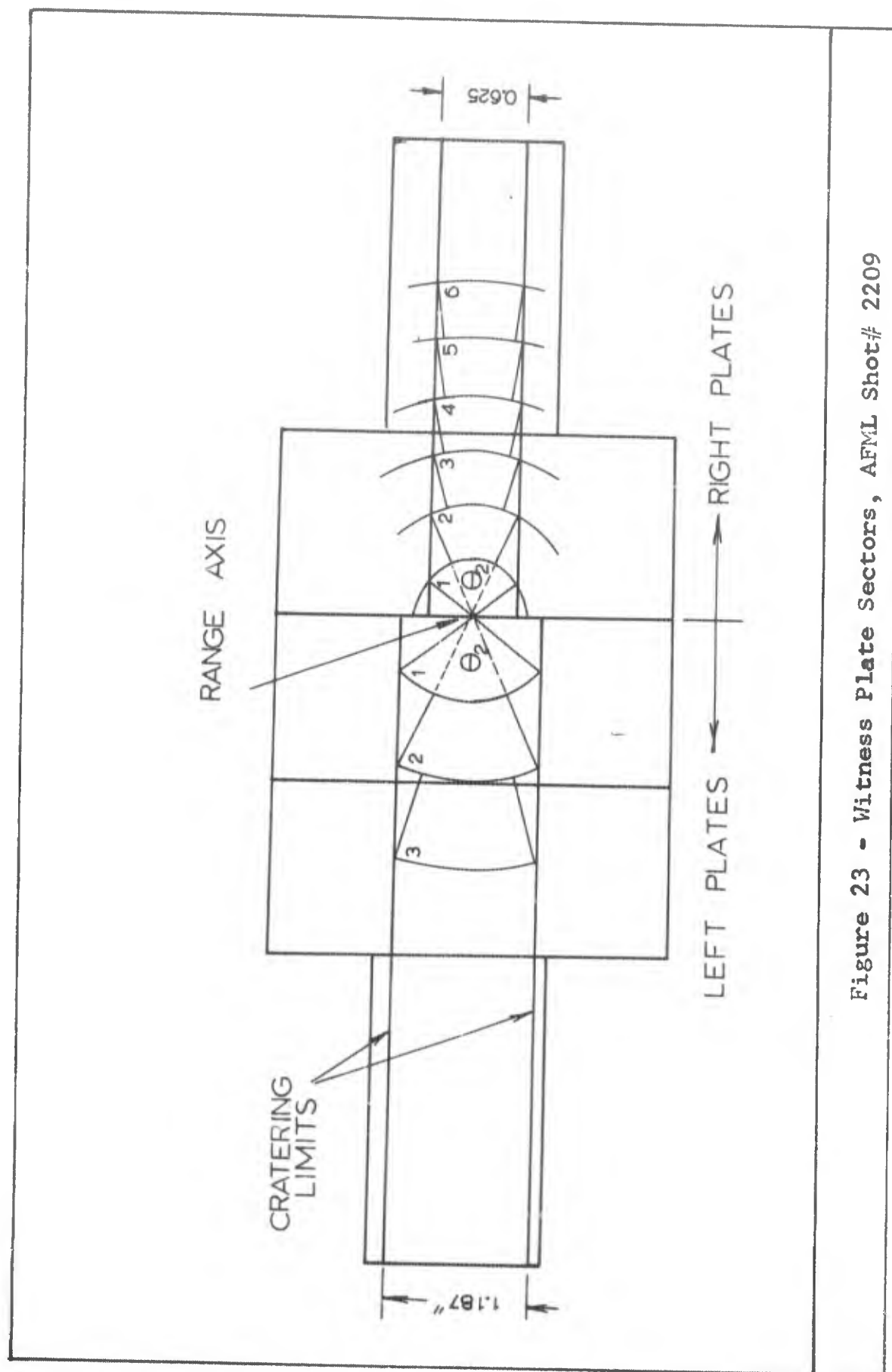
Figure 23 - Witness Plate Sectors, AFML Shot# 2209

sections of the concentric circles and the crater limit
lines completed the sector configurations. The area of the
sectors was computed by the formula:

$$A_S = \frac{\theta}{2}\left(r_0^2 - r_I^2\right)$$

(6)

where A_S is the area of the sector,

r_0 is the outer radius,

r_I is the inner radius,

θ is the central angle in radians

The area of the entire ring in which a sector is positioned
was determined by using:

$$A_r = \pi\left(r_0^2 - r_I^2\right)$$

(7)

where r_0 and r_I are as before. Due to the geometry of the
target, the ratio A_r/A_S is equal for corresponding sectors on
each side of the axis.

The crater diameters within each sector were measured
by the use of the microscope on a Tektron Microtester. The
diameters were measured to the nearest hundredth of a milli-
meter. Craters below 0.05 mm diameters were not measured.
Literally hundreds of craters of this size were present,
particularly in the sectors closest to the trajectory. The
volumes of the craters were computed assuming hemisphericity.

The next step involved determining the energy required to form the craters. It was discovered that the Brinell hardness readings of the copper billet materials and the copper plates were not the same. The readings were 123 and 80 (kg/mm^2) for the plates and billets, respectively (see Appendix C-2). The plots in Figure 15 had to be adjusted. Eichelberger and Gehring have established a linear volume-energy relationship based on the Brinell hardness of the target.

$$V = 4 \times 10^{-2} E/B_H \qquad (8)$$

<div align="right">(Ref 12:1591)</div>

where V is the volume in cc and E is energy in joules. B_H is Brinell hardness in kg/mm^2. The plot of log V - log E was adjusted for this hardness effect using the ratio

$$\frac{V_1}{V_2} = \frac{B_{H_2}}{B_{H_1}} = \frac{80}{123} = 0.65$$

where the subscript 1 refers to the hard copper and 2 to the soft copper. The adjusted plot is shown in Figure 24. The equations for the V - E relationship were recomputed as:

$$Cd-Cu: \quad V = 1.85 \times 10^{-3} E^{0.783} \qquad (9)$$

$$Cu-Cu: \quad V = 1.70 \times 10^{-3} E^{0.802} \qquad (10)$$
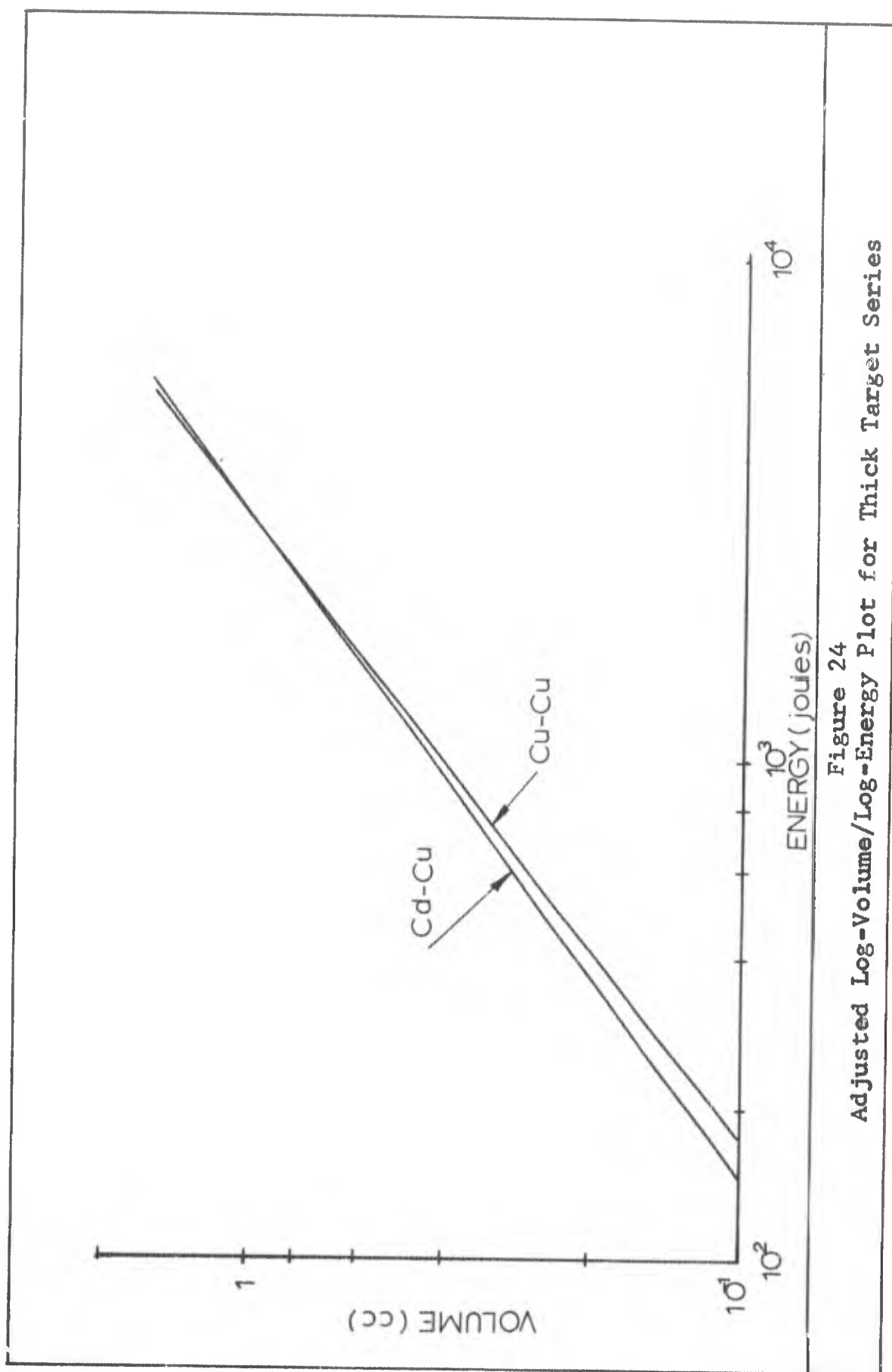
Figure 24

Adjusted Log-Volume/Log-Energy Plot for Thick Target Series

the log of E/V vs log V was then plotted in Figure 25. To determine the cratering energy in AFML Shot 2209, the energy corresponding to a given crater volume was read from the recomputed curve of Cu - Cu impacts. To facilitate this, Figure 25 was plotted by decades of volume size in Figure 26. The energies corresponding to craters within a sector were added to obtain the sector energy, E_S.

The results from the calculations of A_r, A_S, and E_S are presented in Table VIII. The total energies E_r were computed by multiplying the energy in a given sector by A_r/A_S. Table IX gives the sectors and corresponding α-ranges.

E_r and energy density as a function of cone angle are shown in Figures 27 and 28, respectively. The curves were fitted through the energy and energy density values at the mid-points of each interval.

Arithmetic average values V_A of cloud front velocities were computed for each cone angle interval. The velocity of the cloud moving at the cone angle interval was assumed to be V_A. The total mass M_r in each cone angle was computed by solving the equation:

$$E_r = \frac{M_r}{2} V_A^2 \tag{11}$$

for M_r, where E_r is in joules, V_A in m/sec, and M_r is in kg. The values of M_r and V_A were multiplied to give the

42
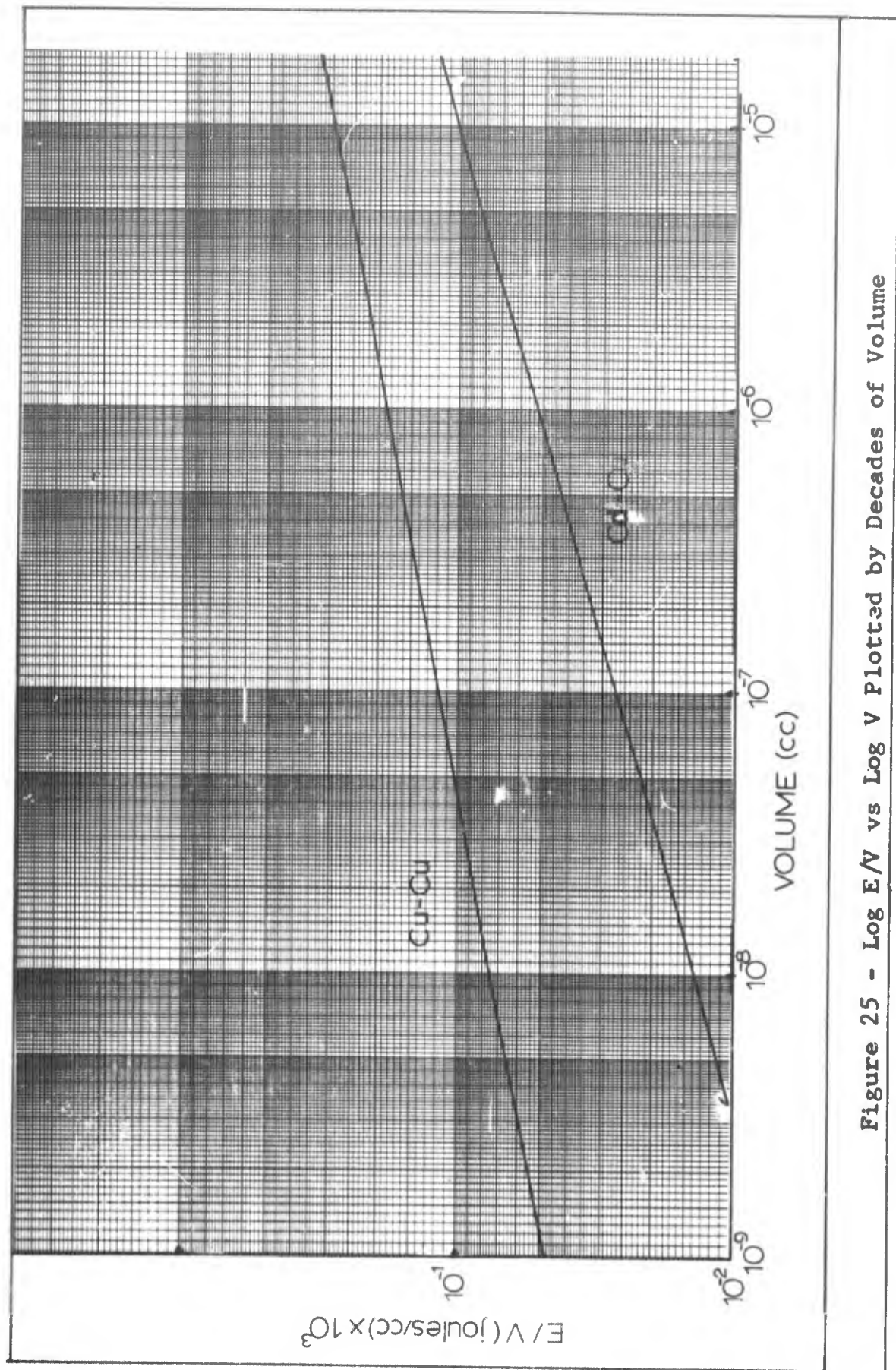
Figure 25 - Log E/V vs Log V Plotted by Decades of Volume
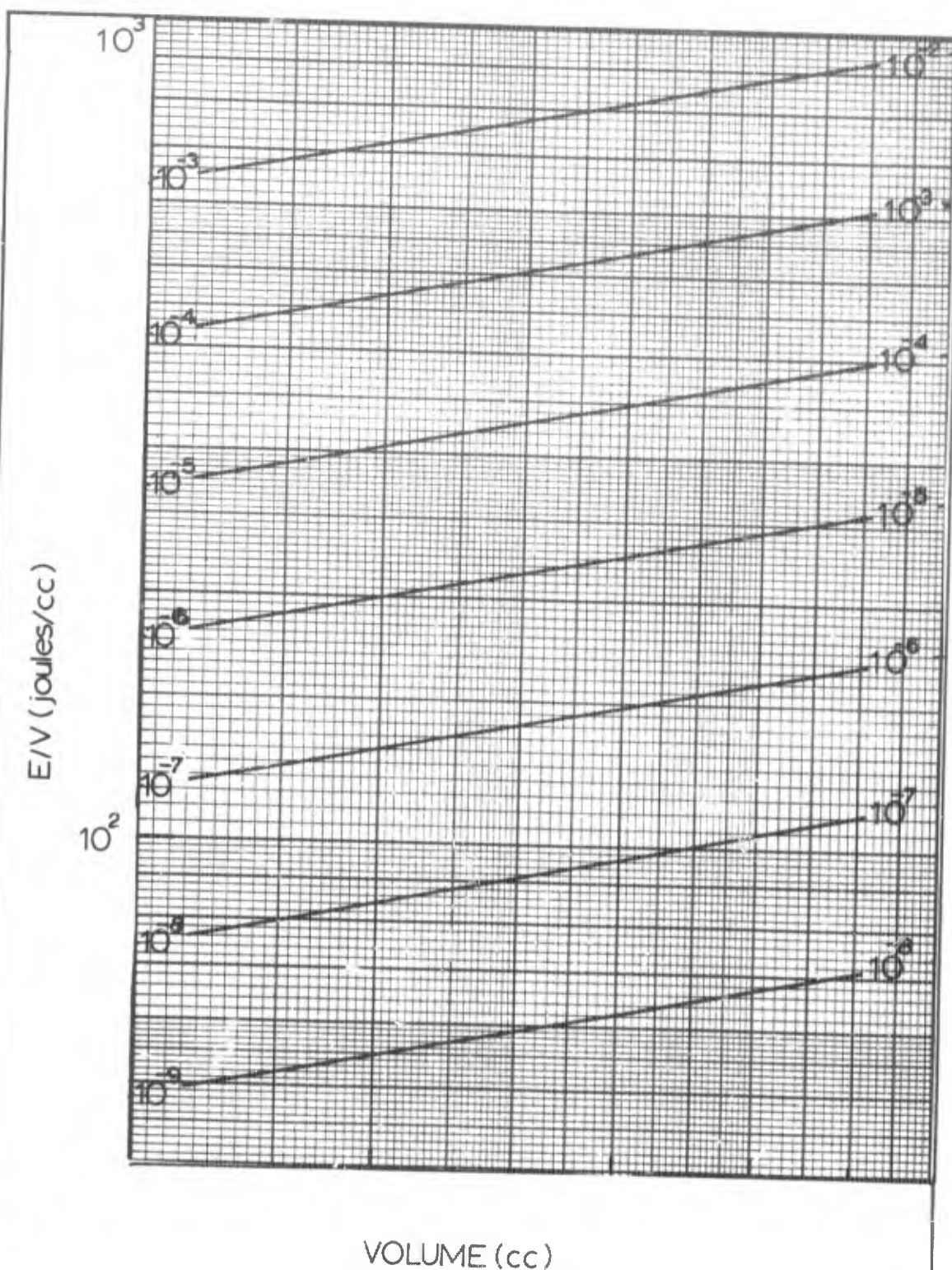
Figure 26 - Log E/V vs Log V
Plotted by Decades of Volume

Left Side					Ar/As	Sector	Right Side				
As (in2)	Ar (in2)	Es (joules)	Er (joules)	Density E (1/in2)			As (in2)	Ar (in2)	Es (joules)	Er (joules)	Density E (1/in2)
0.437	1.49	0.126	0.43	0.29	3.4	1	0.130	0.44	0.347	1.18	2.67
0.595	4.45	0.313	2.35	0.53	7.5	2	0.177	1.325	0.552	4.15	3.12
0.680	7.42	0.539	5.87	0.80	10.9	3	0.202	2.210	0.610	6.65	3.02
0.692	10.40	0.898	13.5	1.30	15.0	4	0.206	3.09	1.085	16.35	5.25
0.707	13.35	1.186	22.35	1.68	18.9	5	0.210	3.96	1.037	19.60	4.94
0.724	16.35	2.172	49.0	3.00	22.6	6	0.216	4.87	2.975	67.2	13.75

Energy and Energy Density for AFML Shot# 2209

Table VIII
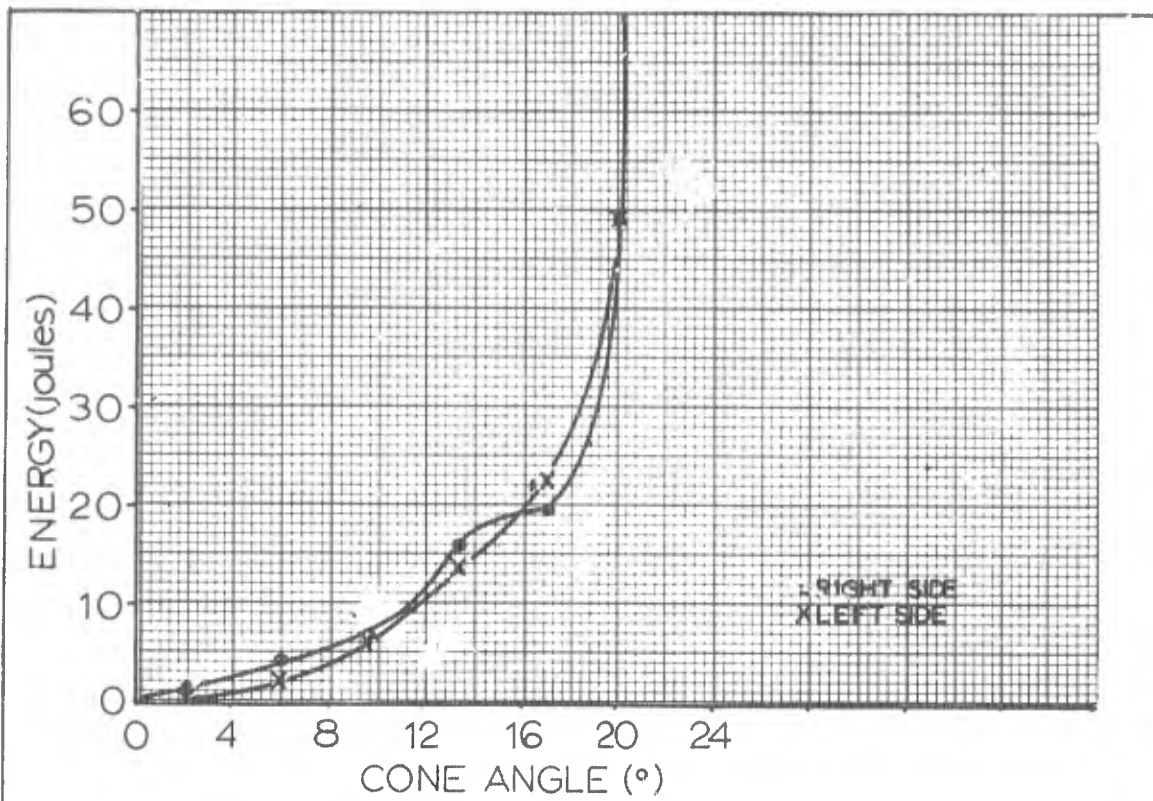
Figure 27 - E_T vs Cone Angle α, AFML Shot# 2209
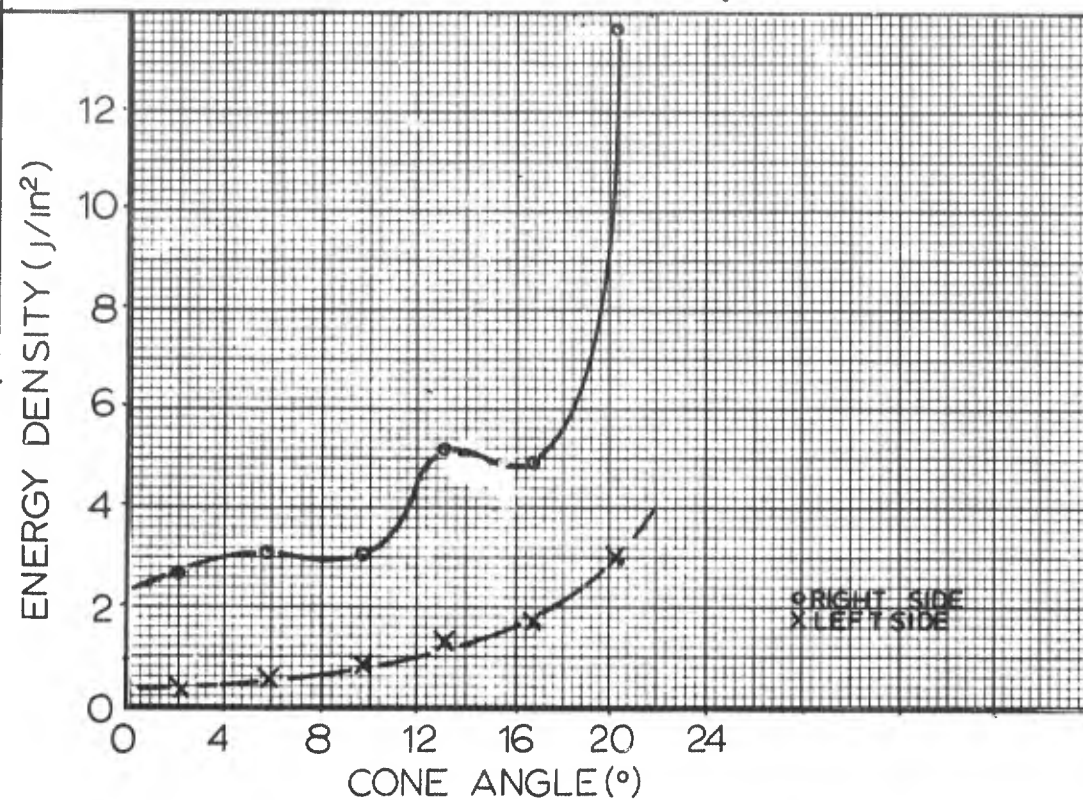
Figure 28 - Energy Density vs Cone Angle α
AFML Shot# 2209

momentum I_r as a function of cone angle. The results of
these calculations are tabulated in Table X. Plots of the
calculations are shown in Figures 29 and 30.

Sector	α-Range (°)
1	0 - 3.9
2	3.9 - 7.5
3	7.5 - 11.3
4	11.3 - 15.0
5	15.0 - 18.5
6	18.5 - 21.9

Sectors and Corresponding α-Range
AFML Shot# 2209

Table IX

Figure 31 is a photograph of the cloud taken simul-
taneously with the triggering of X-ray 2. The direction
of motion is from right to left. The cloud is approxi-
mately 0.9 actual size. The flat edge in the right side of
the picture is the back face of the splitter plate through
which the cloud has passed. The edges of the cloud are not
straight, indicating that a vapor state may be present.

The results for the remaining shots in the test series
are presented in the remainder of this section. The analy-
tical method of data reduction was the same for all shots and
will not be repeated. Certain characteristic differences

	Left Side				Right Side	
Sector	M_r (mg)	I_r (kg-m/sec x 10^3)	V_A (m/sec)		M_r (mg)	I_r (kg-m/sec x 10^3)
1	0.04	0.18	4.38×10^3		0.12	0.53
2	0.34	0.13	3.73×10^3		0.60	2.24
3	1.00	0.34	3.41×10^3		1.14	3.89
4	2.70	8.30	3.08×10^3		3.45	10.62
5	5.43	15.60	2.87×10^3		4.77	13.65
6	17.90	41.95	2.34×10^3		24.60	57.50

Mass and Momentum for AFML Shot# 2209

Table X
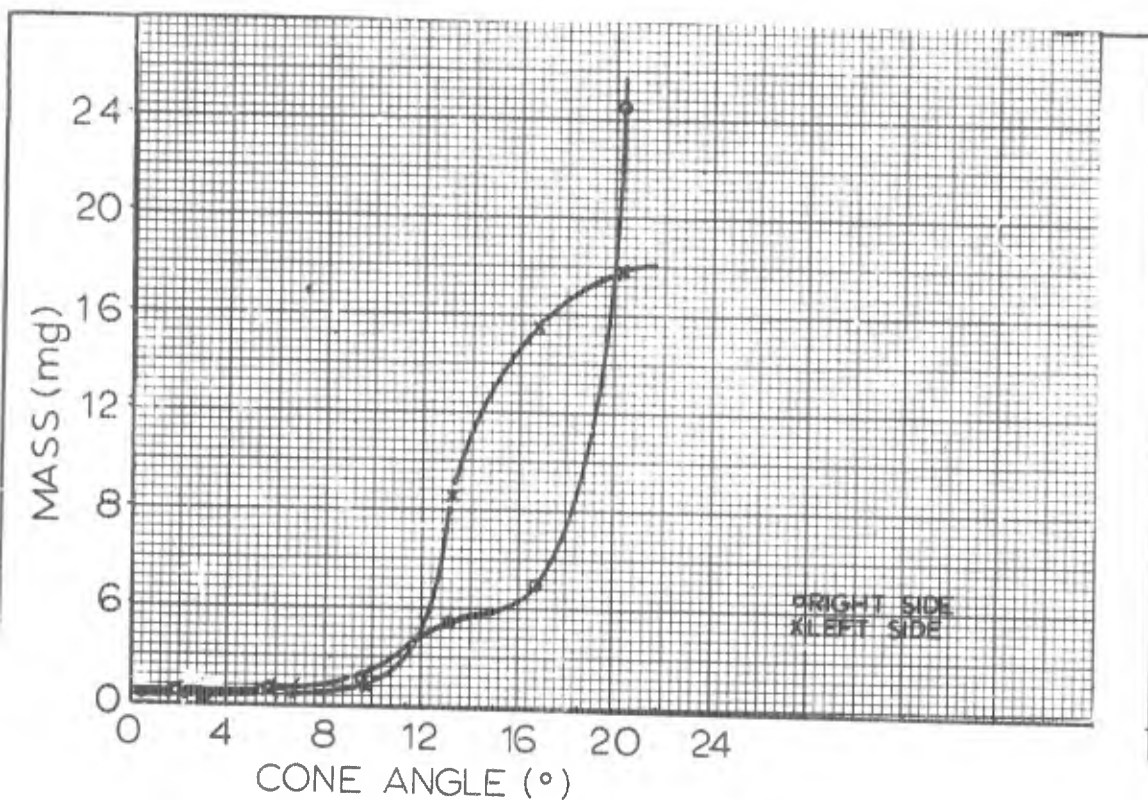
Figure 29 - Mass vs Cone Angle α
AFML Shot# 2209
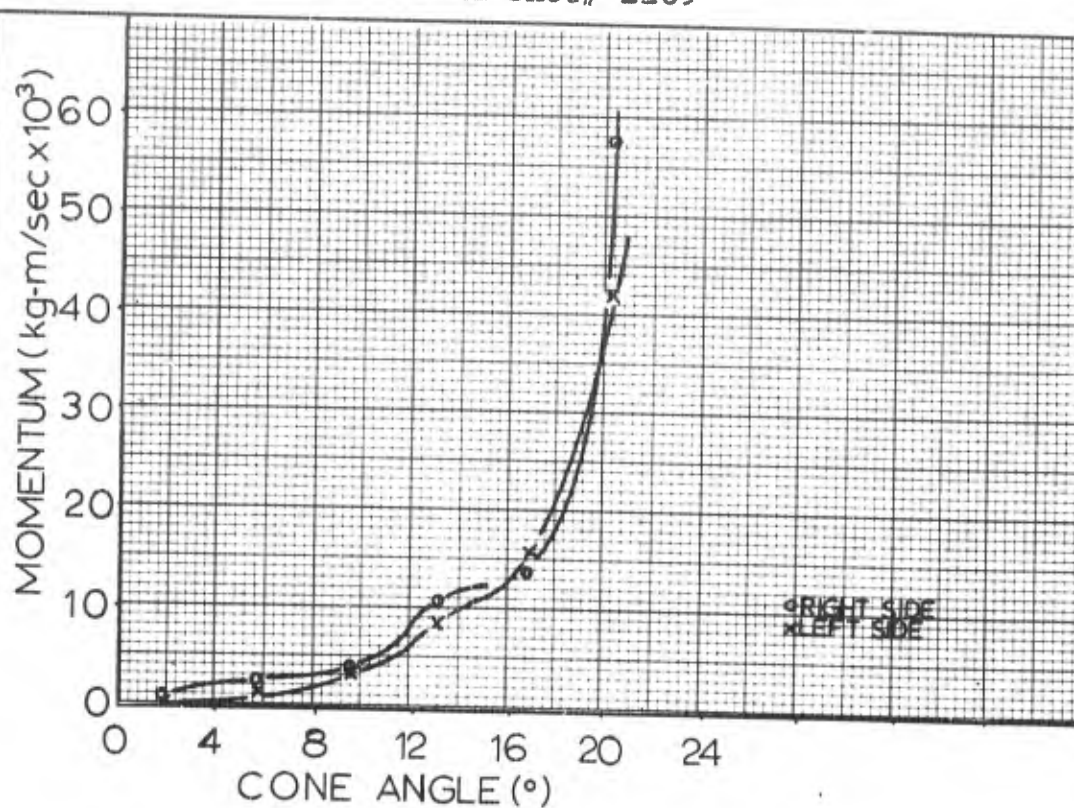
Figure 30 - Momentum vs Cone Angle α
AFML Shot# 2209
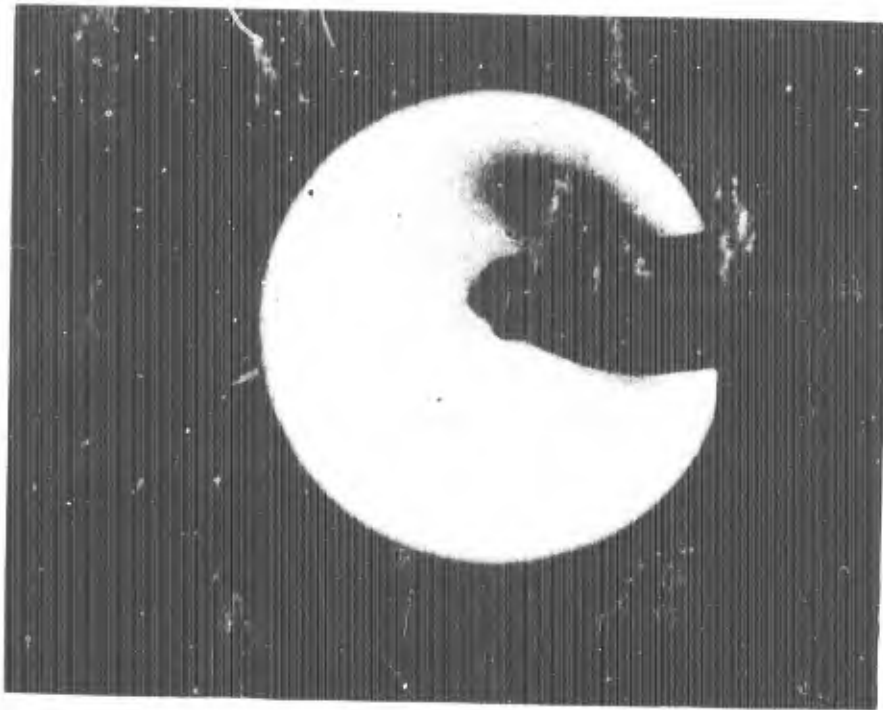
Figure 31 - Photograph of Sliced
Debris Cloud, AFML Shot 2209

in the results are noted, however.

a. AFML Shot# 2205 - A copper sphere impacted a
1/16" copper sheet at 14,615 ft/sec. The associated graphs
and tables are presented below. Figure 33 shows the
asymmetric nature of the debris pattern. Cloud velocities
for the right and left halves of the cloud were computed.
The results are shown in Table XI. The time between radio-
graphs was 7.76 microseconds. Figure 34 shows the plots of
normalized cloud velocities for the left and right sides of
the cloud. Table XII gives the results of the energy and
energy density calculations. Table XIII gives the corres-
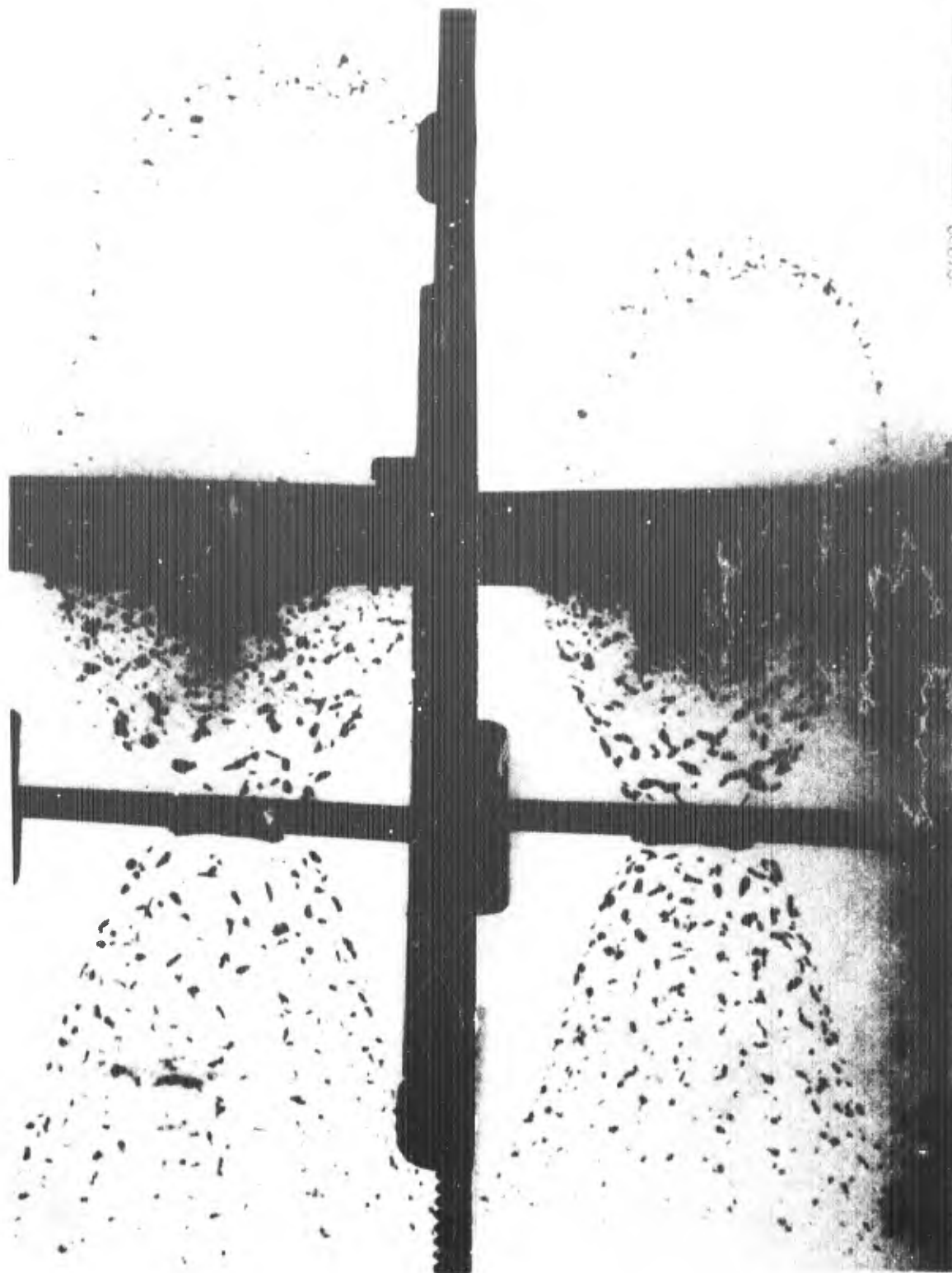
Figure 32
Sequential Radiographs of
AFML Shot# 2205
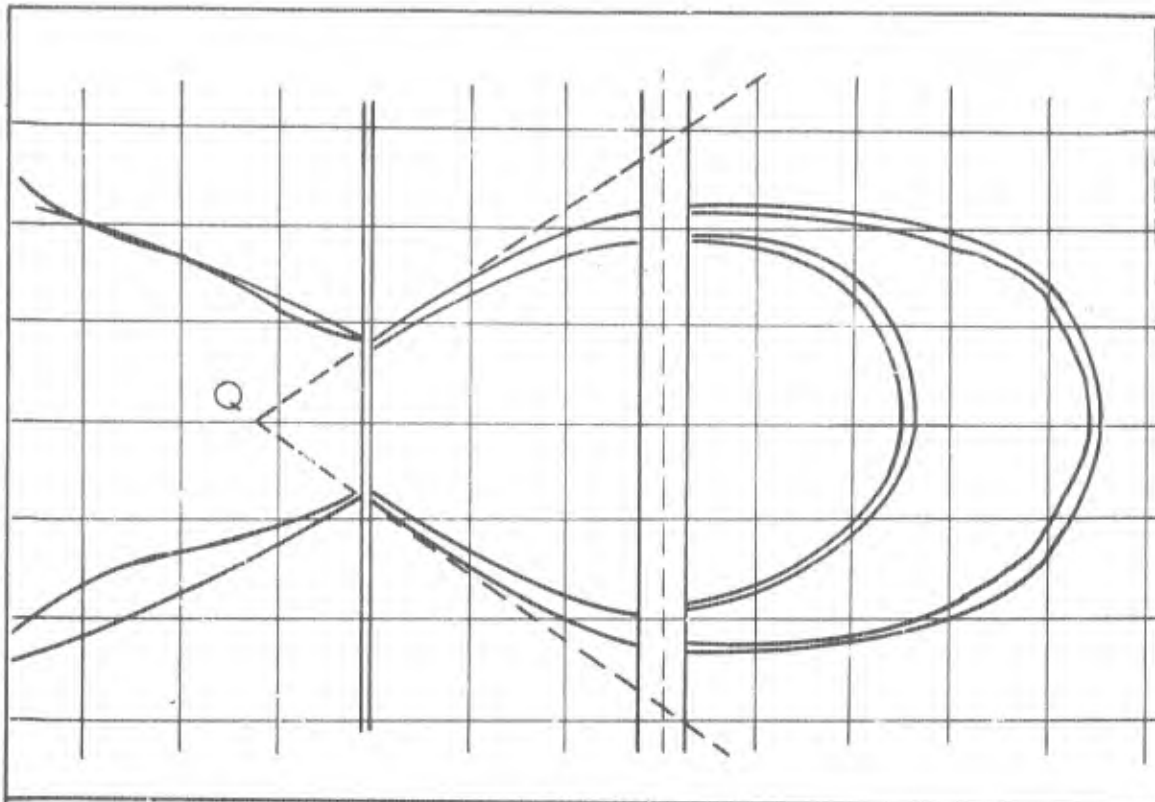
Figure 33 - Corrected Geometry of Debris Clouds
AFML Shot# 2205
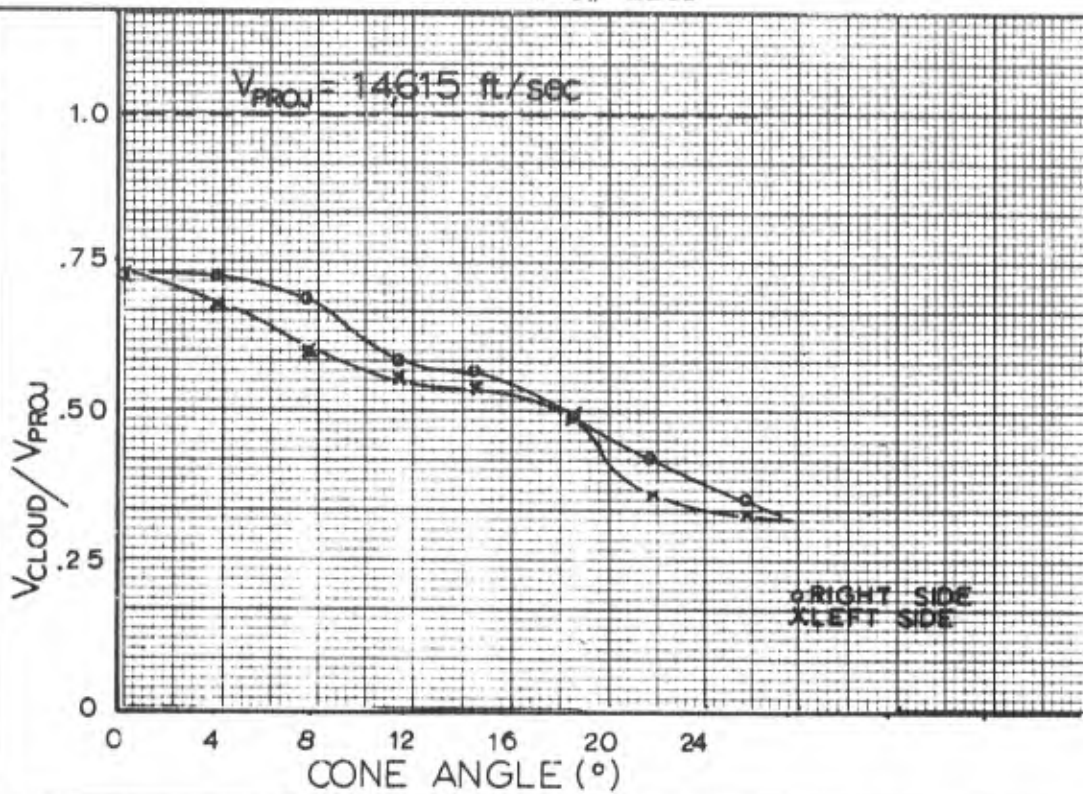
Figure 34 - V Cloud/V Projectile vs α
AFML Shot# 2205

Table XI

Left Side			Right Side	
Distance Traveled (in)	Velocity (ft/sec)	α (°)	Distance Traveled (in)	Velocity (ft/sec)
1.00	10,741	0	1.00	10,741
0.94	10,058	3.8	1.00	10,741
0.88	9,391	7.5	0.95	10,233
0.80	8,550	11.2	0.92	9,883
0.76	8,216	14.4	0.83	8,891
0.66	7,041	18.3	0.66	7,041
0.47	5,000	21.7	0.53	5,666
0.44	4,666	24.9	0.50	5,366

Results of Cloud Velocity Determination
AFML Shot# 2205

Table XII

Left Side						Sector	Right Side				
As (in2)	Ar (in2)	Es (joules)	Er (joules)	Density E (j/in2)	Ar/As		As (in2)	Ar (in2)	Es (joules)	Er (joules)	Density E (j/in2)
0.07	1.49	0.001	0.011	0.007	21.25	1	0.03	0.44	0.168	3.58	6.25
0.49	4.45	2.984	27.20	6.080	9.1	2	0.15	1.33	3.695	33.60	25.40
0.37	7.42	3.012	60.72	8.140	20.2	3	0.11	2.21	0.897	18.20	8.18
0.41	10.40	0.79x	21.30	1.97	25.7	4	0.12	3.09	2.075	53.20	17.25
0.43	13.35	-	-	-	31.3	5	0.13	3.96	0.471	14.30	3.71
0.45	16.35	-	-	-	37.5	6	0.13	4.87	1.118	35.1	8.60

Energy and Energy Density for AFML Shot# 2205

Sector	α - Range (^{o})
1	0 - 3.8
2	3.8 - 7.5
3	7.5 - 11.2
4	11.2 - 14.4
5	14.4 - 18.3
6	18.3 - 21.7

Sectors and Corresponding α - Range
AFML Shot #2205

Table XIII

pondence between sectors and α for this shot. No crater
data was available for sectors 5 and 6 on the left side.
The projectile impacted 7/32" above the range axis, which
added to the distortion in the radiographs. The results
of Table XII are plotted in Figures 35 and 36. The re-
sults of the mass and momentum calculations are shown in
Table XIV. The results of Table XIV are plotted in Figures
37 and 38 as a function of cone angle. Figure 39 is a
photograph of the sliced debris cloud. The downward slope
of cloud movement was a result of the projectile trajectory
being above the range axis. The edges of the cloud are
not straight, which may indicate the presence of vapor.
Table III predicts incipient melting, with predominately
solid debris for Cu-Cu impacts at 14,615 ft/sec.
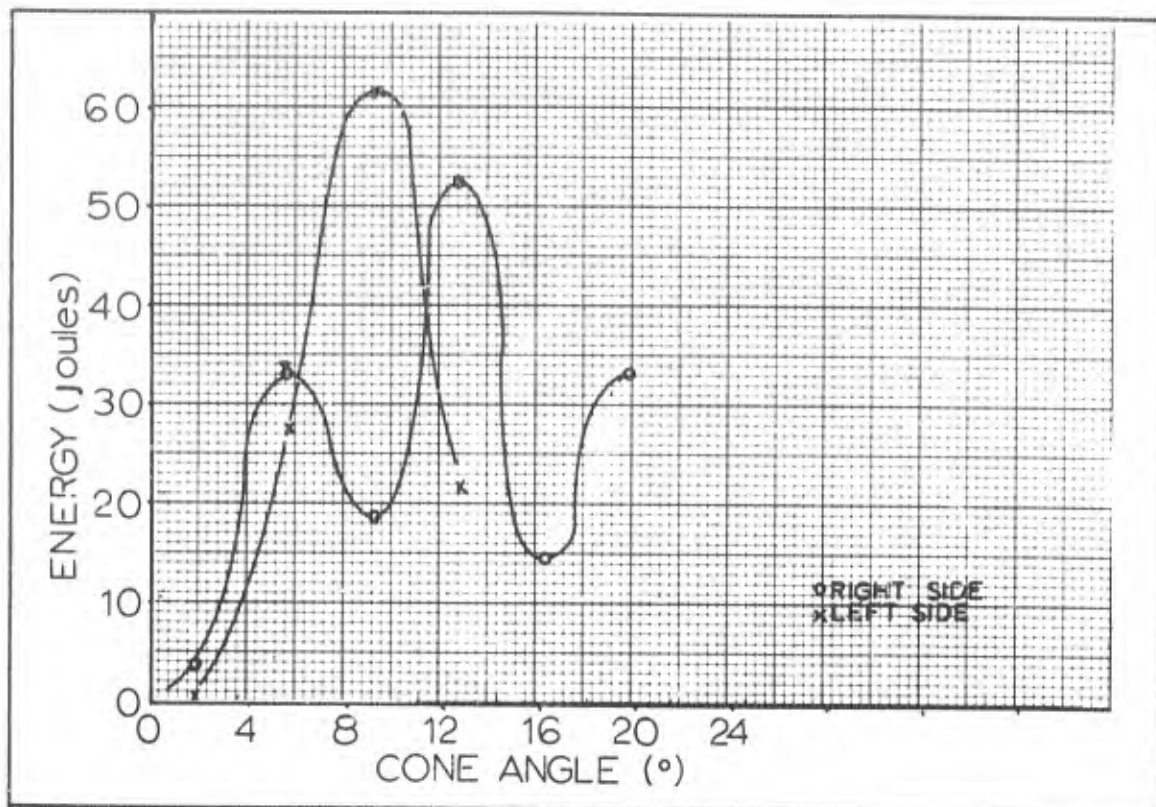
Figure 35 - E_r vs Cone Angle α , AFML Shot 2205
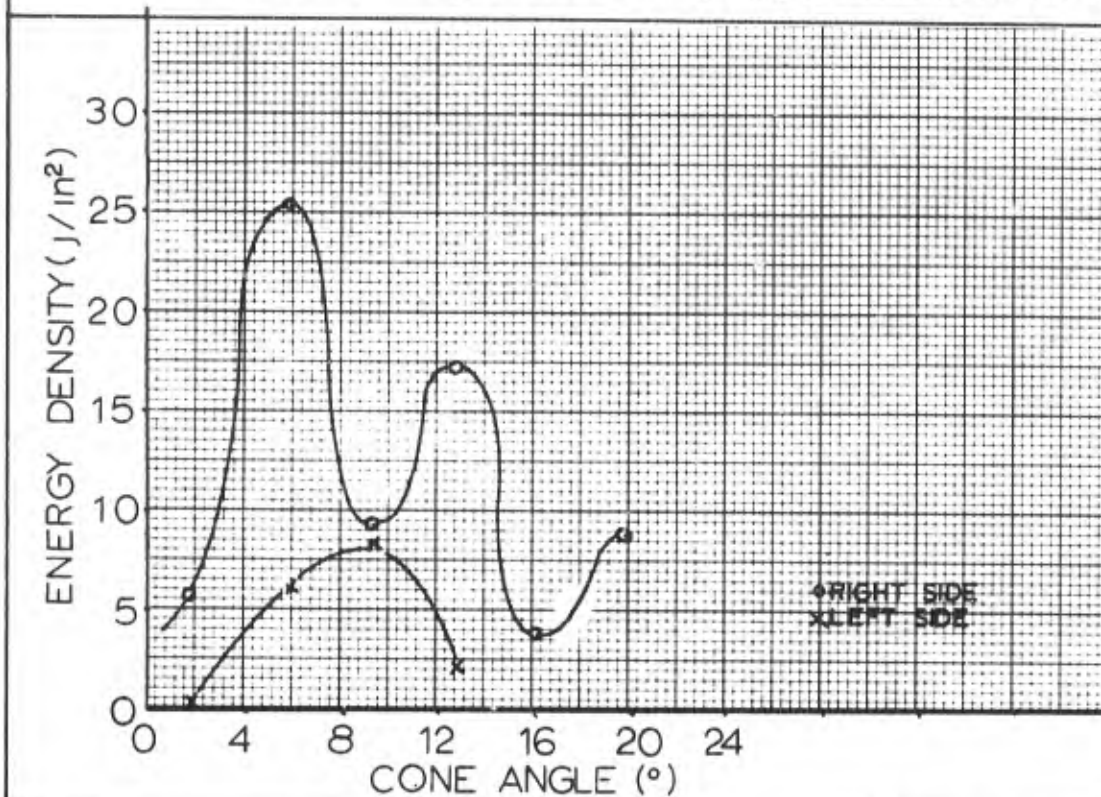
Figure 36 - Energy Density vs Cone Angle α
AFML Shot# 2205

Left Side			Sector	Right Side		
V_A (m/sec)	M_r (mg)	I_r (kg-m/sec$\times10^3$)		V_A (m/sec)	M_r (mg)	I_r (kg-m/sec$\times10^3$)
3.16×10^3	0.002	0.0	1	3.27×10^3	0.66	2.16
2.96×10^3	6.22	18.40	2	3.18×10^3	6.72	21.40
2.73×10^3	15.85	43.25	3	3.06×10^3	3.90	11.92
2.55×10^3	6.55	16.71	4	2.86×10^3	13.05	37.38
2.32×10^3	-	-	5	2.42×10^3	4.89	11.82
1.84×10^3	-	-	6	1.93×10^3	18.89	36.42

Mass and Momentum
AFML Shot# 2205

Table XIV
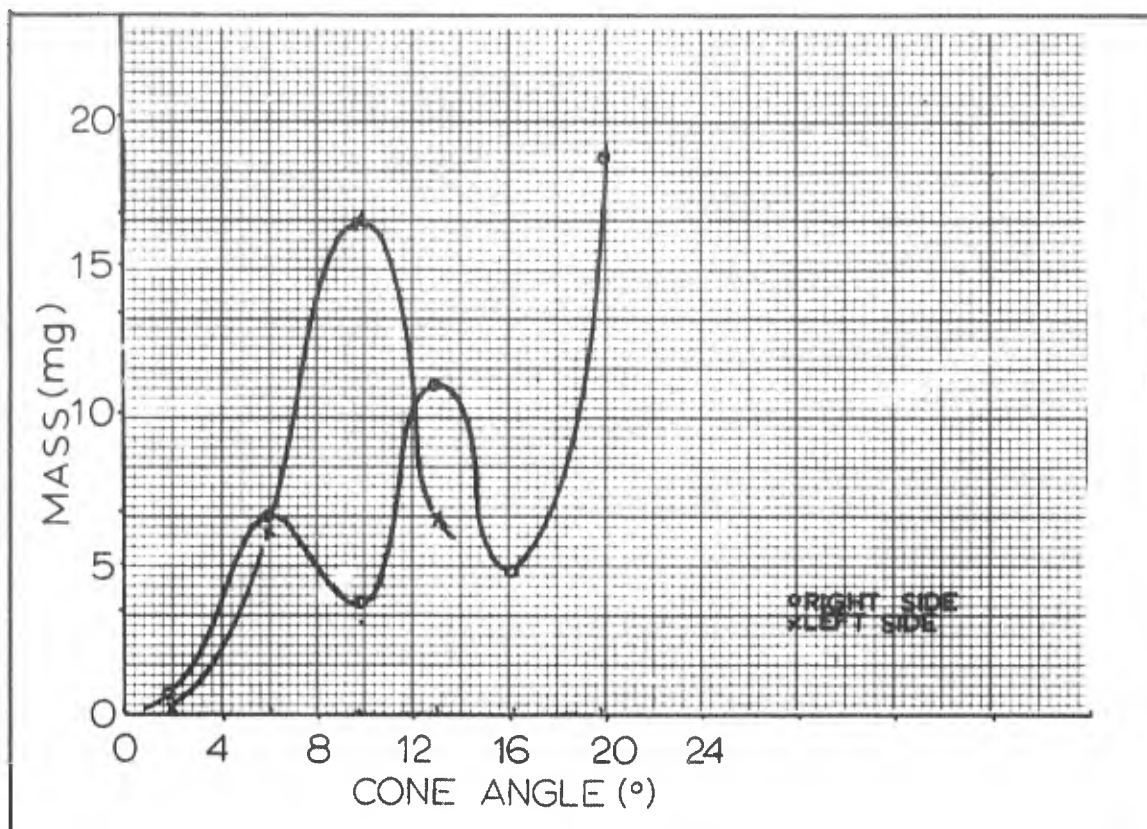
Figure 37 - Mass vs Cone Angle α, AFML Shot# 2205
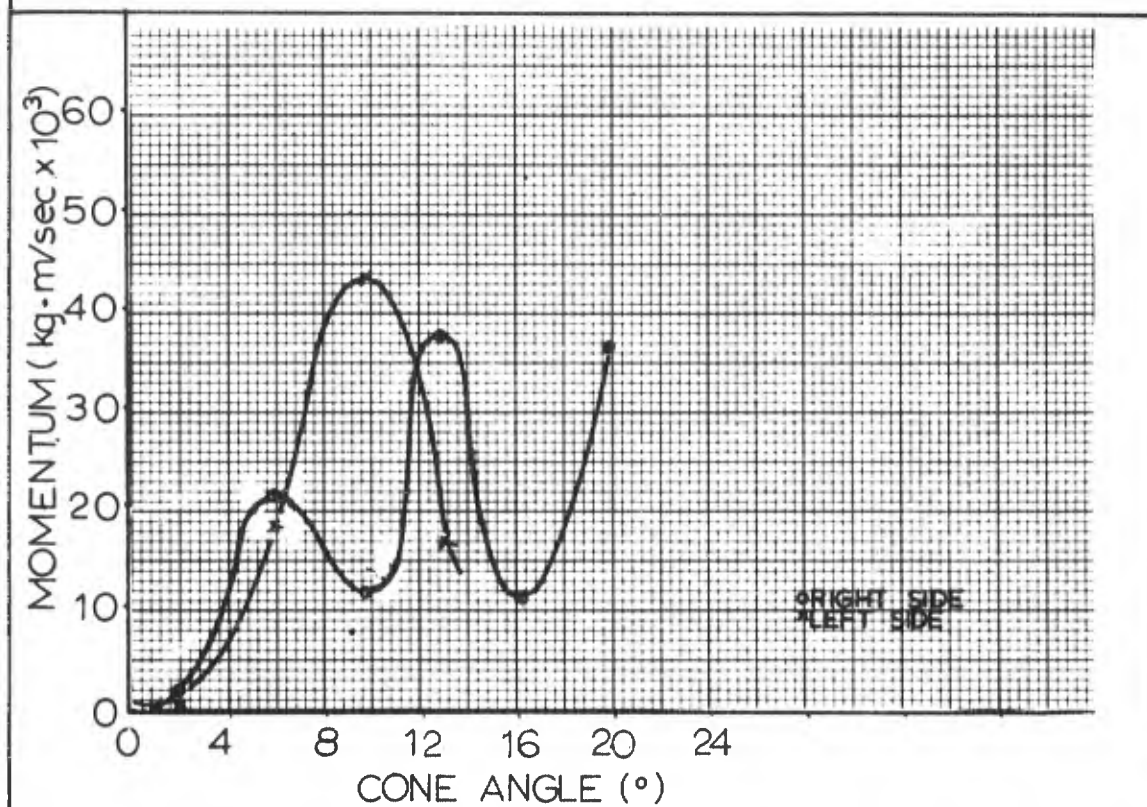
Figure 38 - Momentum vs Cone Angle α, AFML Shot# 2205
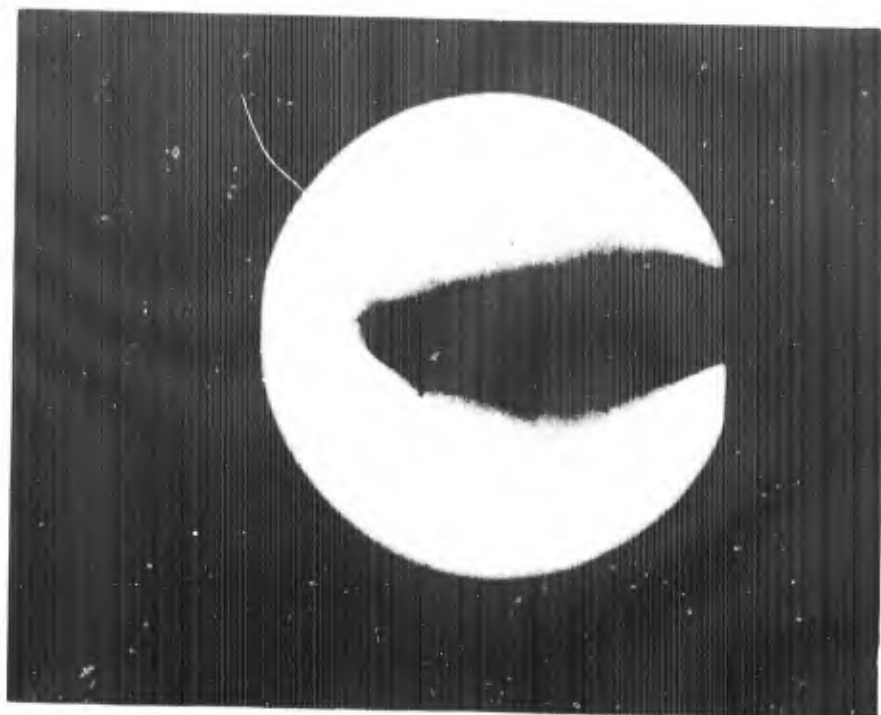
Figure 39 - Photograph of Sliced Debris Cloud
AFML Shot# 2205

b.   AFML Shot #1022 - A 1/8" diameter copper projec-
tile impacted a 1/16" copper sheet at a velocity of 6,560
ft/sec. Figures 40 and 41 show the random scattering of
the debris particles and the wide range of particle size.
The delay between X-ray firings was 24.70 microseconds.
No attempts were made to calculate the cloud velocity for
this shot. The cratering in the witness plates was also
asymmetric, and the craters were not even approximately
hemispherical. No energy, energy density, mass, and mo-
mentum calculations could be made using the technique de-
veloped in this study. Figure 42 shows the debris after
passing through the splitter plate. Range pressure was
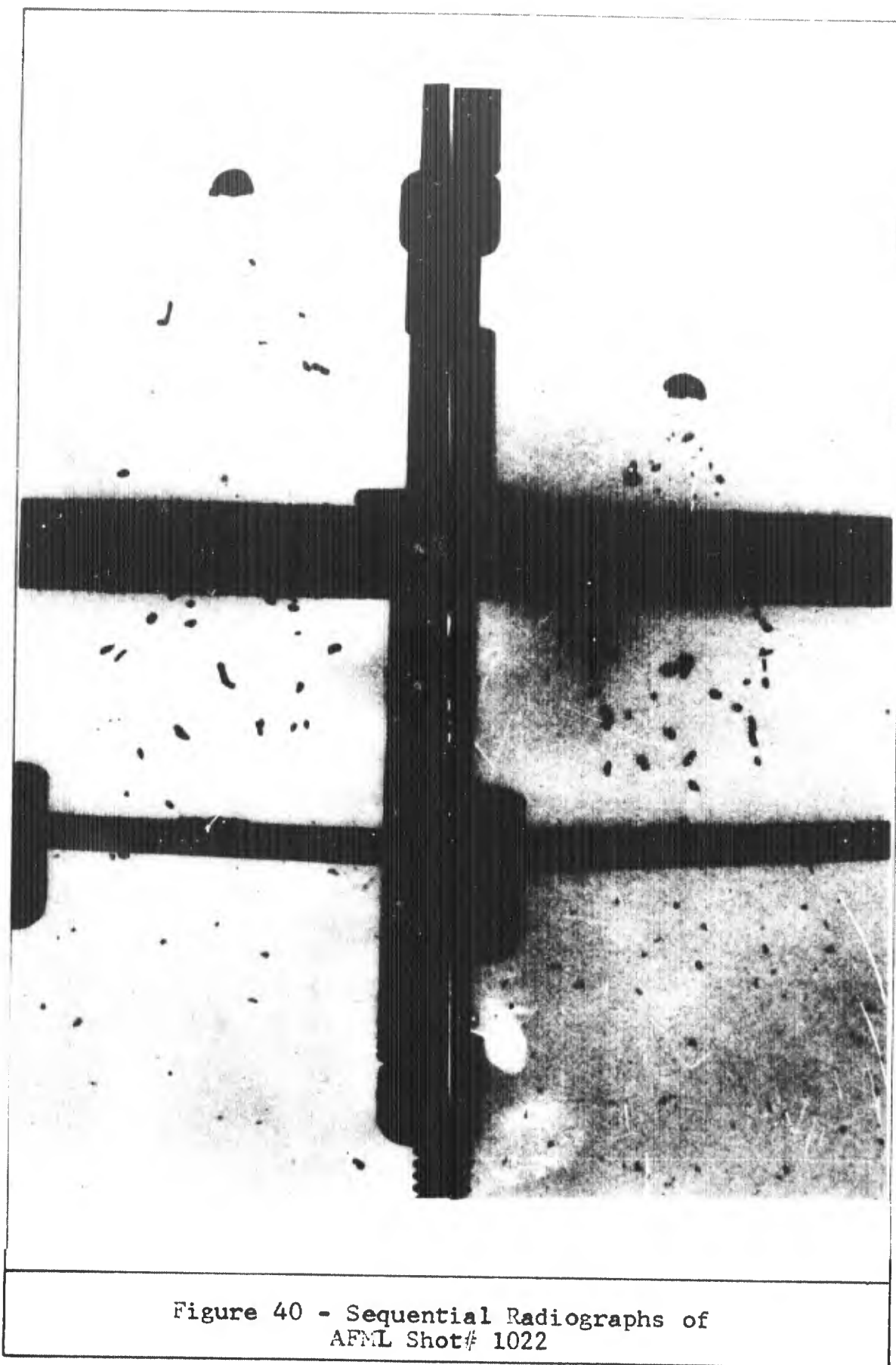
Figure 40 - Sequential Radiographs of
AFML Shot# 1022

BLACKENED PARTICLES
APPEARED IN SECOND
RADIOGRAPH

Figure 41 - Corrected Geometry of Debris Clouds
AFML Shot# 1022
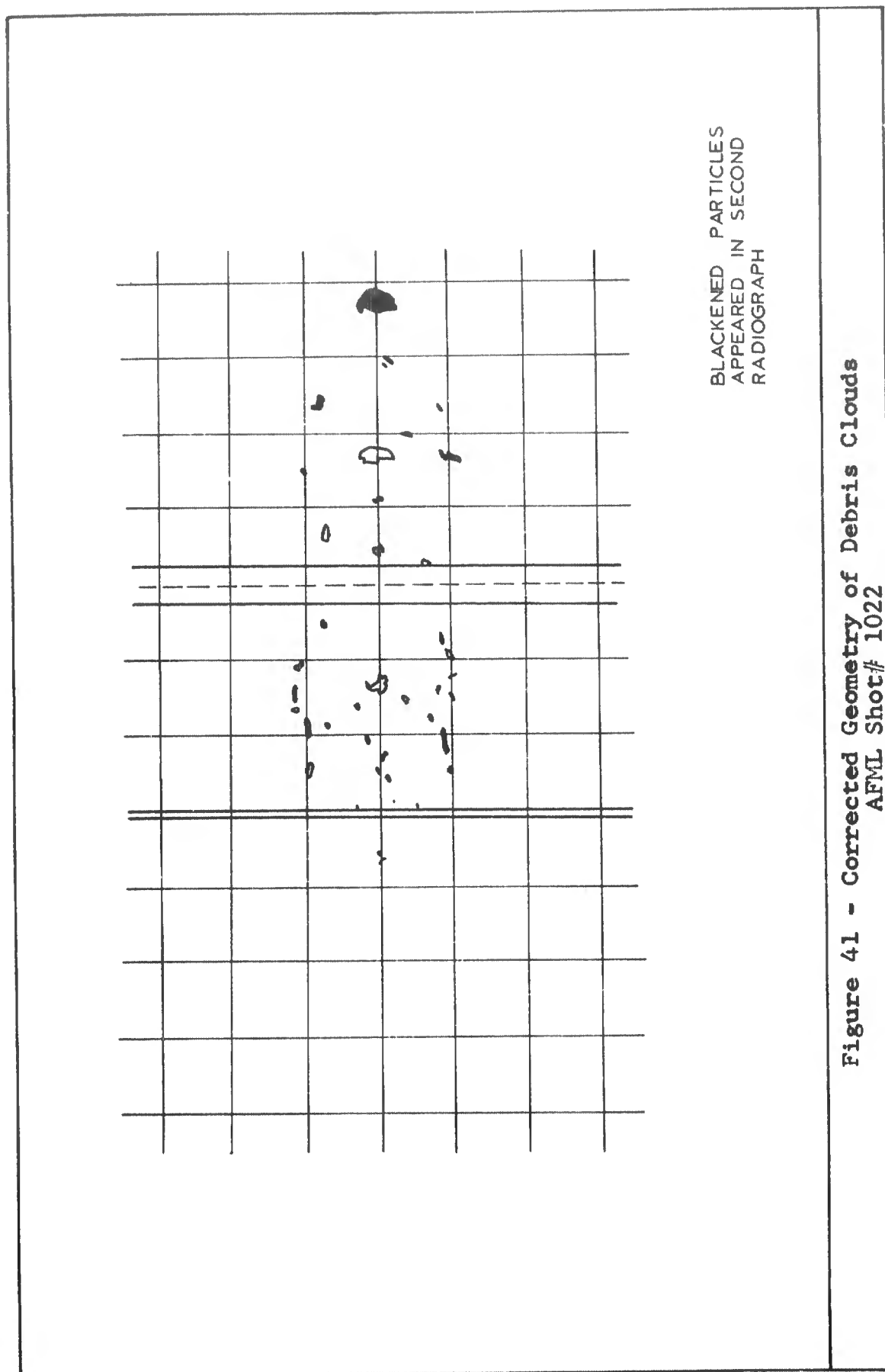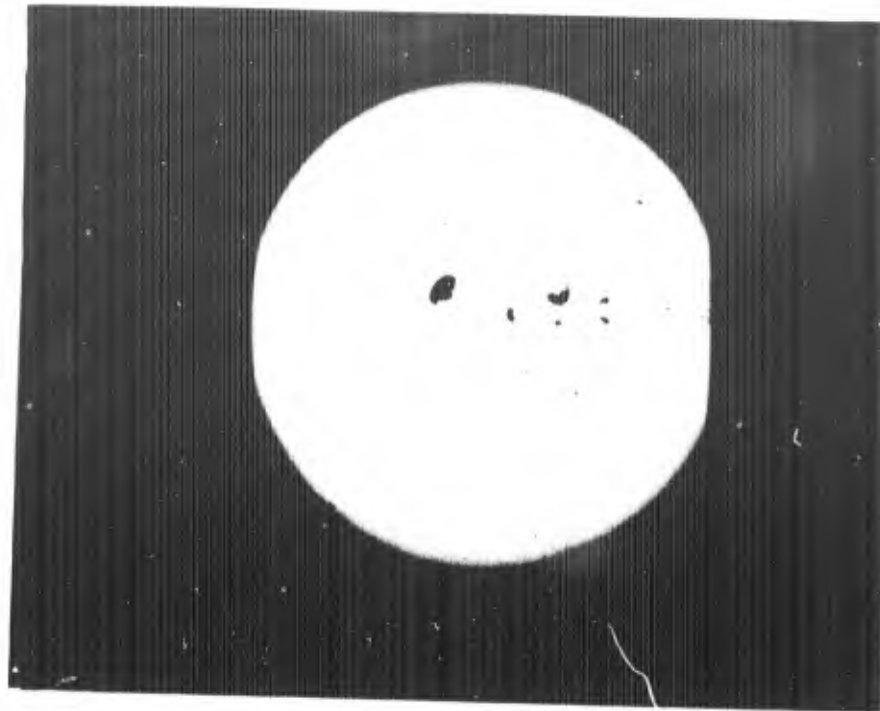
Figure 42 - Photograph of Sliced Debris Cloud
AFML Shot# 1022

atmospheric for this shot which accounts for the bow wave on the leading particle. No vapor phase is evident. Table II predicts no melting for impacts below 15,000 ft/sec.

c. AFML Shot# 2199 - A cadmium sphere impacted a 1/16" cadmium sheet at 21,990 ft/sec. Figure 43 shows radiographs of the cloud taken 3.89 microseconds apart. X-ray 1 appears to have made a triple exposure. The corrected cloud geometry is shown in Figure 44. The results of the cloud velocity measurements are listed in Table XV.
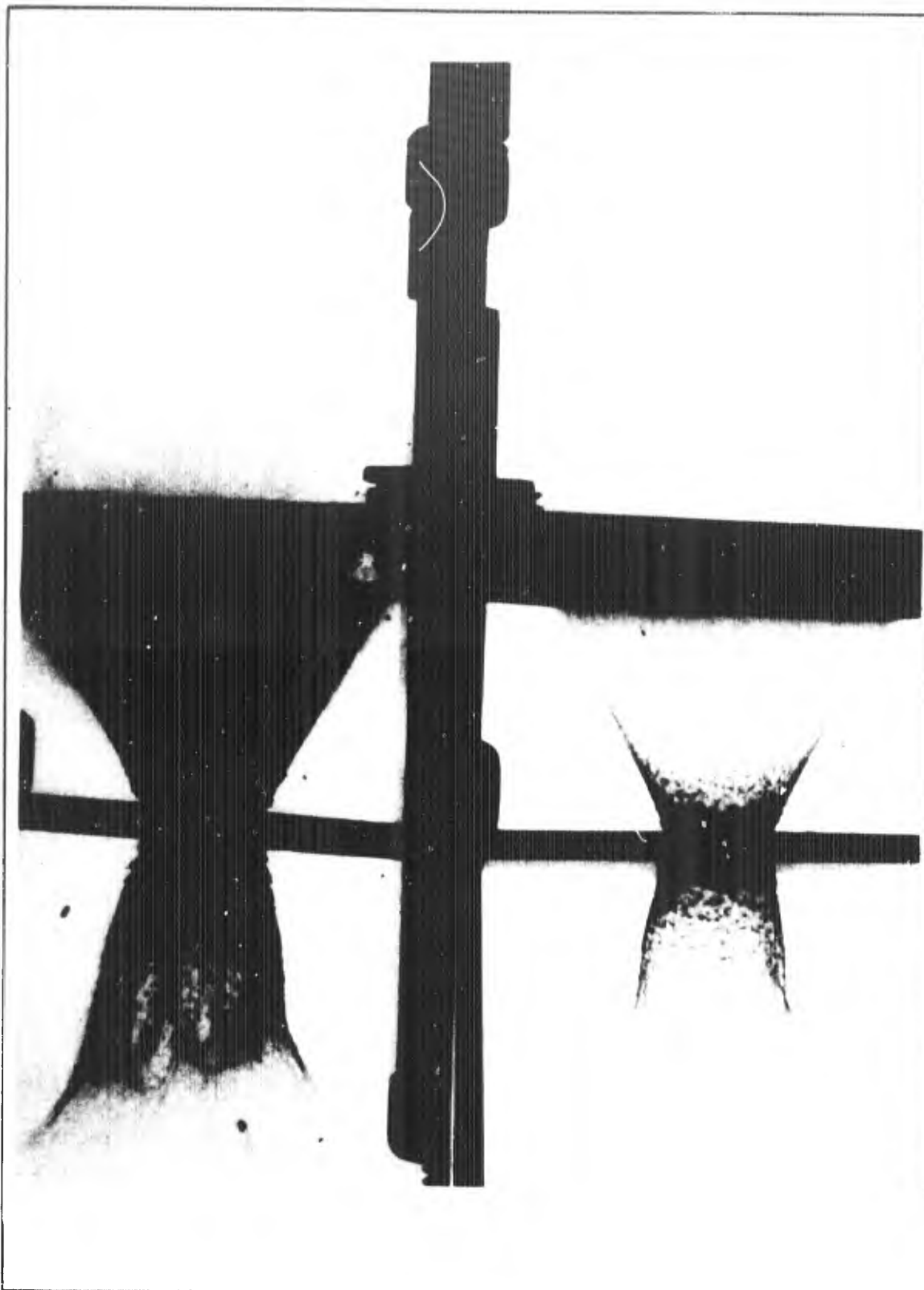
Figure 43 - Sequential Radiographs of
AFML Shot# 2199
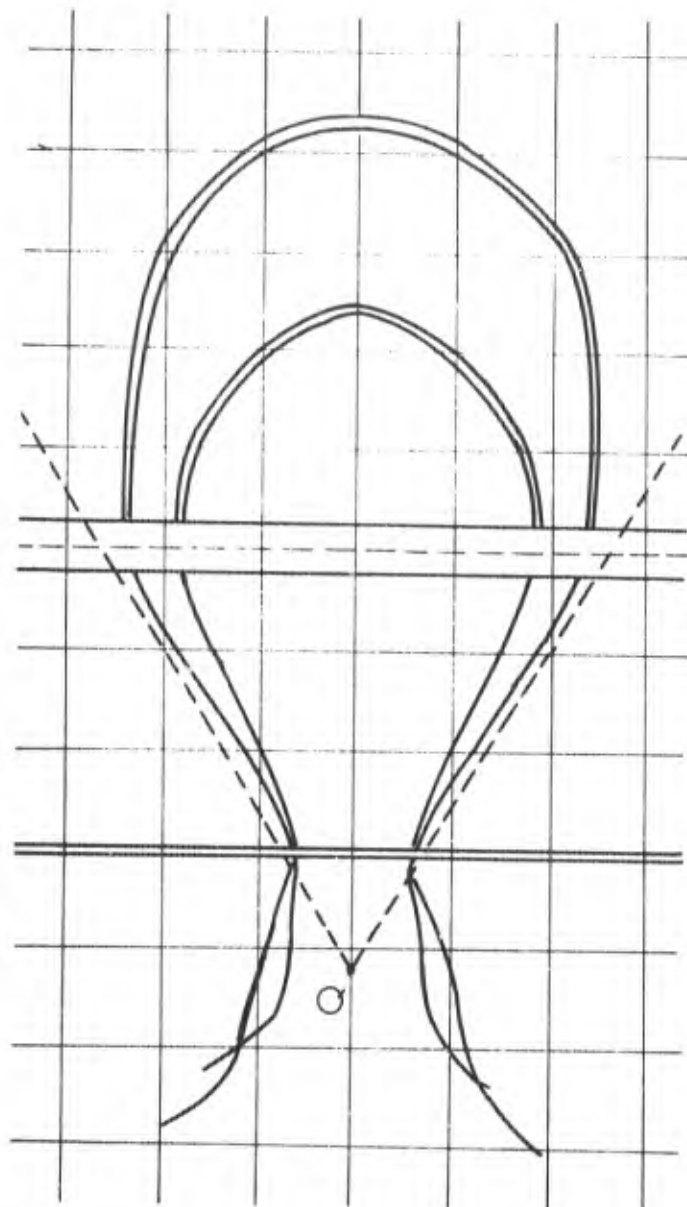
Figure 44 - Corrected Geometry of Debris Clouds, AFML Shot# 2199

α (°)	Distance Traveled (in)	Velocity (ft/sec)
0	0.968	20,736
3.8	0.968	20,736
7.6	0.968	20,736
11.3	0.954	20,437
14.9	0.937	20,072
18.4	0.906	19,408
21.8	0.812	17,395
25.0	0.750	16,066

Results of Cloud Velocity Determination
AFML Shot# 2199

Table XV

The normalized velocity is plotted as a function of α in
Figure 45. Due to the symmetry of the cloud, the velocity
for the right and left sides was identical. No craters
were found on the witness plates after being impacted by
this cloud. Peak pressures generated by impact of the
projectile and bumper were enough to completely vaporize
the cloud debris. No calculations of energy, energy den-
sity, mass, and momentum were possible using the technique
described here. Figure 46 shows the debris cloud emerging
through the splitter plate. The uneven edges of the cloud
are quite evident in this photograph.
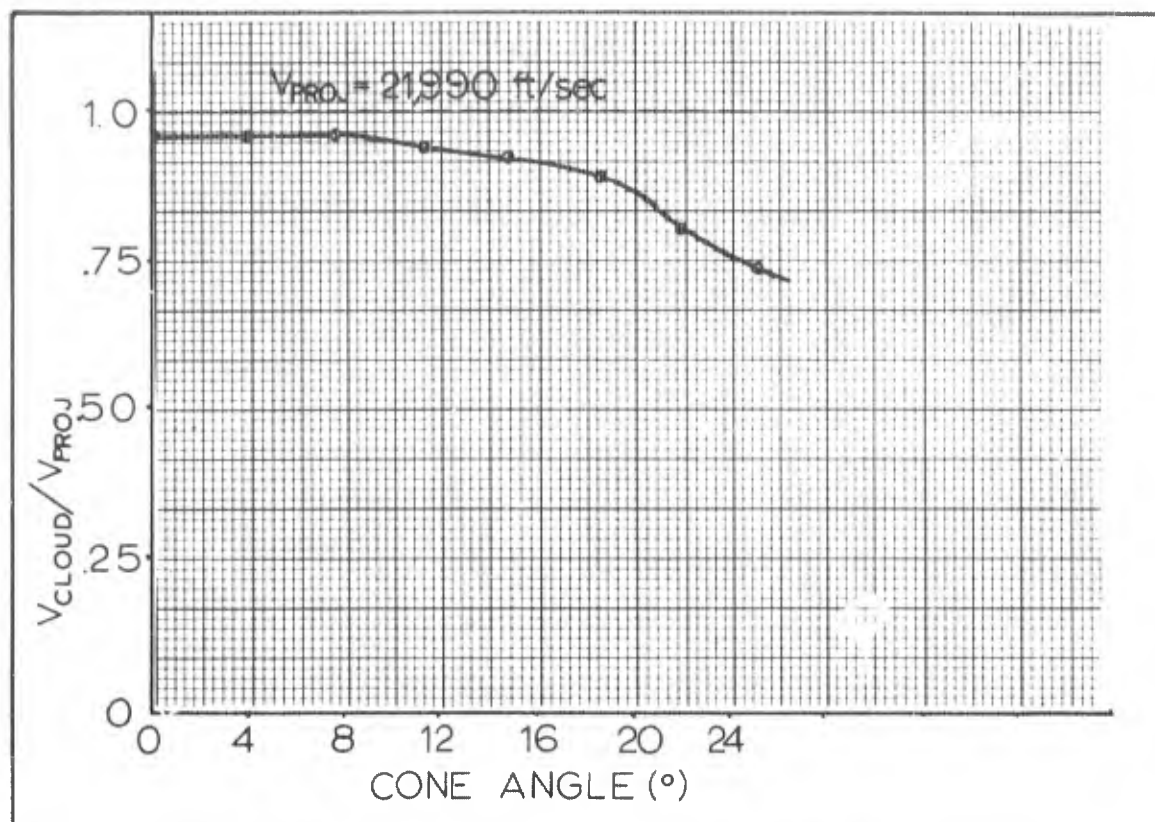
Figure 45 - V Cloud/V Projectile vs α
AFML Shot# 2199

Figure 46 - Photograph of Sliced Debris Cloud
AFML Shot# 2199

GSF/Mech 67-1

d. <u>AFML Shot# 2214</u> - A cadmium sphere impacted a cad-
mium bumper at 10,481 ft/sec. Figure 47 shows the radio-
graphs taken at a time interval of 10.288 microseconds.
Table XVI lists the results of the cloud velocity calcu-
lations.

α (°)	Distance Traveled (in)	Velocity (ft/sec)
0	0.968	7.840
3.9	0.953	7.719
7.7	0.921	7.460
11.5	0.906	7.338
15.2	0.875	7.087
18.7	0.843	6.828
22.1	0.781	6.325
25.4	0.750	6.075

Results of Cloud Velocity Determination
AFML Shot# 2214

Table XVI

Table XVII lists the results of the energy and energy
density calculations. Table XVIII gives the sectors and
the corresponding α- ranges. Er and energy density are
plotted in Figures 50 and 51 as a function of cone angle.
Table XIX lists the results of the mass and momentum cal-
culations for shot# 2214.
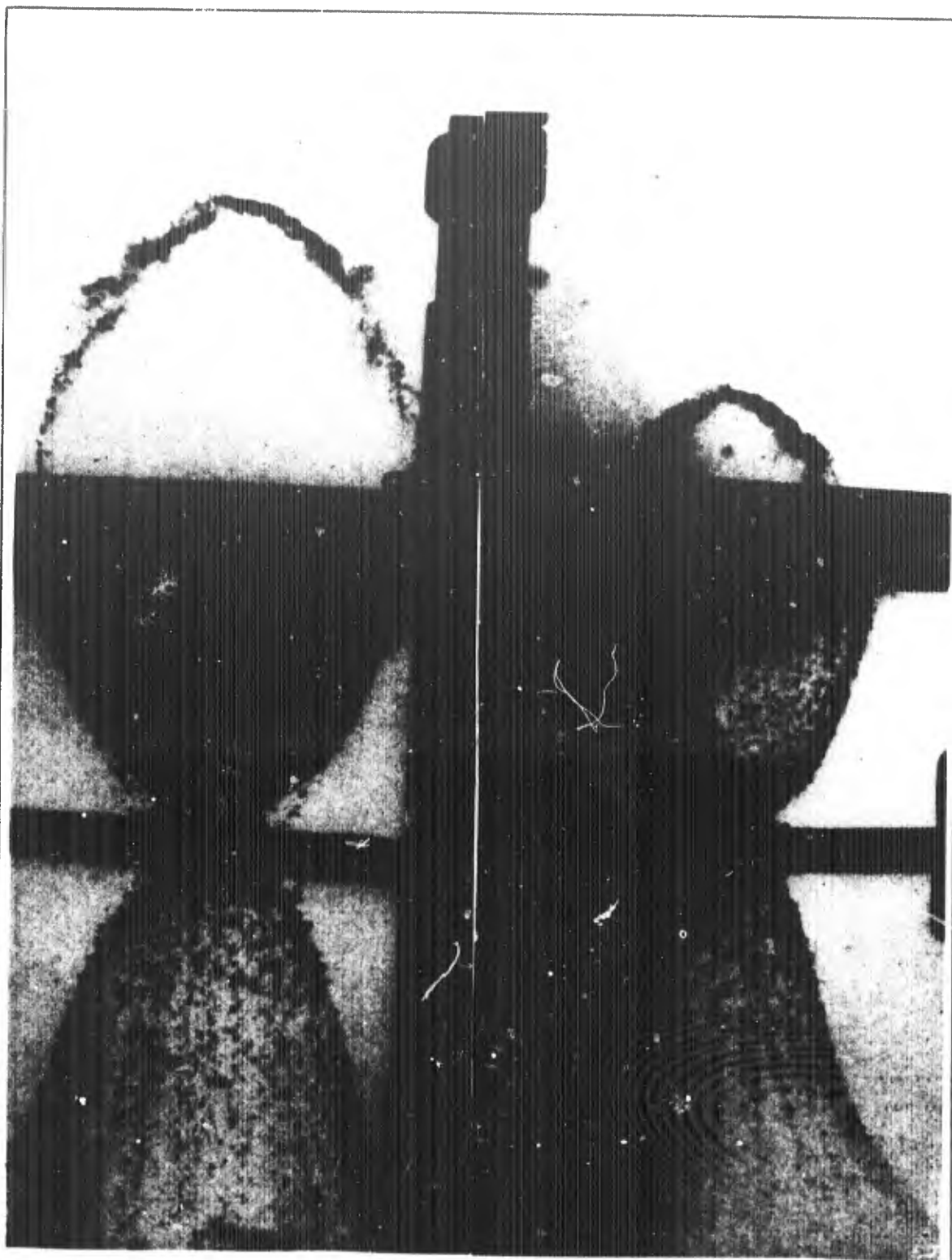
Figure 47 - Sequential Radiographs of
AFML Shot# 2214
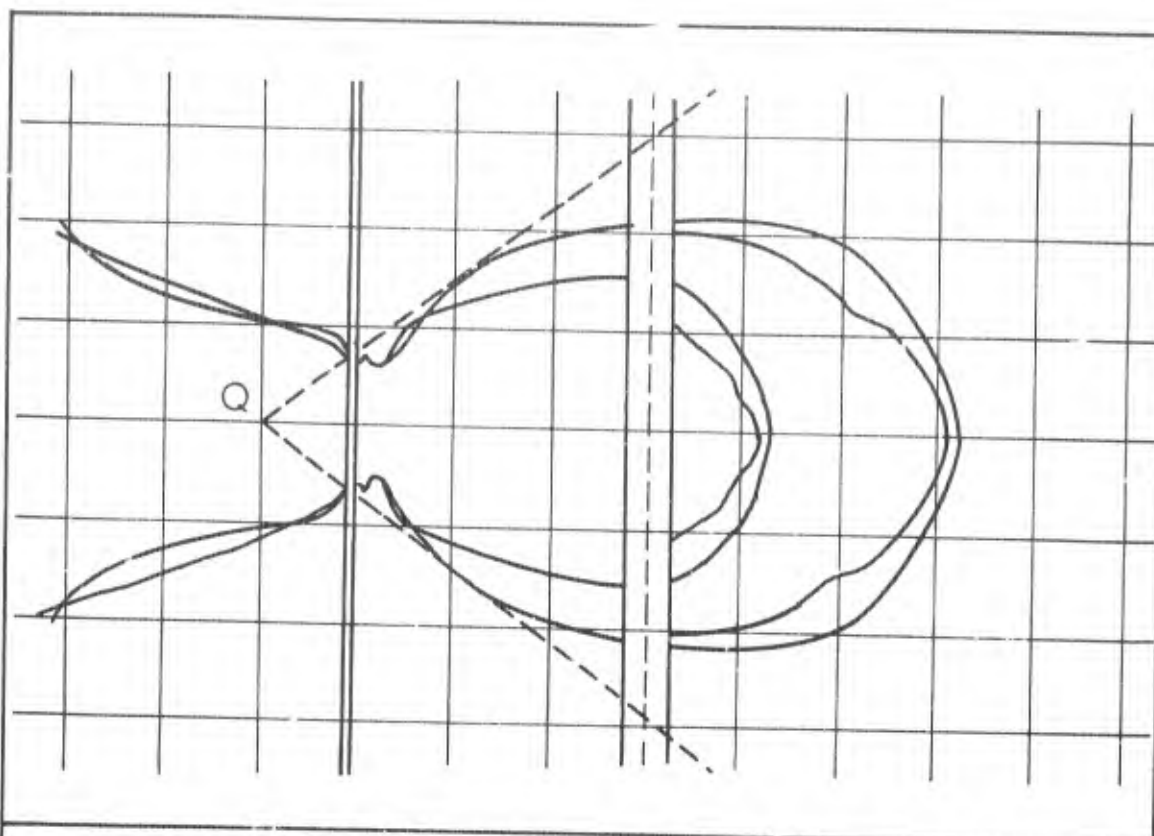
Figure 48 - Corrected Geometry of Debris Cloud
AFML Shot# 2214
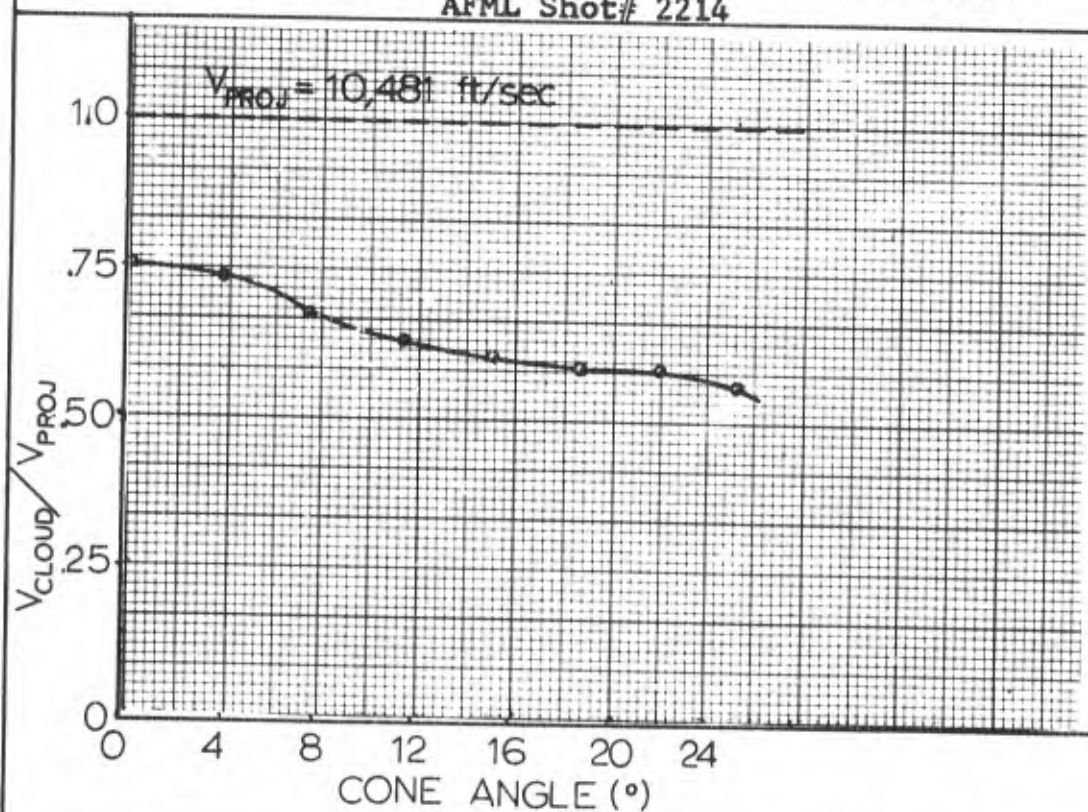
Figure 49 - V Cloud/V Projectile vs ∝
AFML Shot# 2214

	Left Side					Sector	Right Side				
A_s (in2)	A_r (in2)	E_s (joules)	E_r (joules)	Density E (j/in2)	A_r/A_s		A_s (in2)	A_r (in2)	E_s (joules)	E_r (joules)	Density E (j/in2)
0.439	1.49	0.014	0.048	0.032	3.40	1	0.131	0.44	0.005	0.017	0.0382
0.598	4.45	0.014	0.104	0.024	7.45	2	0.179	1.33	0.006	0.045	0.0335
0.683	7.42	0.007	0.076	0.010	10.85	3	0.204	2.21	0.066	0.717	0.323
0.695	10.40	0.007	0.105	0.010	14.98	4	0.207	3.09	0.006	0.090	0.0290
0.710	13.35	0.069	1.300	0.097	18.80	5	0.212	3.96	0.014	0.263	0.066
0.727	16.35	0.036	0.81	0.050	22.51	6	0.218	4.87	0.081	1.821	0.372

Energy and Energy Density
AFML Shot# 2214

Table XVII

Sector	α - Range (°)
1	0 - 3.9
2	3.9 - 7.7
3	7.7 - 11.5
4	11.5 - 15.2
5	15.2 - 18.7
6	18.7 - 22.1

Sectors and Corresponding α - Ranges
AFML Shot# 2214

Table XVIII

Mass and momentum as a function of cone angle are plotted in Figures 52 and 53, respectively. Figure 54 is a photograph of the cloud emerging through the splitter plate. The edges of the cloud are more nearly straight than was the case for Shot# 2199. Table II predicts possible incipient vaporization for the impact velocity of 10,481 ft/sec.

e. AFML Shot# 1025 - A 1/8" cadmium sphere impacted a 1/16" thick cadmium bumper at 3,336 ft/sec. Figure 55 depicts the corrected cloud geometries. This drawing was derived from the sequential radiographs shown in Figure 56. The interval between X-ray triggering was 34.302 microseconds. The asymmetry of the cloud precluded calculations of cloud velocity. Therefore, calculations of energy,
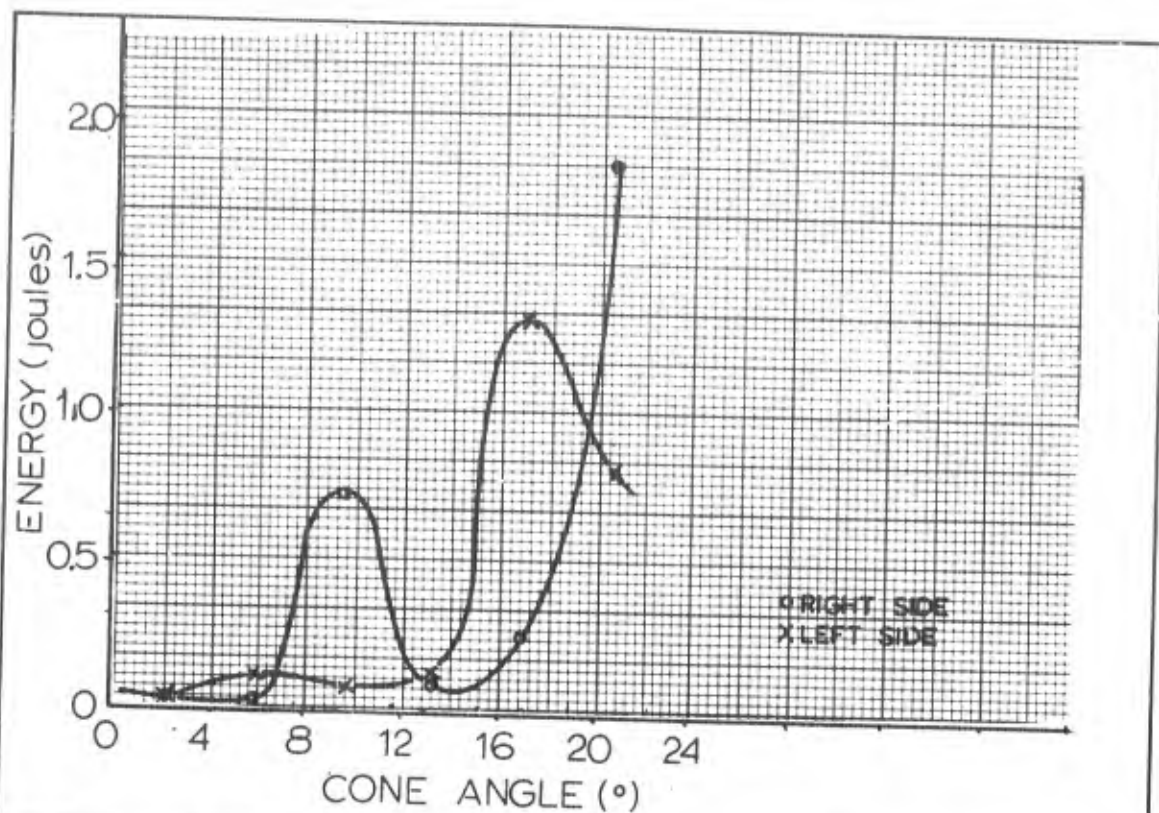
Figure 50 - E_r vs Cone Angle α, AFML Shot# 2214
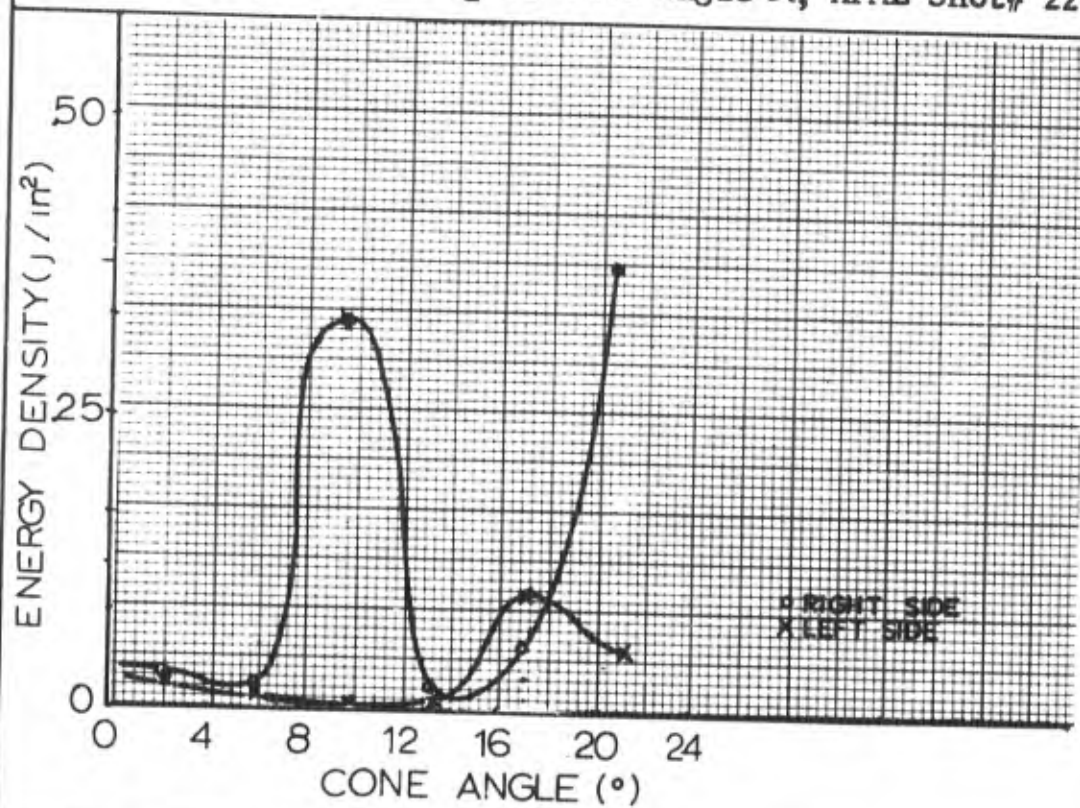
Figure 51 - Energy Density vs Cone Angle α
AFML Shot# 2214

Left Side		Sector	V_A (m/sec)	Right Side	
M_r (mg)	I_r (kg-m/secx10^3)			M_r (mg)	I_r (kg-m/secx10^3)
0.0172	0.0041	1	2.37x10^3	0.00596	0.0014
0.0367	0.0084	2	2.36x10^3	0.0159	0.0038
0.030	0.0675	3	2.25x10^3	0.284	0.641
0.044	0.0965	4	2.19x10^3	0.038	0.0833
0.568	1.141	5	2.12x10^3	0.113	0.231
0.400	0.805	6	2.01x10^3	0.875	1.76

Mass and Momentum
AFML Shot# 2214

Table XIX
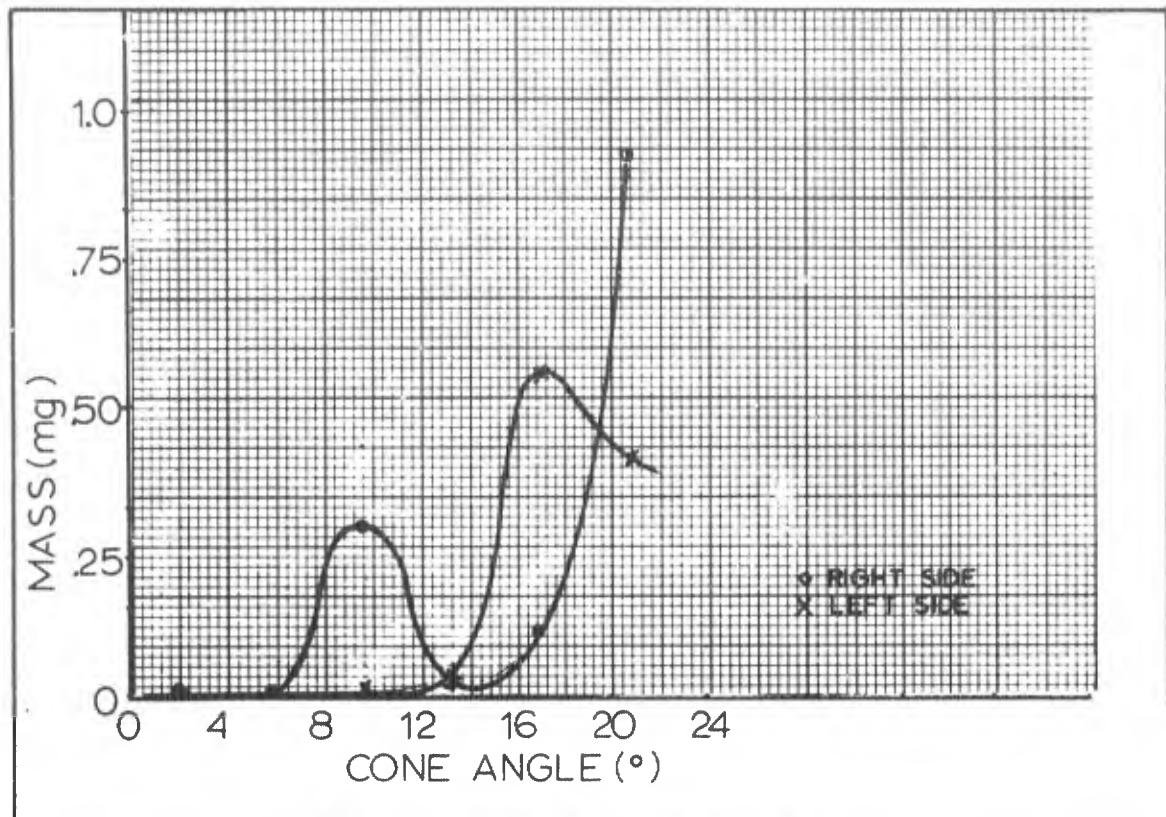
Figure 52 - Mass vs Cone Angle $\propto$
AFML Shot# 2214
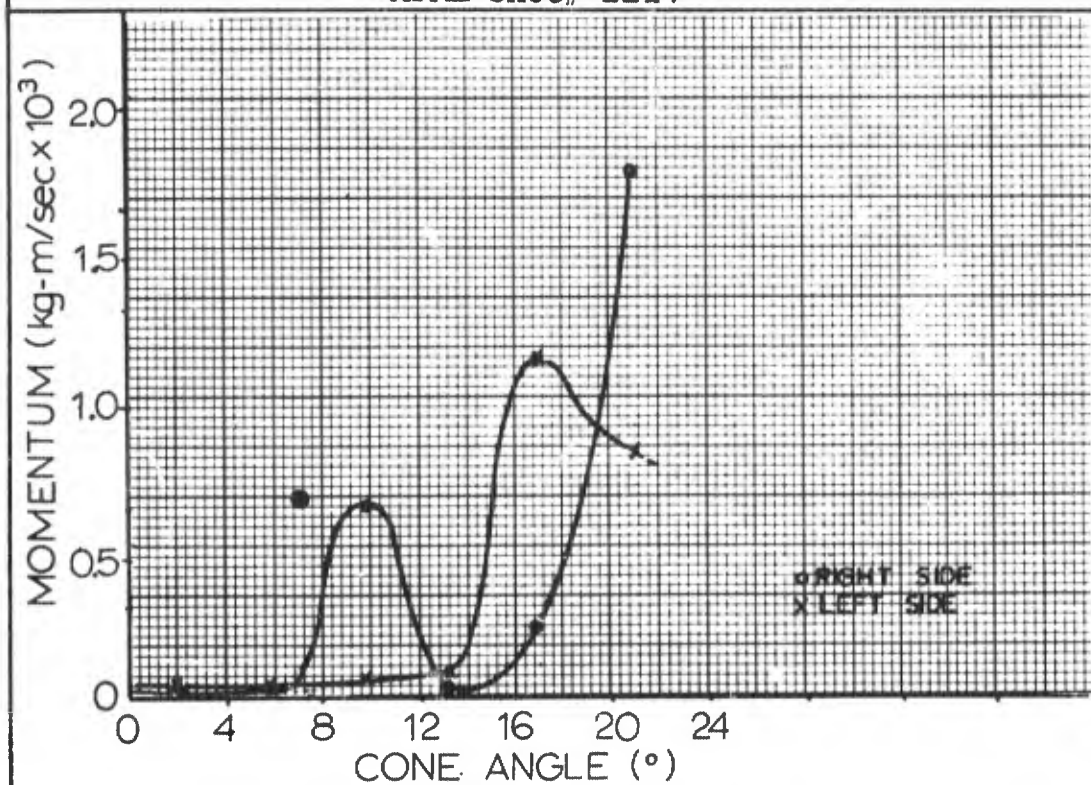
Figure 53 - Momentum vs. Cone Angle $\propto$
AFML Shot# 2214
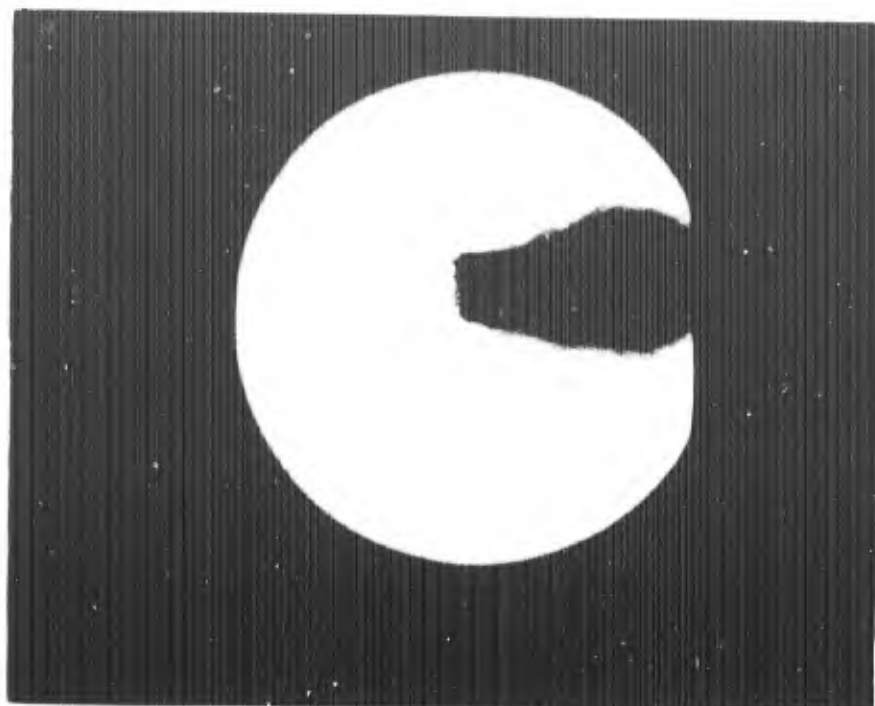
Figure 54
Photograph of Sliced Debris Cloud, AFML Shot# 2214
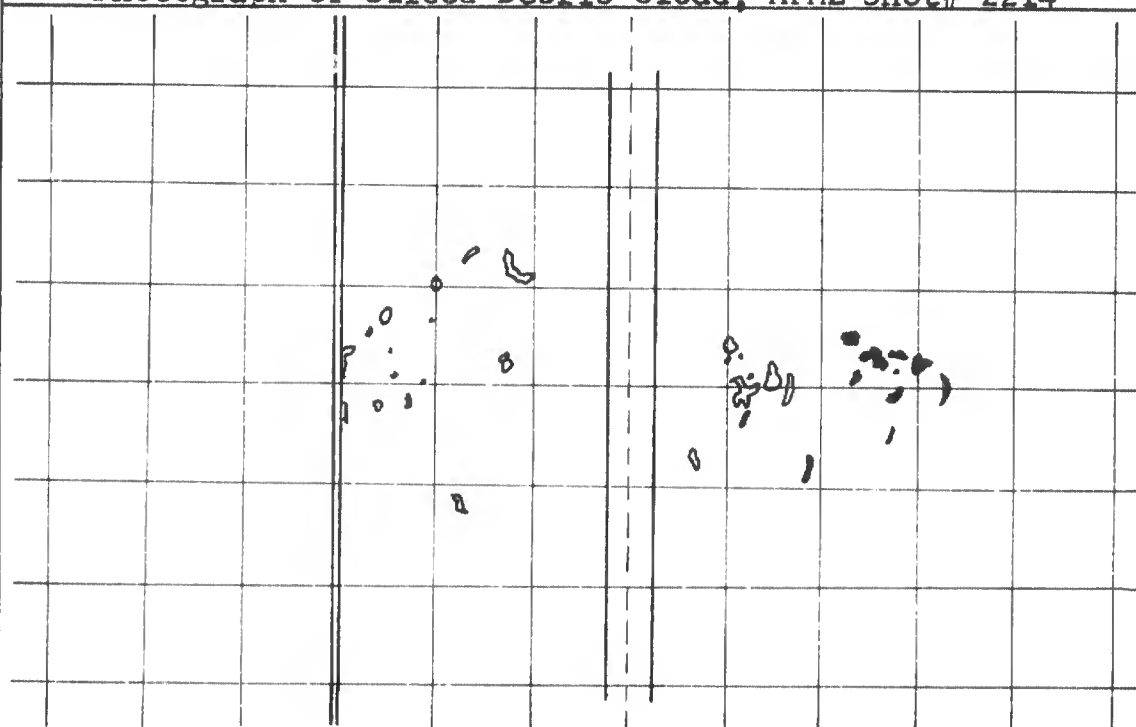
BLACKENED PARTICLES AS
IN SECOND RADIOGRAPH

Figure 55
Corrected Geometry of Debris Clouds, AFML Shot# 1026
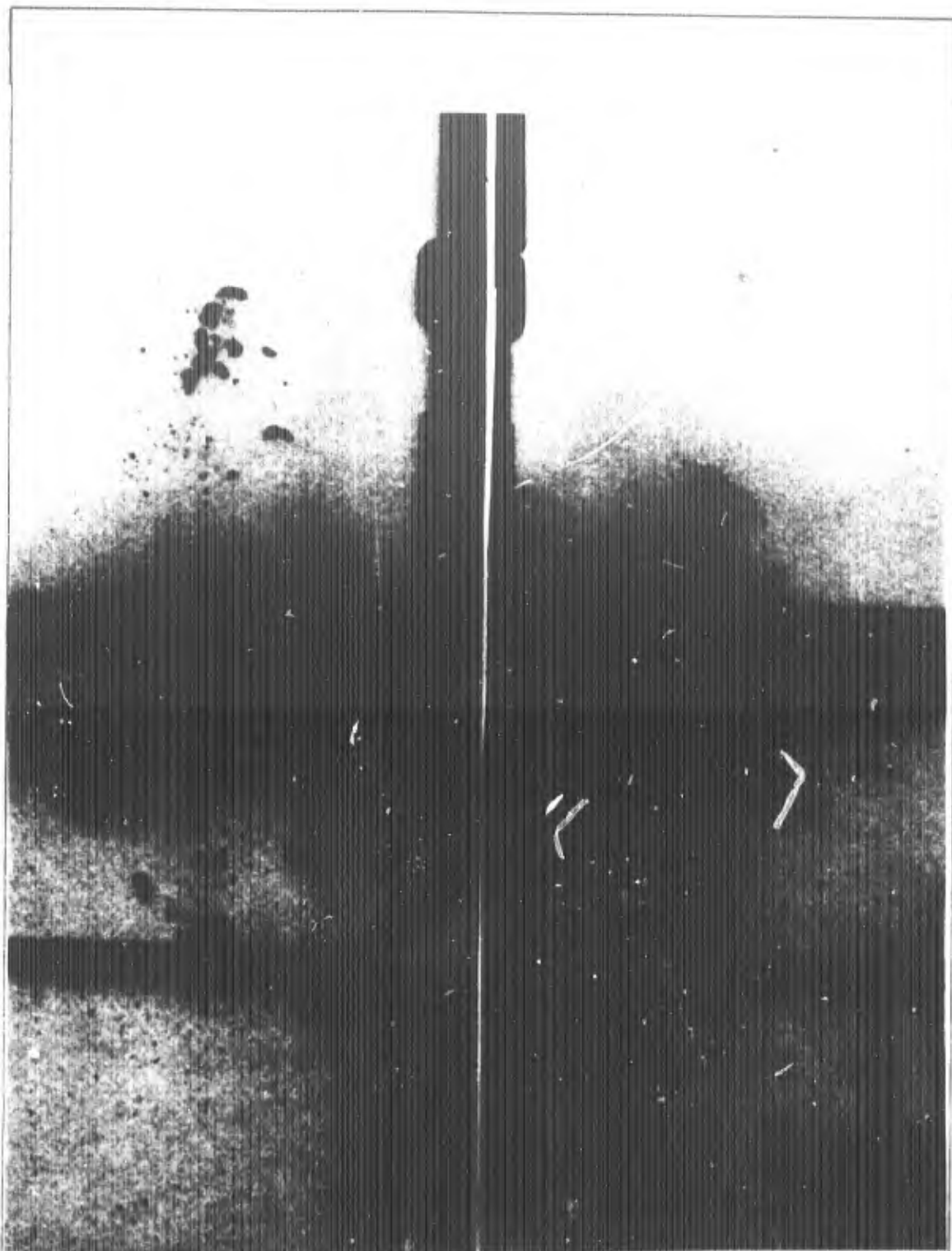
Figure 56
Sequential Radiographs of AFML Shot# 1026
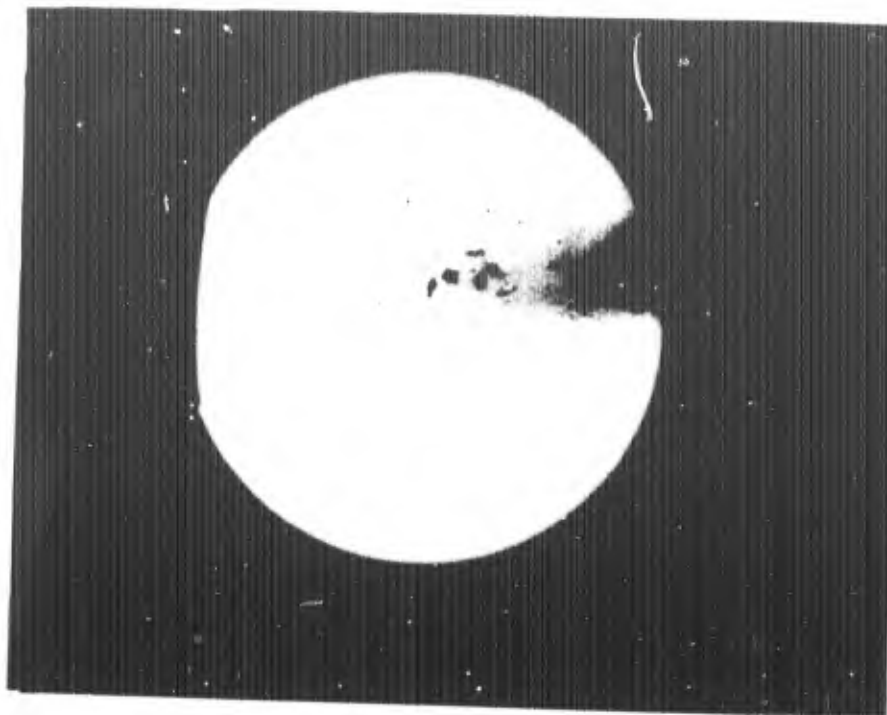
Figure 57
Photograph of Sliced Debris Cloud, AFML Shot# 1026

energy density, mass and momentum were not made. Figure 57 shows the debris moving in straight lines. Only solid particles are predicted in Table II.

f. Bumper Hole Diameters - The diameters of the holes in the bumpers were measured. Nomenclature for other descriptive parameters are indicated in Figure 58. R_1 is the radius of hemispherical cratering damage on the witness plate over the splitter slot; R_2 is the radius of damage on the right side witness plates; R_M is the maximum hole radius achieved during cloud formation; R_H is the measured hole radius; α_M is the maximum cone angle reached during

Figure 58
Bumper-Debris Cloud Geometry
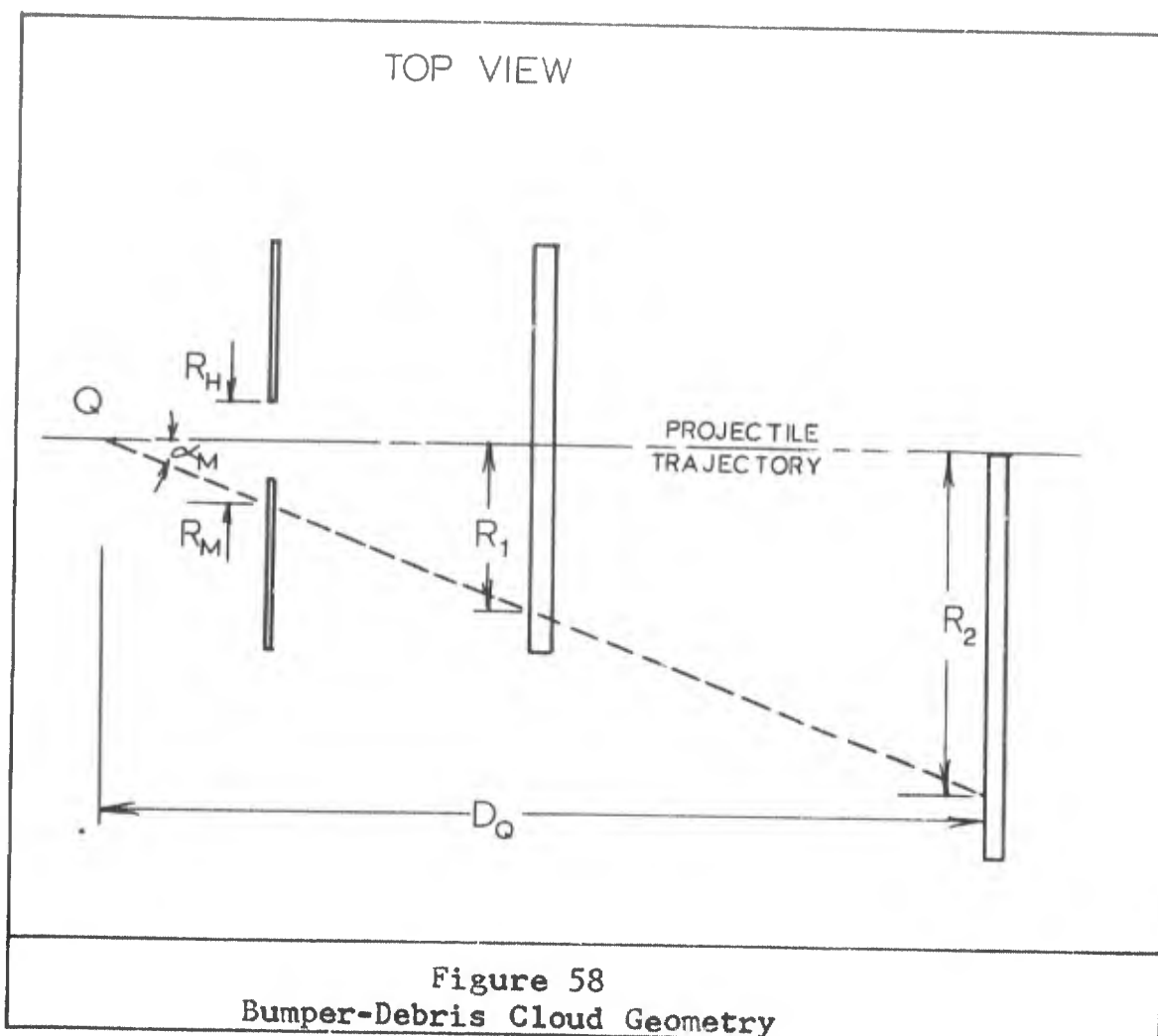
cloud formation; D_Q is the distance from the face of the right side witness plates to point Q. The parameters are listed for four of the bumper shots in Table XX.

Shot No.	α_M (o)	R_1 (in)	R_2 (in)	R_H (in)	R_M (in)	RM/RH	D_Q (in)
2209	35.5	1.250	4.122	0.218	0.311	1.425	5.594
2205	34.2	1.250	3.505	0.187	0.293	1.570	5.660
2199	32.9	1.125	3.625	0.281	0.295	1.050	5.625
2214	36.7	1.250	4.125	0.218	0.276	1.265	5.530

Bumper Hole Calculations

Table XX

III. Discussion of Results
and Conclusions

The calculations of cloud velocities were made with
two implicit assumptions. The first is that the particles
are moving in straight paths along lines constructed
through a point Q which remains stationary throughout cloud
development. No data is available to confirm this position.
It was not possible to compare the computations with those
of other experimentors because of the definition of cone
angle supplied in this study. The calculations also
assume a constant particle velocity in the cloud. Appen-
dix C contains calculations which show that atmospheric
drag is not an apreciable slowing mechanism on solid par-
ticles. No calculations were made as to the ablative
effects of the atmosphere, or the action of aerodynamic
forces on liquid droplets or fractured solid particles.
In spite of these possible weaknesses, however, the velo-
city profiles agree with the trend evident in sequential
radiographs. Axial expansion of the cloud is much faster
than radial expansion and the slowest particles are ex-
pected to be traveling along a path determined by the
maximum cone angle.

The energy calculations are strongly biased by many
factors. It must be remembered that only the energy in

solid and liquid phases is measured by this technique.
The low energy values at the center of the cloud are par-
ticularly intriguing. No significant amount of crater
overlap on the witness plates near the range axes was
noted. However, these central portions of damage also
correspond to regions of high densities of craters with
diameters below 0.05 mm. Inclusion of these craters in
the calculations might bring the energy value up by as much
as 25%. Energy calculations are based directly on the
volumes of observed craters. The absence of craters due
to impact by a gaseous cloud does not imply that the cloud
has no damage potential (see Appendix B - AFML Shot# 2125).
The technique developed is limited to cloud energy mani-
fested by cratering. Finally, no scaling of particle
size was attempted. Various techniques are available
(Ref 9 and 11), but were beyond the scope of investigation.
The overlapping of the left and right energy, energy den-
sity, mass, and momentum curves is another interesting
result. The clouds may not possess the symmetry of par-
ticle distribution suggested by their geometry. AFML
Shot# 2205 produced an asymmetric cloud. The energy shifts
noted may be due to particle breakup by ablation or rapid
tumbling.

The extent of hole growth was calculated for the thin
plate study. The clouds were all apparently devoid of
particles inside a thin-walled bubble shell. This suggests

that after the initial penetration occurs along the projectile trajectory, the region near the edge of the hole is the sole source of cloud particles, whether they are bumper or projectile material. Rolsten has previously reported the hole growth phenomena with an attendant "relaxation" of the material (Ref 22). The results of this study show agreement that such a phenomena is occurring. Table XX shows possible shrinkage as much as 36% for Shot# 2205, which is hardly believable. The difference between the amount of shrinkage for the Cu - Cu impacts (Shots 2209 and 2205) and the Cd - Cd shots does appear significant, in view of the relative physical strengths of the material. Also, note that for both materials, less shrinkage occurred following higher impacting velocities. The cloud splitter plate gave only marginal indications as to the presence of vapors in the cloud. If the detector functioned properly, then vapors are produced when not expected, notably in Shot# 2205. The impact velocity of 4.45 km/sec is just above that required for incipient melting (see Table III). The upper uneven edge of the cloud slice could be caused by material impacting the inner walls of the splitter plate slot. The impact point of Shot# 2205 was 7/32" above the range axis, so particles in the downward moving cloud could impact the lower slot wall.

Caron reports that oxidative detonations were ob-

served in a 98% H_e - 2% O_2 atmosphere at 14.7 psi (Ref 4). This suggests that the uneven edges viewed may be due to vapor production by localized burning at the cloud edges. A similar detonation probably occurred in the high-velocity Cd - Cd shot (see Appendix B - AFML Shot# 2125). The liquid phase could not be distinctly detected. The scheme to measure a change in average crater diameter with increasing distance from the bumper gave no coherent results. If the breakup of material in flight occurs, the solid particles would probably be just as likely to break up as the liquid droplets.

In the preliminary tests (see Appendix B), several catcher materials were tried, but no cloud particles were successfully recovered. However, 6" of shaving cream did prevent damage in the bottom of a tin can (see Appendix B - AFML Shot# 2190).

IV. Recommendations

With regard to the technique developed, four improvements might increase the reliability of the data.

a. Anneal the target materials to insure similar strength parameters.

b. Thicker witness plates should be used. Bowing of the plates was noted, particularly in Shot# 2209.

c. The downrange edge of the splitter slot should be beveled off. This would present a sharp edge to the cloud and prevent deflections of cloud particles as possibly occurred in Shot# 2205.

d. The range atmospheric pressure should be further decreased and an inert gas such as helium used to replace the air. This would minimize ablation and the possibility of burning of cloud particles.

e. Further work should be done to study the hole growth phenomena. A splitter plate in which at least three slots have been cut should prove useful in such an effort. Extrapolation of particle paths back to the bumper should provide hole radius as a function of time.

f. High speed cameras might be used to detect cloud particle breakup. A very narrow slot in a splitter plate might permit a thin cloud slice to pass through. Photographs could possibly reveal particles breaking as they

travel downrange.

g. A target system in a calorimetric device might enable calculations to be made of the energy contained in the cloud.

h. The use of low density substances to prevent impact damage due to particles in the mass range 10^{-7} to 10^{-5} grams is encouraged. A rigidizing styrofoam may be useful for this purpose.

Bibliography

1. Bjork, R. L., "Review of Physical Processes in Hypervelocity Impact and Penetration", RAND Corporation, RM-3529-PR, July 1963.

2. Bjork, R. L., and Olshaker, A. E., "The Role of Melting and Vaporization in Hypervelocity Impact", The RAND Corporation, RM-3490-PR, May 1965.

3. Burbank, P. B., Cour-Palais, B. G., and McAllum, W. E., A Meteoroid Environment for Near-Earth Cislunar, and Near-Lunar Operations, NASA TN-D-2747, April 1965.

4. Caron, A. P., "Oxidative Detonations Initiated by High Velocity Impacts", AFFDL-TR-65-41, May 1965.

5. Charters, A. C., Gehring, J. W., and Maiden, C. J., "Impact Physics, Meteoroids, and Spacecraft Structures", AGARDograph 87, Vol. 1, The Fluid Dynamics of Space Flight, Gordon & Breach, Science Publishers, New York, 1958.

6. Corcoran, J. W., "Shock Pressure Measurement by Streak Photography - A Photo Manometric Technique", presented at the Society of Photographic Instrumentation Engineers at New York City, 7 Aug 1962.

7. Courant, R., and Friedricks, K., Supersonic Flow and Shock Waves, Interscience Publishers, New York, 1948.

8. Dallavalle, J. M., Micrometrics, Pitman Publishing Corporation, New York, 1948.

9. Denardo, B. P., and Nysmith, C. R., "Momentum Transfer and Cratering Phenomena Associated with the Impact of Aluminum Spheres into Thick Aluminum Targets at Velocities to 24,000 Feet Per Second", AGARDograph 87, Vol. 1, The Fluid Dynamics of Space Flight, Gordon & Breach, Science Publishers, New York, 1958.

10. Duvall, G. E., "Shock Waves in Solids", International Science and Technology, pp. 45-52, April 1963.

11. Eichelberger, R. J., Allison, F. E., and Donaldson, W. F., "Craters Formed by High-Velocity Fragments", Fundamentals of Shaped Charges, Chapter I, Carnegie Institute of Technology, Pittsburgh, Pa., July 1954.

12. Eichelberger, R. J., and Gehring, J. W., "Effects of Meteoroid Impacts on Space Vehicles", _ARS Journal_, Vol. 32, No. 10, pp. 1583-1591, October 1962.

13. Goldsmith, W., _Impact_, Edward Arnold Ltd., London, 1960.

14. _Handbook of Engineering Fundamentals_, Eshbach, O. W., ed. Wiley & Sons, Inc., New York, 1952.

15. Hildebrand, Joel, H., _Kinetic Theory_, Reinhold Publishing Company, New York, 1963.

16. Kuethe, A. M., and Schetzer, J. D., _Foundations of Aerodynamics_, John Wiley & Sons, Inc., New York, 1961.

17. Lee, John F., Sears, Francis W., and Turcotte, Donald L., _Statistical Thermodynamics_, Addison Wesley Publishing Company, Inc., Reading, Mass., 1963.

18. Maiden, C. J., and McMillan, A. R., "An Investigation of the Protection Afforded a Spacecraft by a Thin Shield", _AIAA Journal_, Vol. 2, No. 11, pp. 1992-1998, November 1964.

19. Maiden, C. J., McMillan, A. R., and Sennett, R. E., _Thin Sheet Impact_, NASA CR-295, September 1965.

20. McQueen, R. G., and Marsh, S. P., "Equations of State for Nineteen Metallic Elements from Shock Wave Measurements to two Megabars", _Journal of Applied Physics_, Vol. 31, No. 7, 1960.

21. Rice, M. H., McQueen, R. G., and Walsh, J. M., "Compression of Solids by Strong Shock Waves", _Solid State Physics_, Vol. 6, ed. by Seitz and Turnbull, Academic Press, Inc., New York, 1958.

22. Rolston, R. F., Wellnitz, J. N., and Hunt, H. H., "An Example of Hole Diameter in Thin Plates Due to Hypervelocity Impact", _Journal of Applied Physics_, Vol. 35, No. 3, pp. 556-559, March 1964.

23. Skidmore, I. C., "An Introduction to Shock Waves in Solids", _Applied Materials Research_, Vol. 4, No. 3, pp. 131-147, July 1963.

24. Swift, J. F., "The Air Force Materials Laboratory Hypervelocity Ballistic Range", Technical Report AFML - TC-67-2, January 1967.

25. Truitt, R. W., _Hypersonic Aerodynamics_, The Ronald Press, Co., New York, 1959.

26. Whipple, F. L., _Possible Hazards to a Satellite Vehicle_, Project RAND, Douglas Aircraft Corporation, Santa Monica, Calif., 1946.

27. Zwartz, Frank, J., "The Initial One Dimensional Expansion of the Shocked States Generated by the Impact of Cylindrical Pellets with Thin Plates", NASA TN-64-6, Jan. 1965.

Appendix A

Description of Equipment

The Air Force Materials Laboratory (AFML) hypervelocity ballistic range was used in this investigation. A complete facility description is contained in Reference 24. A brief description of those portions of the light gas gun and instrumentation which were important in this study is included here. The overall facility is pictorically described in Figure 59.
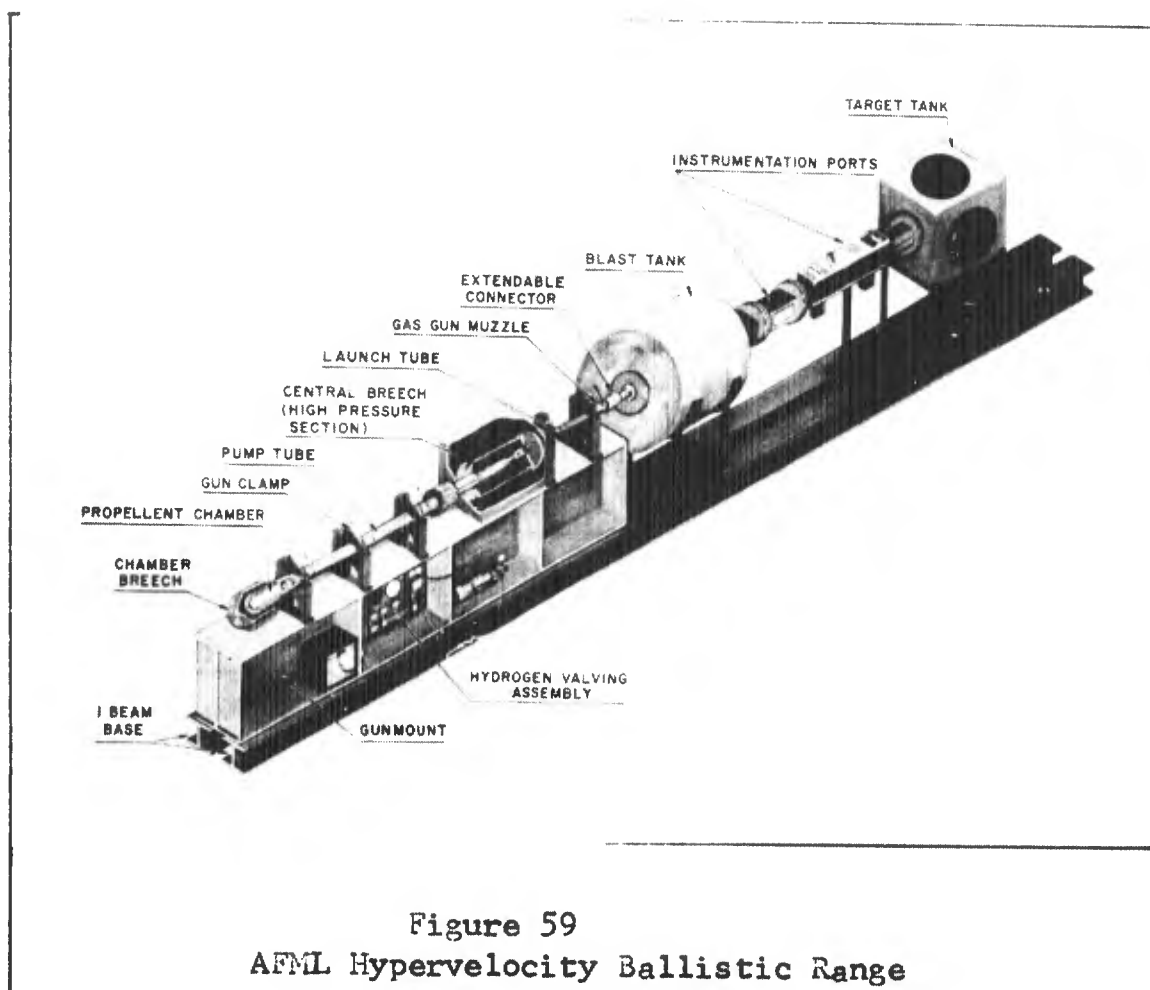
Figure 59
AFML Hypervelocity Ballistic Range

1. AFML Light Gas Gun

The Air Force Materials Laboratory light gas gun has
the present capability of accelerating projectiles up to
1 gram in mass to velocities of 7.65 km/sec. The chamber
accepts a 40 mm MK4 propellant casing with a steel piston
projectile (see Figure 60). A screw breech contains a
firing pin which is actuated by an electric solenoid. The
pump tube (1.63" ID, 71" long) contains hydrogen at a
pressure of 265 psi.

Figure 60
AFML Light Gas Gun

(Ref 24)
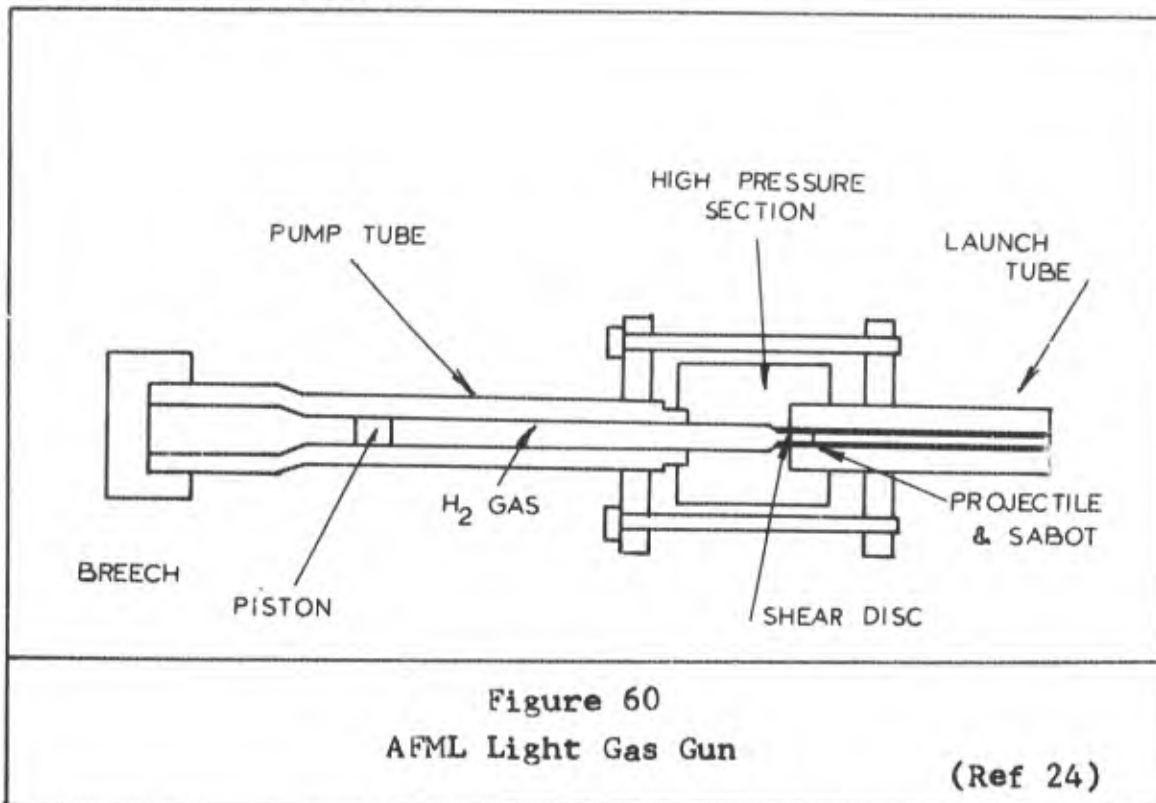
After firing, the piston compresses the gas in the launch
tube and drives it toward the central high pressure section.
The tube inside diameter narrows to .30 caliber in this
section. A 0.020 inch thick aluminum shear disc is placed
at the interface of the .30 cal launch tube and the pump

tube. A full-bore, 5 piece aerodynamic sabot[1] is seated against the shear disc in the launch tube. When the hydrogen gas achieves pressure of 40,000 psi, the sabot containing a spherical projectile is accelerated down the launch tube followed by a plug from the shear disc. Range atmospheric pressure is maintained at 25mm Hg. Experience has shown that this pressure is high enough to insure sabot opening and still produce minimal drag on the projectile. The sabot and sphere enter a tank with baffles to trap muzzle blast. At the down range end of the blast tank, a sabot impact plate allows passage of the projectile through a 1/4" diameter hole, but stops the trailing sabot components and the shear disc plug. The four quadrants of the cylindrical sabot will close the 1/4" opening upon impact, preventing the sabot end cap and shear disc from following the projectile to the target. This closing also seals the propellant gases off from the instrumentation ports.

The light gas gun was fired in three modes to achieve varying velocities. The 40 mm casing is loaded with 180 grams of powder when velocities above 20,000 ft/sec are desired. For velocities between 10,000 - 20,000, this powder load is decreased an amount dependent on the required velocity. For velocities below 10,000 ft/sec, the projec-

---

[1] A sabot is a capsule which holds the sphere during launch. It protects the sphere from barrel friction and provides a seal for the propelling gases. The sabot is separated from the sphere after leaving the launch tube.

tile and sabot are fired from a 30 caliber powder gun.
The projectile proceeds downrange to the target tank, a
2' cube with 5 removable 18" diameter windows. The win-
dows provide access to the target area and may serve as
mounts for targets or instrumentation.
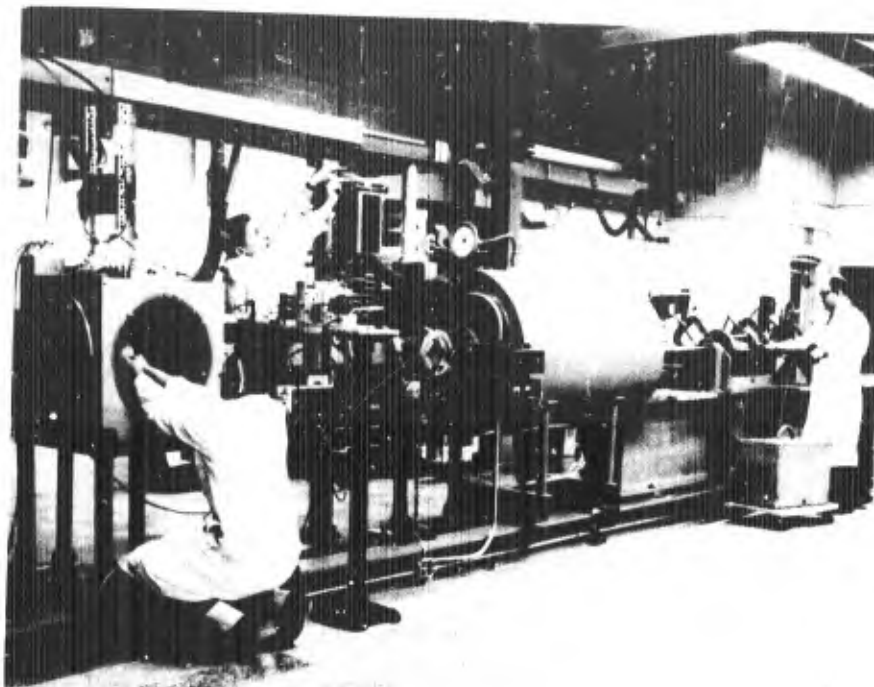
Figure 61
Downrange: Target Tank and Instrumentation

2.   Instrumentation

Image Converter Cameras. Eighteen inches after
emerging from the blast tank, the projectile is photographed
by two image converter cameras with optical axes placed 20
cm apart. These cameras[2] take orthogonal pictures so that

---

[2] Beckman & Whitley Model 500-10 nanosecond exposure time

projectile integrity may be verified and to detect extrane-
ous debris following the projectile. Time elapsed between
photographs is used to compute projectile velocity.

Streak Camera System (Figure 62).

Figure 62
Streak Camera-Winker System   (Ref 24)
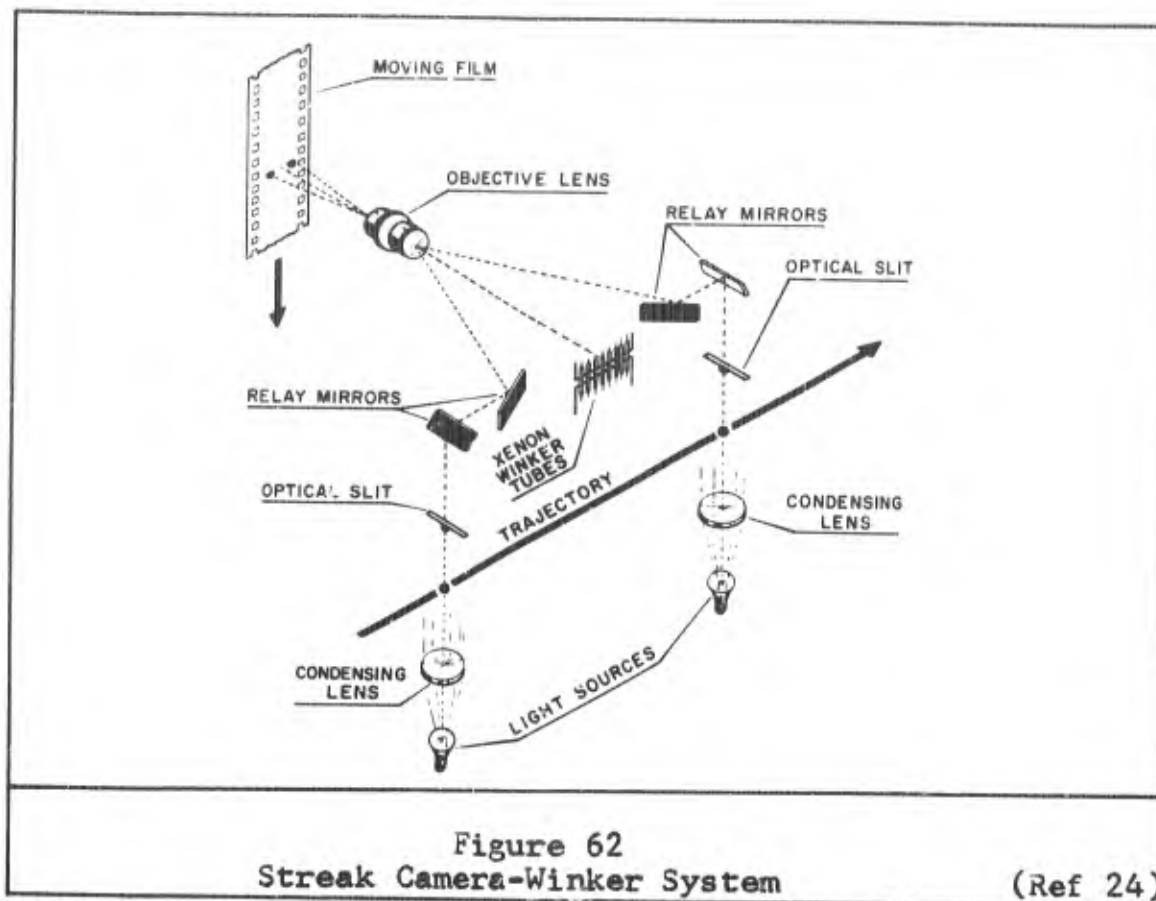
This system consists of a reel-type streak camera[3] focused
on a bank of eight xenon flash lamps. The flash lamps are
discharged by electrical signals originating at instrumen-
tation sites along the range. The signals trigger the flash
lamps, causing small images to appear on the film. A typical

[3] Wollensak 16mm Fastax Camera

event would be the triggering of the image converter cameras previously discussed. Up to eight sequential experimental events may be recorded in positions along the direction of film motion which are directly related to the occurrence of the event in time. Fiducial time markers are also placed in the film at every 100 microseconds so that film speed may be determined. The times between events can be determined to an accuracy of 0.06 microseconds. The film is also aligned with two optical slits placed exactly 2' apart along the projectile trajectory. Light sources beneath the trajectory produce a shadow image of the projectile at two points exactly two feet apart. Since the time between the exposure of the two projectile images is known from the film speed, the velocity of the projectile can be determined to within ± 0.25%.

Flash X-Ray System. Two 105 kv, 30 nanoseconds pulse duration X-ray sources[4] were available to take sequential radiographs of the cloud debris during formation. An input voltage of 27 kv was determined to give the best resolution for the materials used. Kodak Royal Blue Medical film was used with DuPont intensifier screens. Film holders were $4\frac{1}{2}$ x 17" cardboard cassettes clamped between 1/8" and 1/4" sheets of plexiglas.

---

[4] Field Emmission Corporation 105 Kv Flexitron Model 231 System

Electrical Switch. Although not a piece of equipment
per se, the switch performed an integral instrumentation
function and deserves mention. The contact switch (shown
in Figure 63) is made by placing a thin strip of aluminum
foil on a piece of thin mylar mounted on a plate in the
cloud trajectory. The foil is connected to a positive
terminal and the plate to a negative terminal. Care must
be taken to insulate the foil from the plate. Arcs across
1/2" gaps have been observed when a 600 V potential is
impressed on the switch in a 25 mm Hg atmosphere. An in-
coming debris particle will easily penetrate the foil and
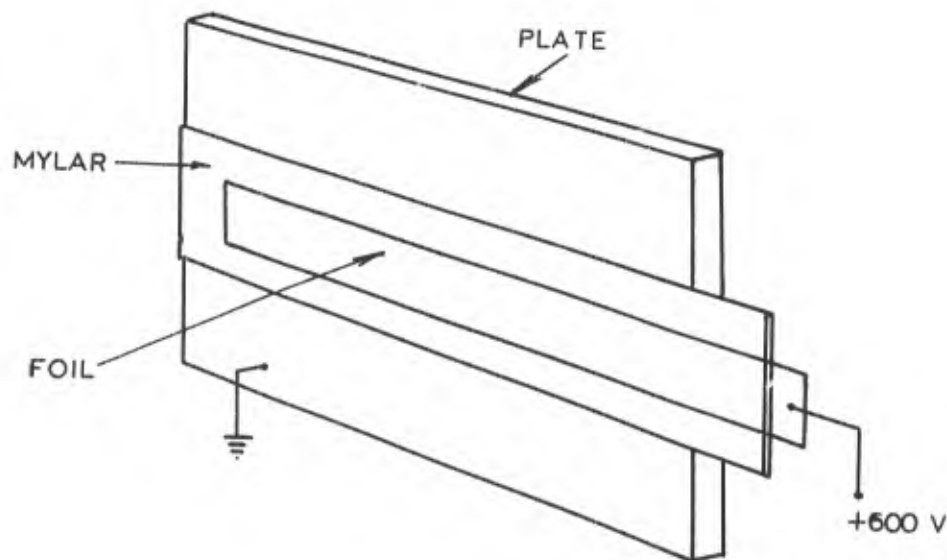mylar, causing the foil to contact the plate which initiates
the xenon lamps.

Figure 63
Electrical Contact Switch

Time Delay Generators. Two time delay generators[5] were utilized to control the initiation of X-ray and photographic equipment at a predetermined time interval after closure of the switch discussed.

---

[5] Electro Optical Instruments Trigger Delay Generator, Model 100.
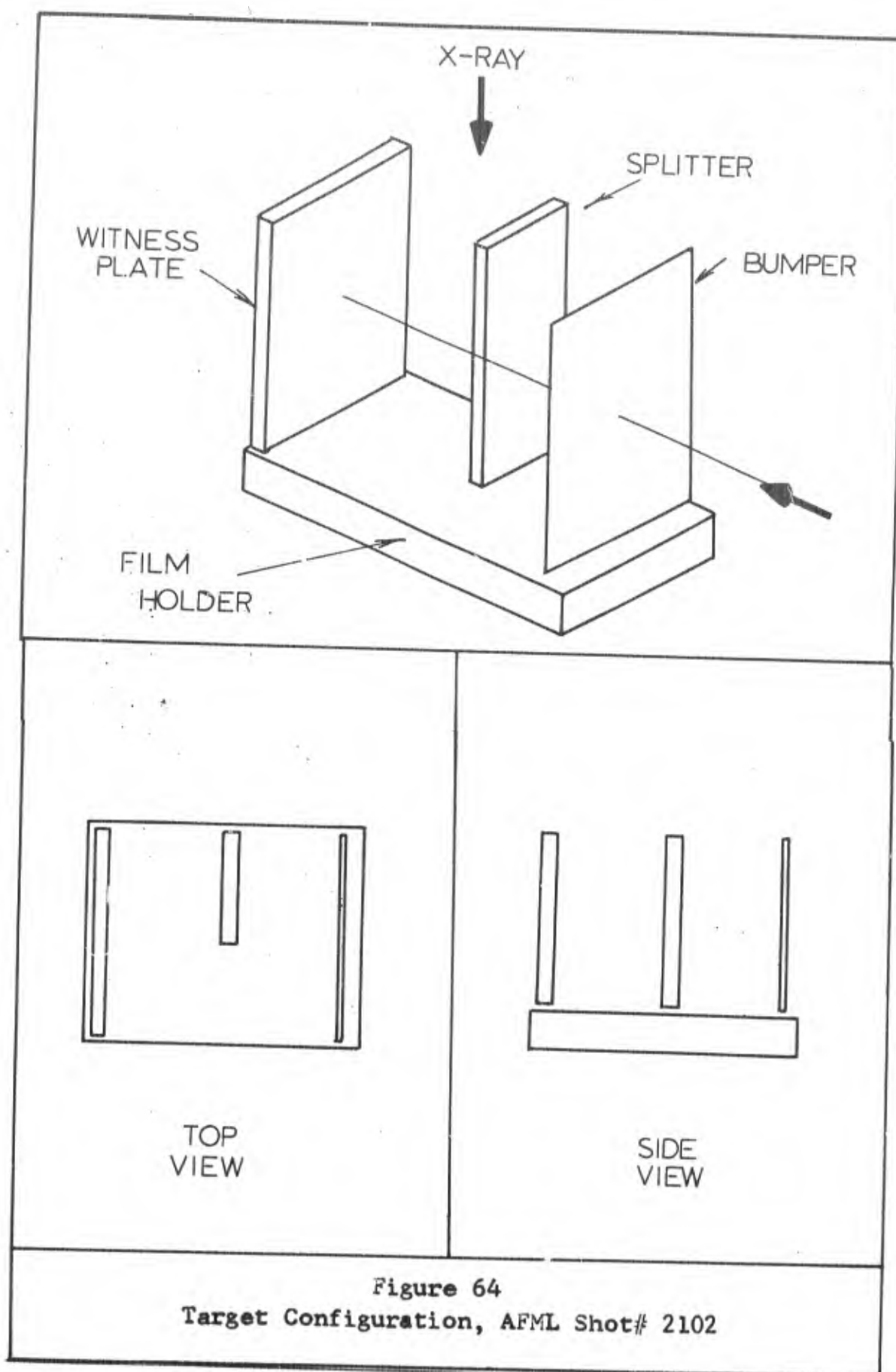
Appendix B

Preliminary Experiments

Some familiarization with the equipment and range
techniques was required of the writer. To gain experience
with possible data collection techniques, a pilot test
program was conducted. Four shots in this series were of
particular value in determining the final experimental
technique.

AFML Shot 2102 (Figures 64 and 65).

The purpose of this shot was to test the passage of
the cloud over a sharp edge. The solid (and possibly liquid)
particles were seen to travel in a straight line past the
plate edge (Figure 65). Gaseous portions of the cloud
do not appear in the radiographs. The gas phase is opaque
to electromagnetic radiation in the visible and will appear
in photographs. These dense metallic vapors are not ex-
pected to travel in straight lines as the solid and liquid
particles do. Comparison of simultaneous photographs and
radiographs should detect any metallic vapors present.

AFML Shot 2117 (Figures 66, 67, and 68).

A 1/8" aluminum sphere impacted a 1/32" copper plate
at 23,100 ft/sec. This shot featured a cloud splitter con-
sisting of a 1/4" steel plate with a 1/4" slit for passage

95

X-RAY

WITNESS
PLATE

SPLITTER

BUMPER

FILM
HOLDER

TOP
VIEW
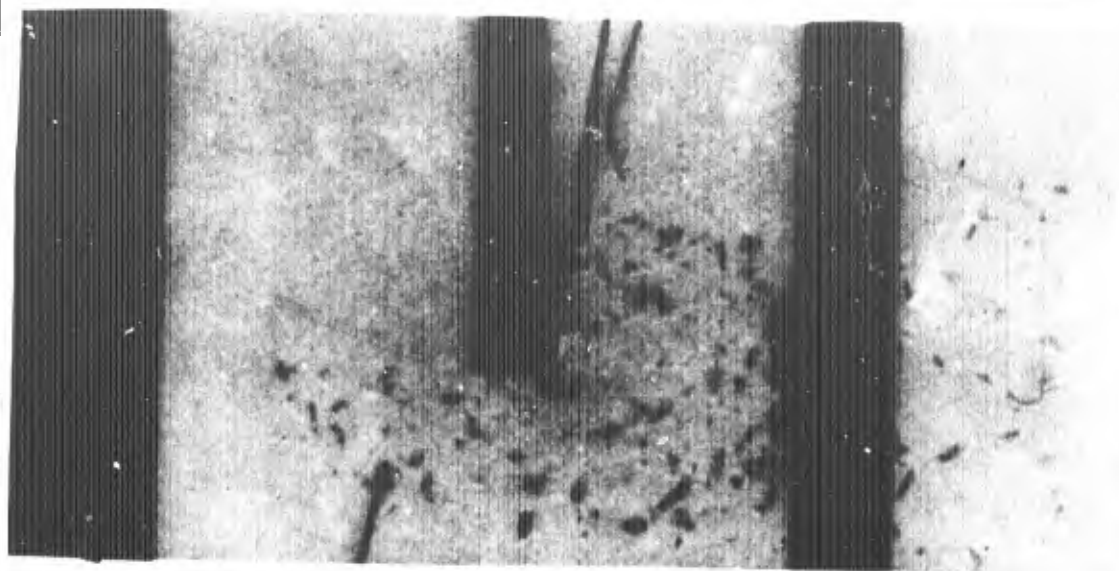
SIDE
VIEW

Figure 64
Target Configuration, AFML Shot# 2102

Figure 65
Radiograph of AFML Shot# 2102

Figure 66
Radiograph of AFML Shot# 2117

WITNESS PLATE

X - RAY

Cloud Splitter

Switches

Capture Hole

FILM HOLDER

Cu bumper

TOP VIEW

SIDE VIEW

Figure 67

Target Configuration, AFML Shot# 2117

Figure 68
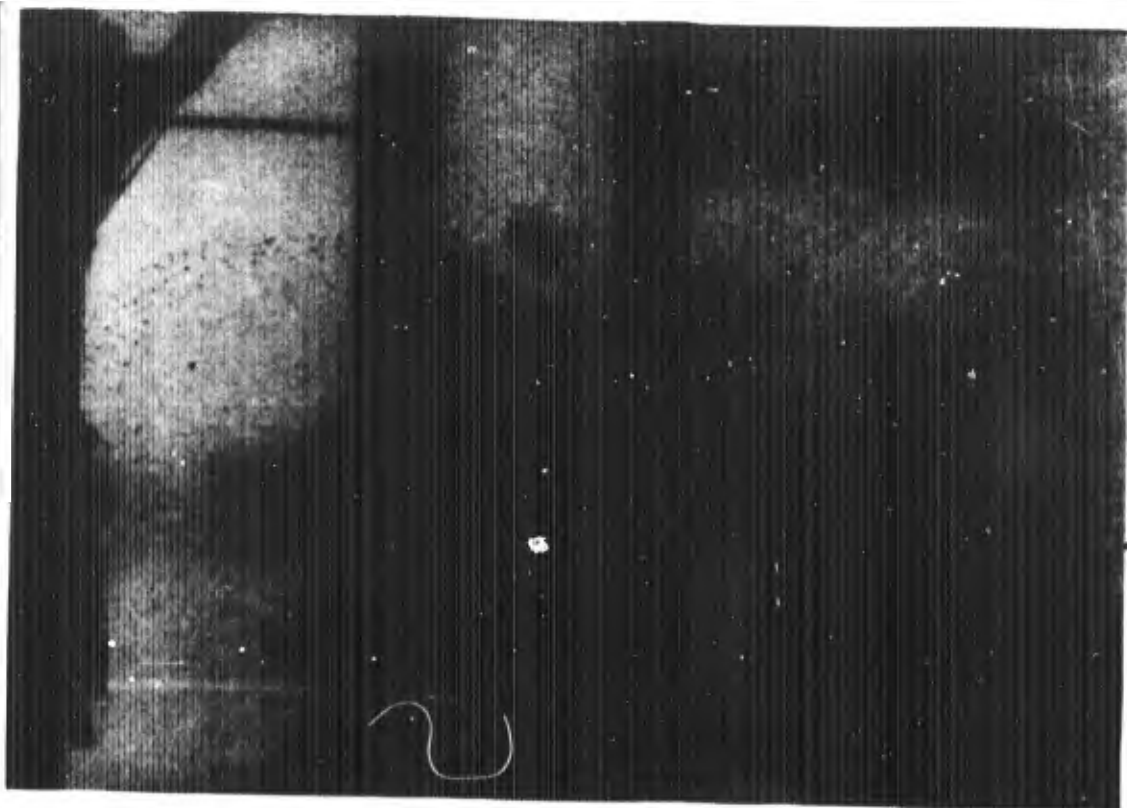Target Plates after AFML Shot# 2117
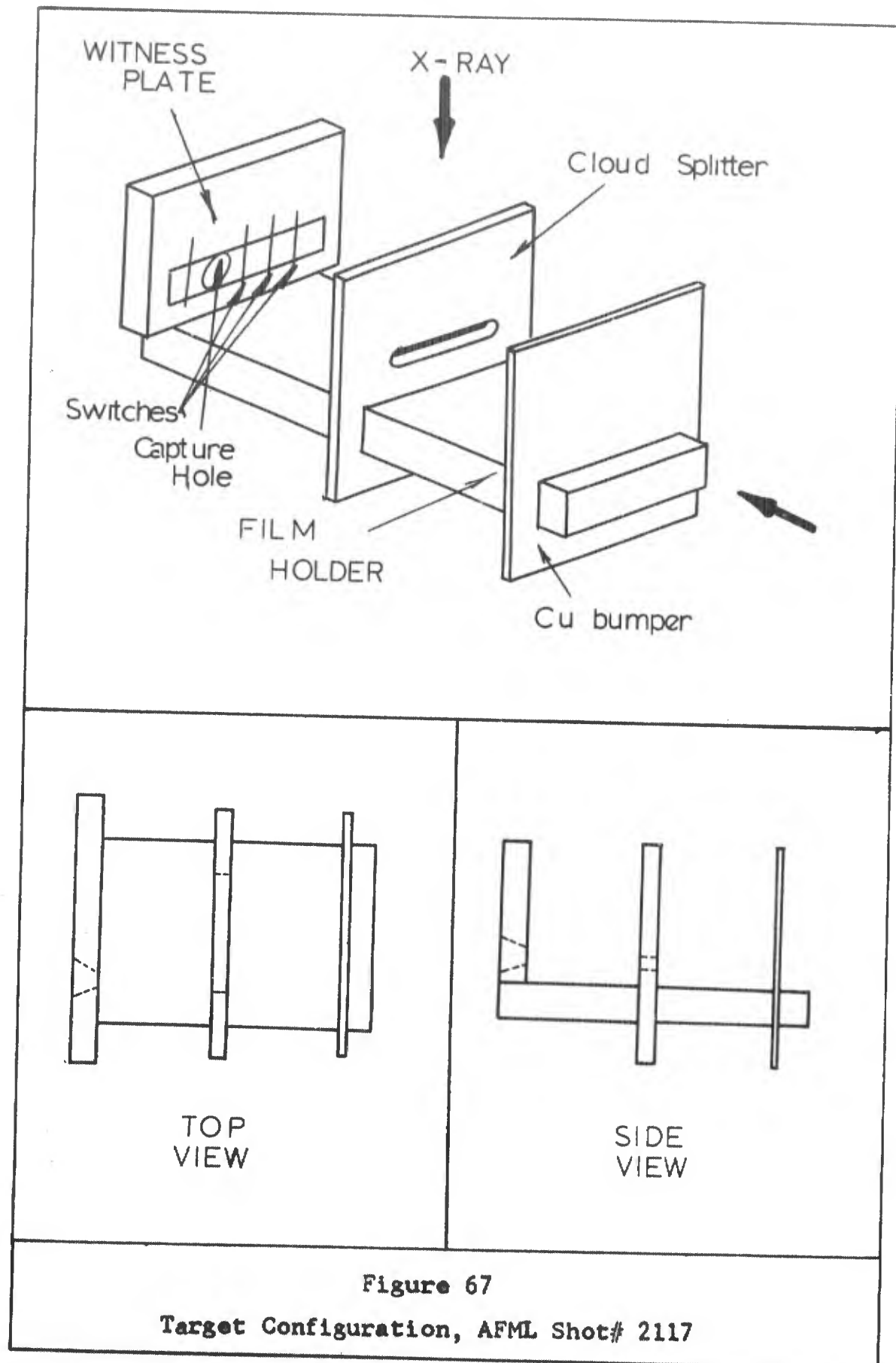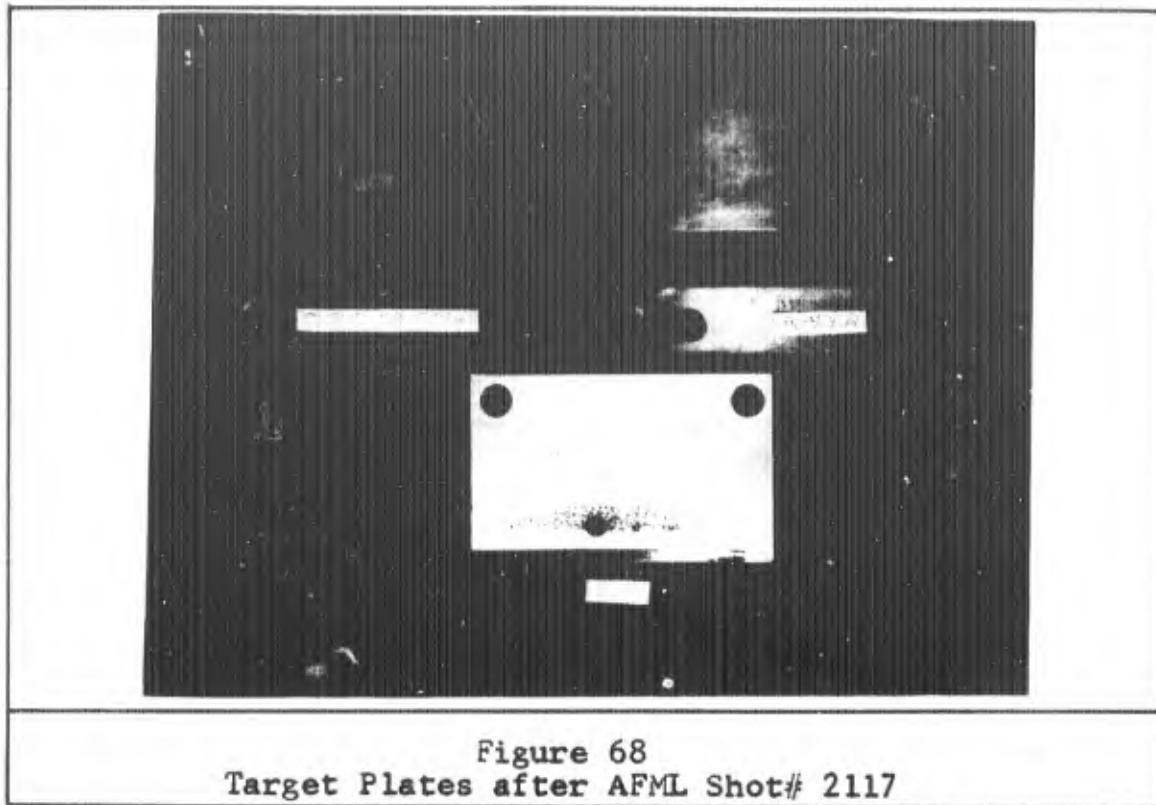
of the debris cloud. The interior of the cloud was seen to
be devoid of any solid or liquid particles. The thickness
of this hollow shell indicates that the cloud forming pro-
cess at any point along the bumper was over in a very short
time interval. In other words, no continuous feeding of
particles was seen to occur throughout bubble formation.
This suggested that the edge of the expanding bumper hole
was the source of the bumper debris particles. Four con-
tact switches were spaced as indicated in Figure 67. A
capture hole was drilled in the witness plate to allow
passage of cloud particles into various capture materials.
Bread, cotton, cloth, cotton batting, and styrofoam were
tried in similar arrangements. No cloud particles were
recovered. Evidence was recorded that impact with the

capture material did occur, but only on the topmost surface. Meanwhile, the aluminum witness plate adjacent to the hole was heavily pitted by the same cloud. The X-ray was triggered by the contact switch on the cloud axis. This switch and the three others were connected to the xenon flash tubes. Times of arrival of the first particles at each location were accurately recorded, but the exact distance traveled by that same particle was indeterminable. Calculations of cloud front velocity by this technique are therefore inaccurate.

AFML Shot 2125 (Figures 69, 70, 71).

A 1/8" cadmium sphere impacted a 1/32" cadmium sheet at 22,756 ft/sec. The shot objective was to X-ray the gaseous cloud and note the damage caused on a witness plate. Projectile and bumper material was cadmium. No cratering of the aluminum witness plate occurred, but it did experience severe deformation and heating. Cadmium film was coated on the surface of the plate. This was probably cadmium oxide, judging from its brownish color, but no characterization was attempted. The important thing noted was that energy was delivered to the witness plate, even though cratering did not take place. The plate was deformed in the central region with such force that it rebounded from the backup plate 1" away (see Figure 70). No attempt was made to measure energy delivered by gaseous phases to witness plates.
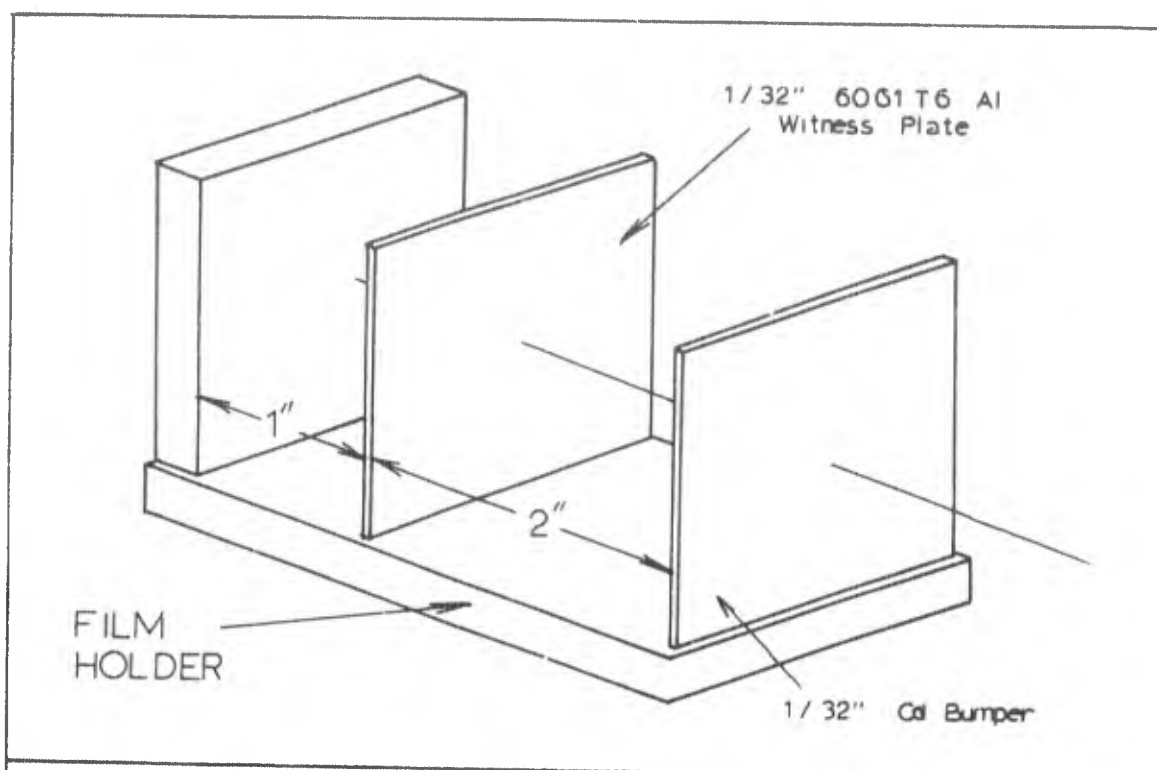
Figure 69

Target Geometry, AFML Shot# 2125
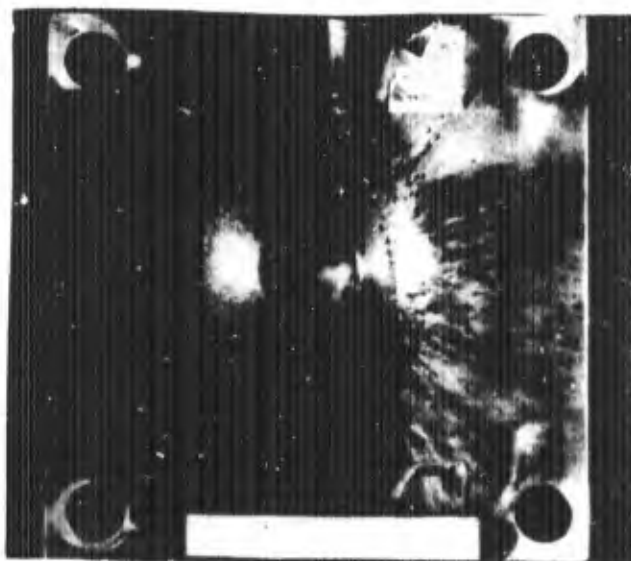
FRONT VIEW
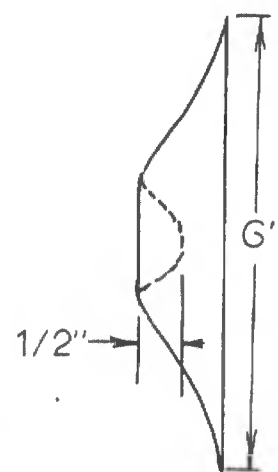
EDGE VIEW

Figure 70

Witness Plate Damaged by Gaseous Cadmium
AFML Shot# 2125

Figure 71
Radiograph of AFML Shot# 2125
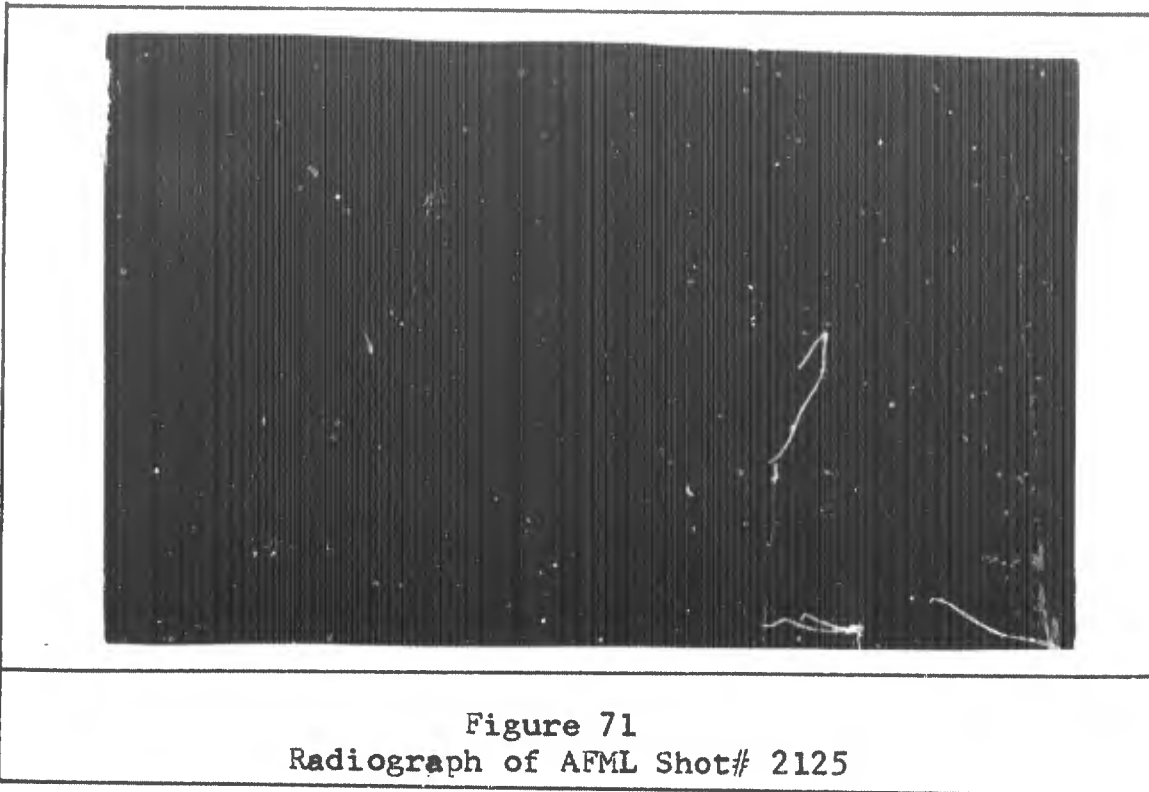
AFML Shot 2190 (Figures 72 and 73).

A 1/8" steel sphere impacted a 1/32" steel bumper at 21,260 ft/sec. This shot combined many promising techniques that were planned for inclusion in the final test series. The bumper was a 1½" by 6" plate to minimize its X-ray silhouette. The two side windows were replaced with 1" thick plexiglas ports so that the experiment could be viewed optically. The debris cloud was to pass over a cloud splitter which would remove the lower half of the debris cloud and enable a picture to be taken for gas cloud detection purposes. The remaining upper half of the cloud would proceed on to a 1/8" thick steel witness plate. Half of this plate had been cut away to permit 1/4 of the cloud to enter a container filled with capture material. Two
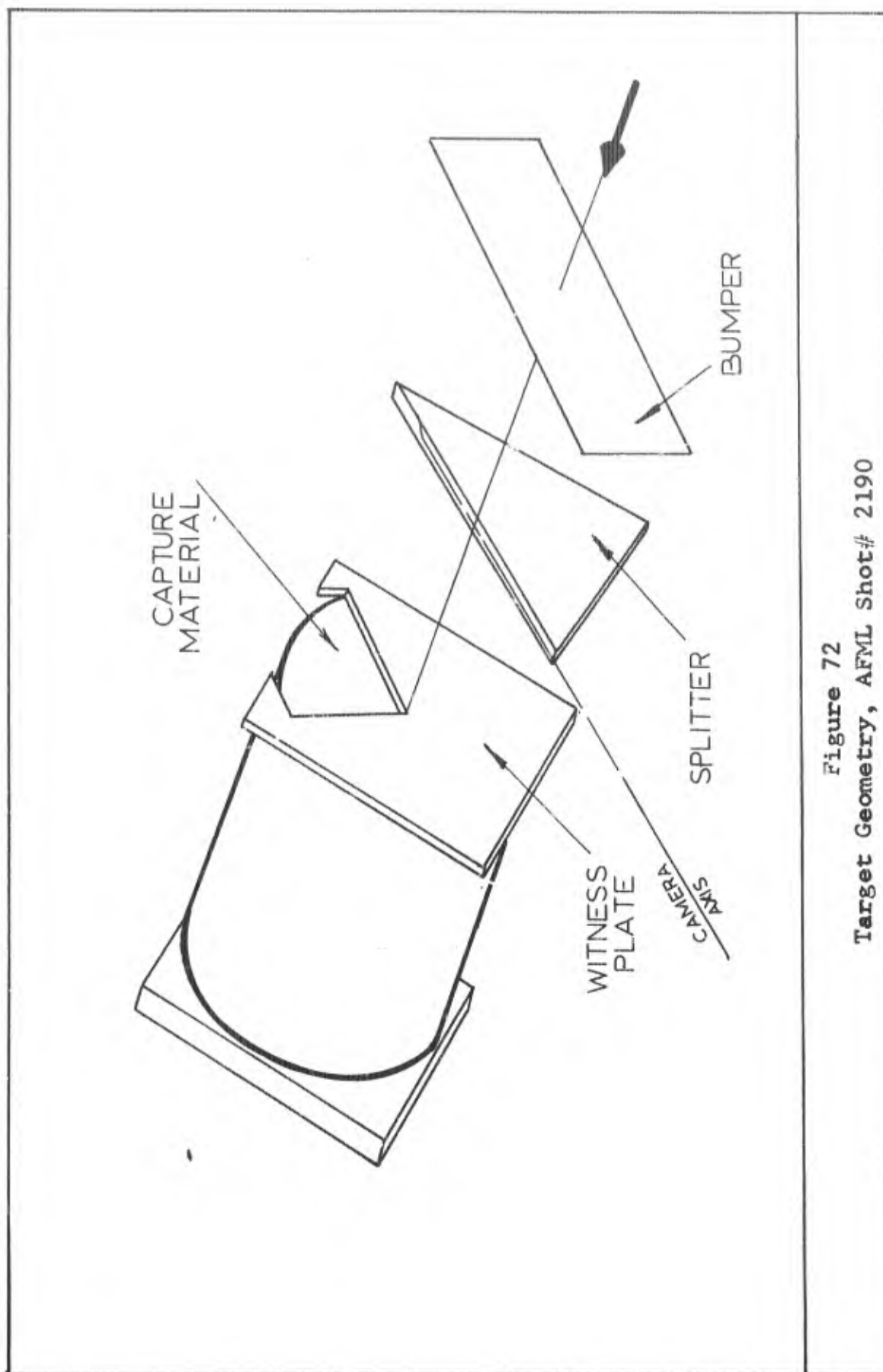
Figure 72
Target Geometry, AFML Shot# 2190

capture materials, shaving cream and meringue, were thought
to be promising because of their low densities.

In this experiment one-half of the opening was covered
by a meringue mixture, 1" thick in an aluminum foil pie
mold. The remainder of the can was then filled with sha-
ving cream dispensed from a can. The shaving cream,
Gillette Foamy (Regular), has a mean density of 0.0618 g/
cc at atmospheric conditions, but was observed to expand
30 - 50 times its normal volume at 25mm Hg. The meringue
also expanded, but not more than 60%. The results of the
test are partially illustrated in Figure 73. Both the
cloud splitter and the witness plate were heavily cratered,
but no craters were observed in the bottom of the can.
Recovery of particles was not possible from either capture
material. The foil pie pan was ripped apart by the cloud,
but no particles were found in the meringue. All traces
of the shaving cream had disappeared, with only a dry,
hard, blackish residue remaining on the inner surface of
the can. No characterization of this residue was attempted.
At this point, further attempts to capture hypervelocity
particles intact were abandoned.

Figure 73
Radiograph of AFML Shot# 2190
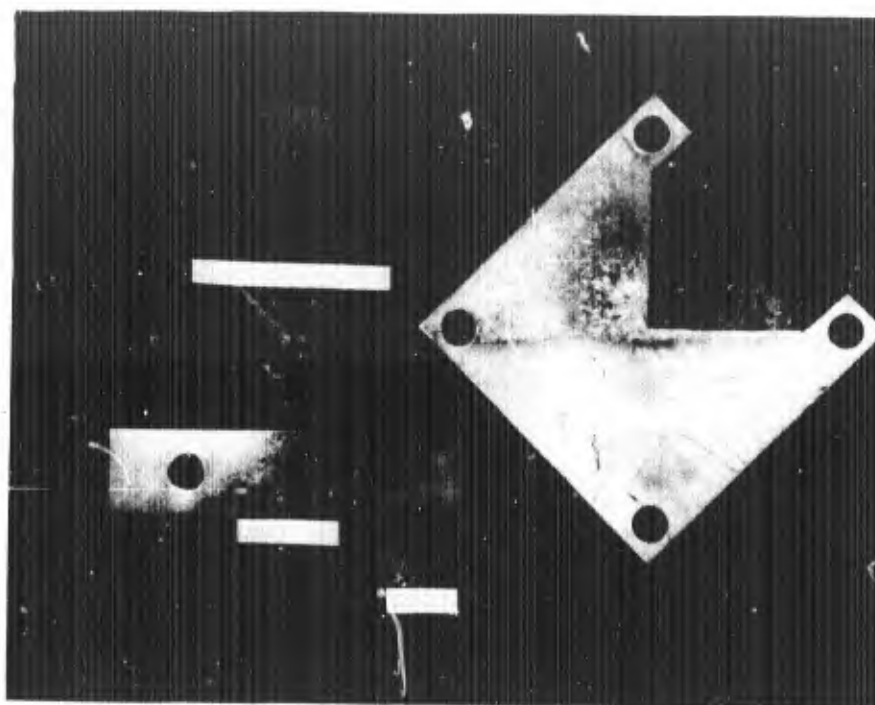
Figure 74
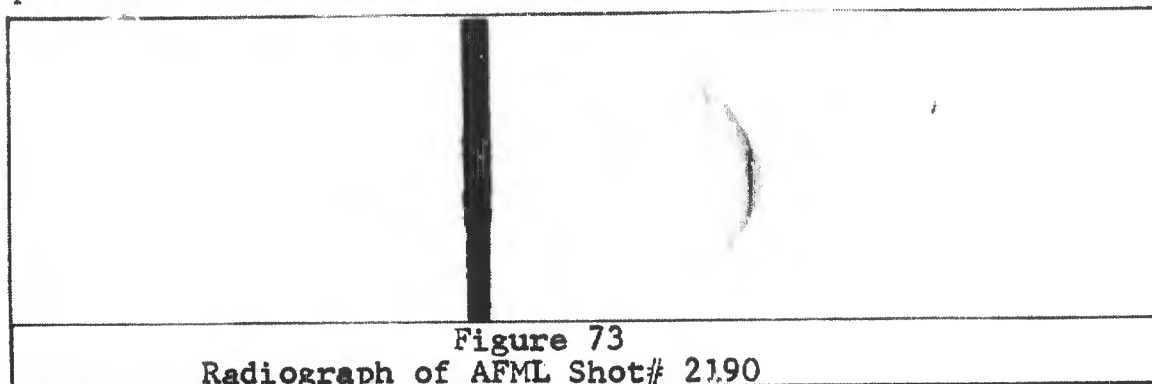Bumper and Witness Plates, AFML Shot# 2190

Appendix C

Specialized Measurements and Calculations

1. Drag Effects of Atmosphere

To determine the slowing effect of the test atmosphere (25mm Hg, 20° C), it was first necessary to calculate the ratio of the Mach number, M, to the Reynolds number, R.

$$M = \frac{V}{C} \qquad\qquad R = \rho \frac{V \ell}{\mu} \qquad\qquad \text{(C-1)}$$

where V = free stream velocity, ρ = density of the atmosphere, μ = viscosity, C = speed of sound in the fluid, and ℓ = characteristic dimension of the object moving through the fluid.

For $M \geqslant 10R$, the aerodynamic regime known as free molecular flow occurs. The mean free path of the gas molecules is much longer than the diameter of the particles. The slowing of cloud particles would be due to collisions of individual gas molecules with particles. The interval $10R > M \geqslant \sqrt{R}$ is called the transition zone. "Slip flow" occurs for $\sqrt{R} > M \geqslant 0.01 \sqrt{R}$. The mean free path of the molecules is small, but not negligible compared to particle diameters. For $M < 0.01 \sqrt{R}$ continuous flow occurs, and consideration must be made of aerodynamic

forces slowing individual particles (Ref 14:7-06).

To proceed with these calculations, several assumptions must be made. The smallest particle resolvable by the X ray was estimated to be 0.25 mm. If a cadmium-sphere of 0.25 mm diameter is considered departing the thin plate with initial velocity V = 7 km/sec, the following results:

$$M = \frac{V}{C} \qquad\qquad C = 49.1 \sqrt{T} \quad \text{for air} \quad (C-2)$$

(Ref 12:150)

where T is measured in degrees Rankine.

$$T = 68°F = 528°R$$
$$C = 49.1 \sqrt{528} = (49.1)(23) = 1130 \, ft/sec$$
$$V = 7 \frac{Km}{sec} \; 3281 \frac{ft}{Km} = 23,000 \, ft/sec$$
$$M = \frac{23000}{1130} = 20.18$$
$$R = \frac{\rho V \ell}{\mu}$$

Considering air as an ideal fluid, the equation of state is applied:

$$P = \rho RT$$
$$\rho = \frac{P}{RT} = \frac{25mm \; Hg \; \; 2.785 \, lb/ft^2/mm \, Hg}{1.715 \frac{ft\text{-}lb}{slug\text{-}°R} \quad 528°R}$$
$$= 7.72 \times 10^{-5} \, slug/ft^3$$
$$For \; T = 68°F, \; \mu = 3.8 \times 10^{-7} \, lb\text{-}sec/ft^2$$
$$= 3.8 \times 10^{-7} \, slug/ft \, sec$$

(Ref 14:6-06)

$$R = \frac{\left(7.72 \times 10^{-5} \frac{slug}{ft^3}\right)\left(23000 \frac{ft}{sec}\right)\left(.25mm\right)\left(3.3 \times 10^{-3} \frac{ft}{mm}\right)}{3.8 \times 10^{-7} \, slug / ft \, sec}$$

$$= 3840$$

$$\therefore M = 20.18 < \sqrt{R} = \sqrt{3840} = 62$$

Therefore, we were in the "slip flow" regime. To check this result, the mean free path of the gas molecules in the air was compared with the diameter of the spherical particle. The ratio of these numbers, K, called the Knudsen number, offered another means of separating flow regimes.

Knudsen #	Flow Regime
$1.0 < K$	free molecular flow
$0.1 < K \leqslant 1.0$	transition region
$0.01 < K \leqslant 0.1$	slip flow
$K \leqslant 0.01$	continuum flow

To determine the mean free path of the gas molecules in air, we note that air at standard conditions has a mean free path, λ, of approximately 10^{-5} cm.

Assuming the velocities of N_2 and O_2 molecules in air have Maxwellian distributions,

$$\lambda = \frac{0.707}{\sigma n} \qquad \text{(C-3)}$$

where $\sigma = 4\pi r^2$, n = $\dfrac{No.\ molecules}{cm^3}$, r = radius of molecule (cm). (Ref 15:72) For air at 68° F, 25 mm Hg, and using

$P = nkT$

$$n = \frac{P}{kT} = \frac{25\ mm\ Hg\ 2.785\ ^{lb/ft^2}\!/_{mm\ Hg}\ 47.88\ ^{n/m^2}\!/_{^{m^2}\!/_{lb/ft^2}}}{1.38 \times 10^{-23}\ n\text{-}m/^{\circ}K\ 293\ ^{\circ}K}$$

$$= \frac{33.3 \times 10^2}{405 \times 10^{-23}} = 8.23 \times 10^{23}\ \frac{molecules}{m^3}$$

$$= 8.23 \times 10^{17}\ \frac{molecules}{cm^3}$$

To simplify the calculations, the nitrogen molecules were assumed to make up 100 % of the air.

For nitrogen r = 1.85 x 10^{-8} cm

$$= 4\pi r^2 = 4.31 \times 10^{-15}\ cm^2$$

(Ref 15:74)

$$\lambda_{N_2} = \frac{0.707}{8.23 \times 10^{17}\ \dfrac{molecules}{cm^3}\ 4.31 \times 10^{-15}\ cm^2}$$

$$= 1.94 \times 10^{-4}\ cm$$

$$\therefore K = \frac{\lambda}{d} = \frac{1.94 \times 10^{-4}\ cm}{0.025\ cm} = 0.0076$$

This indicated the flow was continuous and aerodynamic drag forces must be considered. This regime will slow particles more than slip flow, so to be conservative, the calculations are based on continuum flow.

The work done by the atmosphere in slowing down a particle was:

$$W = \triangle KE = F_d \cdot D \tag{C-4}$$

where $\triangle KE$ is the change in kinetic energy, F_d is aero-dynamic drag force, and D is distance traveled.

$$F_d = \frac{C_D}{2} \rho A V^2 \tag{C-5}$$

where C_D is coefficient of drag, ρ is the medium density, A is cross sectional area of the particle, and V is the free stream velocity. C_D may be taken as 1 for a sphere at hypersonic speeds (Ref 25:11).

$$A = \pi \frac{d^2}{4} = \frac{3.14}{4}\left[(.25\, mm)\left(3.281 \times 10^{-4} \frac{ft}{mm}\right)\right]^2$$
$$= 6.43 \times 10^{-8}\, ft^2$$
$$F_d = 0.5\left(7.7 \times 10^{-5} \frac{slug}{ft^3}\right)\left(2.3 \times 10^4\right)\frac{ft^2}{sec^2}\, 6.43 \times 10^{-8}\, ft$$
$$= 203.5 \times 10^{-5}\, slug\, ft/sec^2$$
$$\triangle KE = F_d \cdot D = 203.5 \times 10^{-3}\, slug\, ft^2/sec^2$$

for a particle traveling 1 ft.

$$\triangle KE = \frac{m}{2}\left(V_I^2 - V_F^2\right) \tag{C-6}$$

where V_I is initial particle velocity, 23000 ft/sec, V_F is final particle velocity, and m is mass of particle (slugs).

$$m = \frac{4}{3}\pi r^3 \rho = 4.18 \left(8.64\,g/cm^3\right)\left(1.25\times10^{-2}\,cm\right)^3$$

$$= 4.18\left(1.96\times10^{-6}\,cm^3\right)\left(8.64\,g/cm^3\right)$$

$$= 70.7\times10^{-6}\,g \;\; \frac{2.21\,lb}{10^3\,g} \;\; \frac{slug}{32.2\,lb}$$

$$= \frac{155.5\times10^{-9}}{32.2} = 4.825\times10^{-9}\,slug$$

$$\Delta KE = \frac{4.825\times10^{-9}}{2}\,slug\left[\left(2.3\times10^4\right)^2 - V_F^2\right]\,ft^2/sec^2$$

$$= 2.035\times10^{-3}\,slug\;ft^2/sec^2$$

$$= 2.413\times10^{-9}\left[5.29\times10^8 - V_F^2\right]\,\frac{slug\;ft^2}{sec^2}$$

$$= 2.035\times10^{-3}\,slug\;ft^2/sec^2$$

$$5.29\times10^8 - V_F^2 = 8.46\times10^5\,ft^2/sec^2$$

$$V_F^2 = 5.28\times10^8\,ft^2/sec^2$$

$$V_F = 22,990\;ft/sec$$

The atmosphere slows the particle a negligible amount, so the assumption of constant velocity was justified.

2. Brinell Hardness Calculations

Readings were taken using a 500 kg load with a 10 mm diameter ball. The recorded diameters of impressions made in the Cu billet and plates respectively were 2.80 mm and 2.25 mm. The equation for Brinell hardness:

$$B_H = \frac{P}{\frac{\pi D}{2}\left(D - \sqrt{D^2 - d^2}\right)} \qquad (C\text{-}7)$$

where P is applied load (kg), D is diameter of ball (mm), and d is diameter of the impression in mm.

$$B_{H_{PLATE}} = \frac{500}{\frac{31.4}{2}\left(10 - \sqrt{100 - 5.107}\right)} = \frac{500}{4.06} \sim 123$$

Similarly B_H billet = 80

3. Measurement of Crater Volume, Depth, and Diameter

The faces of the thick targets were ground flat and parallel prior to the test series. The volumes of the craters formed during impact were determined by the following technique. A depth gauge was zeroed on the undisturbed billet material near the edge of the target. The arm of the depth gauge was swung away and penetration oil from a 10 ml burette was metered into the crater. The smallest controllable drop size was 0.01 ml. Volumes were deter-

mined when the point of the depth gauge just touched the top surface of the oil in the crater (see Figure 75).
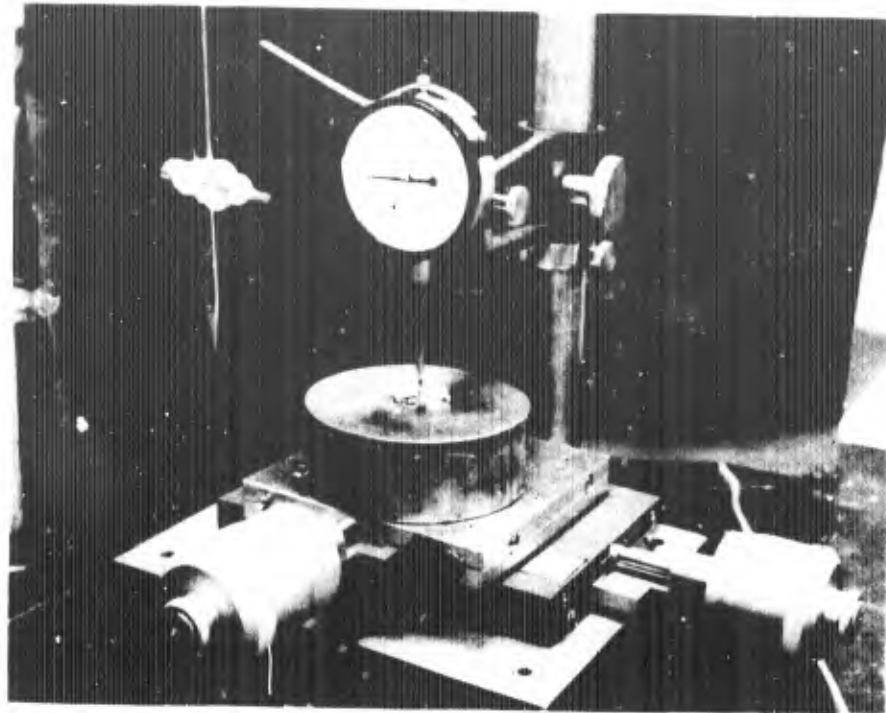
Figure 75
Crater Volume Measurement Technique for Thick Targets

The technique was calibrated by use of "standard" volumes drilled into three aluminum cylinders 1" in diameter and 1" in height.(see Figure 76). Nominal hole size was 1/2" D - 1/2" depth. Fifteen depth readings taken with the depth gauge were averaged to compute the actual depth. Hole diameters were measured with a ball gauge, the dimension of the gauge being taken with a micrometer. The volumes were computed using the measured depth and diameter. The volumes of these standards were then
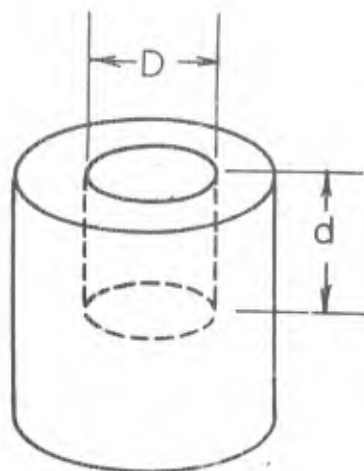
Figure 76
Standard Volume

measured using the penetrating oil technique. Three readings were taken of each standard volume and averaged. The results and accuracies are indicated in Table XXI.

Volume No.	Measured Diameter, D (in)	Measured Depth, d (in)	Calc. Volume cm^3	Measured Volume cm^3	error %
1	0.5006	0.4997	1.61	1.603	0.47%
2	0.5028	0.4998	1.62	1.607	1.16%
3	0.5006	0.4997	1.61	1.603	0.47%

Accuracy Determination of
Penetrating Oil Technique

Table XXI

The depths of the craters were measured using the depth gauge initially zeroed at the bottom of the crater. The needle was then placed at a point on the billet face near the edge of the target. The differential readings noted on the dial gave the crater depth.

The crater diameters were measured using the microscope on a Tektron Microtester. The microscope was focused on the billet surface near the edge. A calibrated traveling bed moved the crater under the microscope until the focal place was found inside the crater rim. After noting the position of the bed on the micrometer gauges, the billet was moved under the microscope by the traveling bed. When the focal plane was found at a point on the opposite rim, bed position was again recorded. The difference between the readings was the crater diameter.
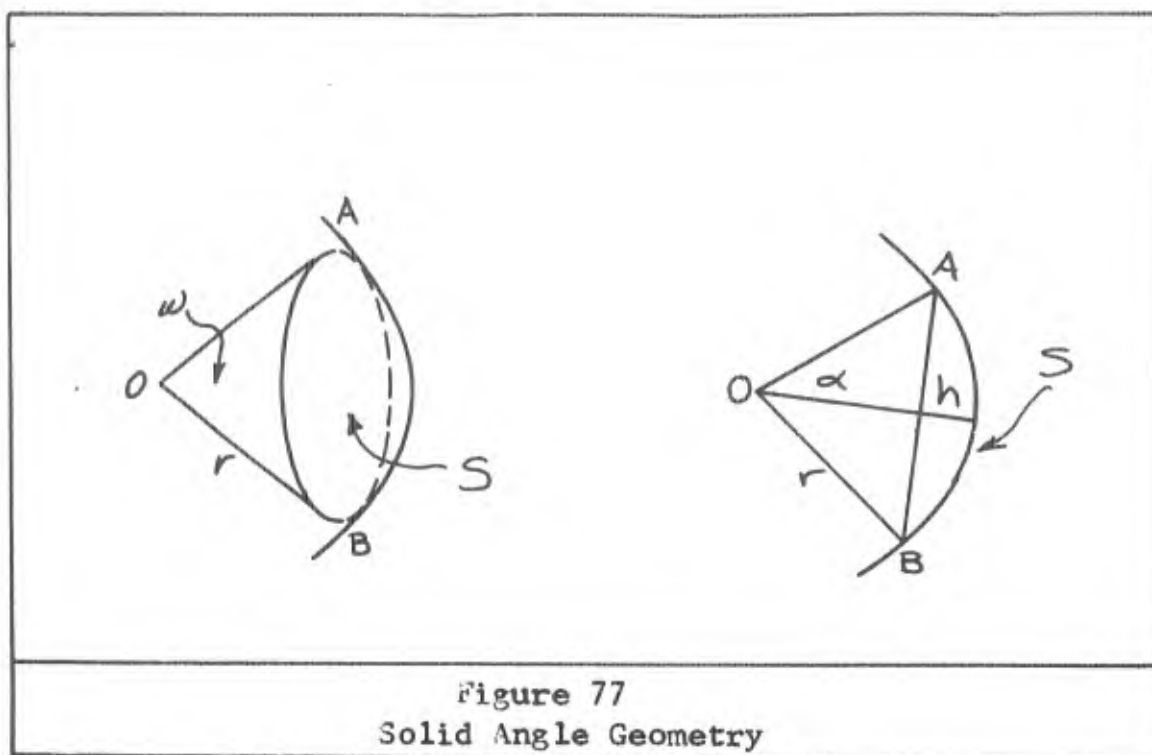
4. Conversion of Cone Angle $\propto$ to Steradians

One steradian is defined as the solid angle subtended by a surface on a unit sphere equal to the radius of the sphere squared. Consider the drawings below. The area S of the sphere subtending solid angle ω at O is given by

$$S = 2\pi r h \tag{C-8}$$

but $$h = r(1 - \cos \alpha) \tag{C-9}$$

115

therefore $\quad S = 2\pi r^2 \left(1 - \cos\alpha\right) \quad\quad$ (C-10)

Figure 77
Solid Angle Geometry

To convert to steradians, divide by r^2.

$$\omega = 2\pi \left(1 - \cos\alpha\right) \quad\quad\quad \text{(C-11)}$$

This function is plotted in Figure 78.

5. <u>Graphical Method of Determining Impact Velocity and Pressures</u>

The graph shown in Figure 79 was used to determine impact velocities and peak pressures. For example, Table I lists 0.8 Mb as the minimum peak pressure required to vaporize cadmium. This pressure is normalized by dividing by the characteristic pressure C_0^2/V_0 for cadmium, which is 0.515 Mb. The resulting normalized pressure is 1.55.

Figure 78
Solid Angle vs Cone Angle
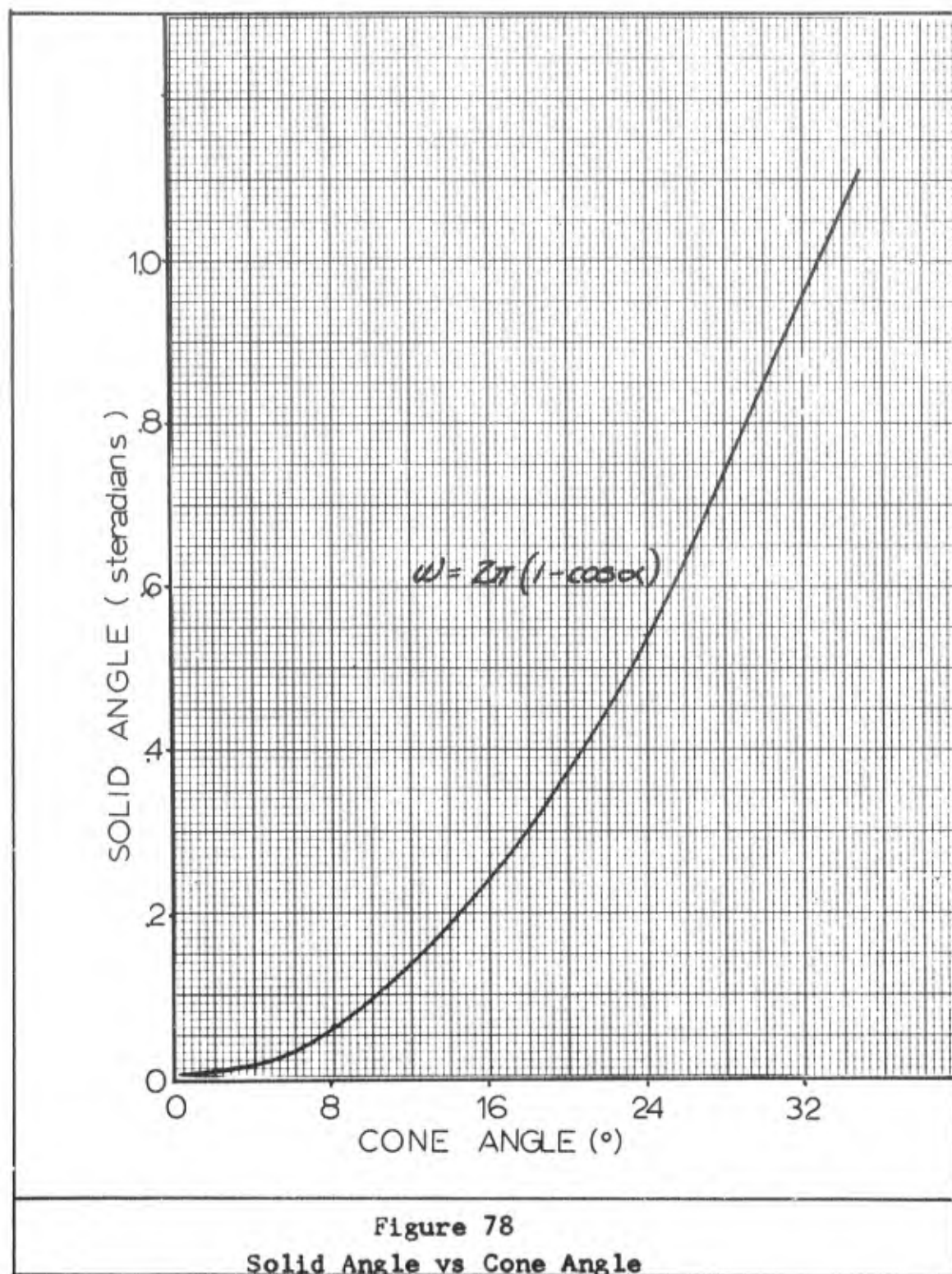
The intersection of the K = 1.67 and the 1.55 normalized
pressure line occurs at a normalized mass velocity of 0.7.
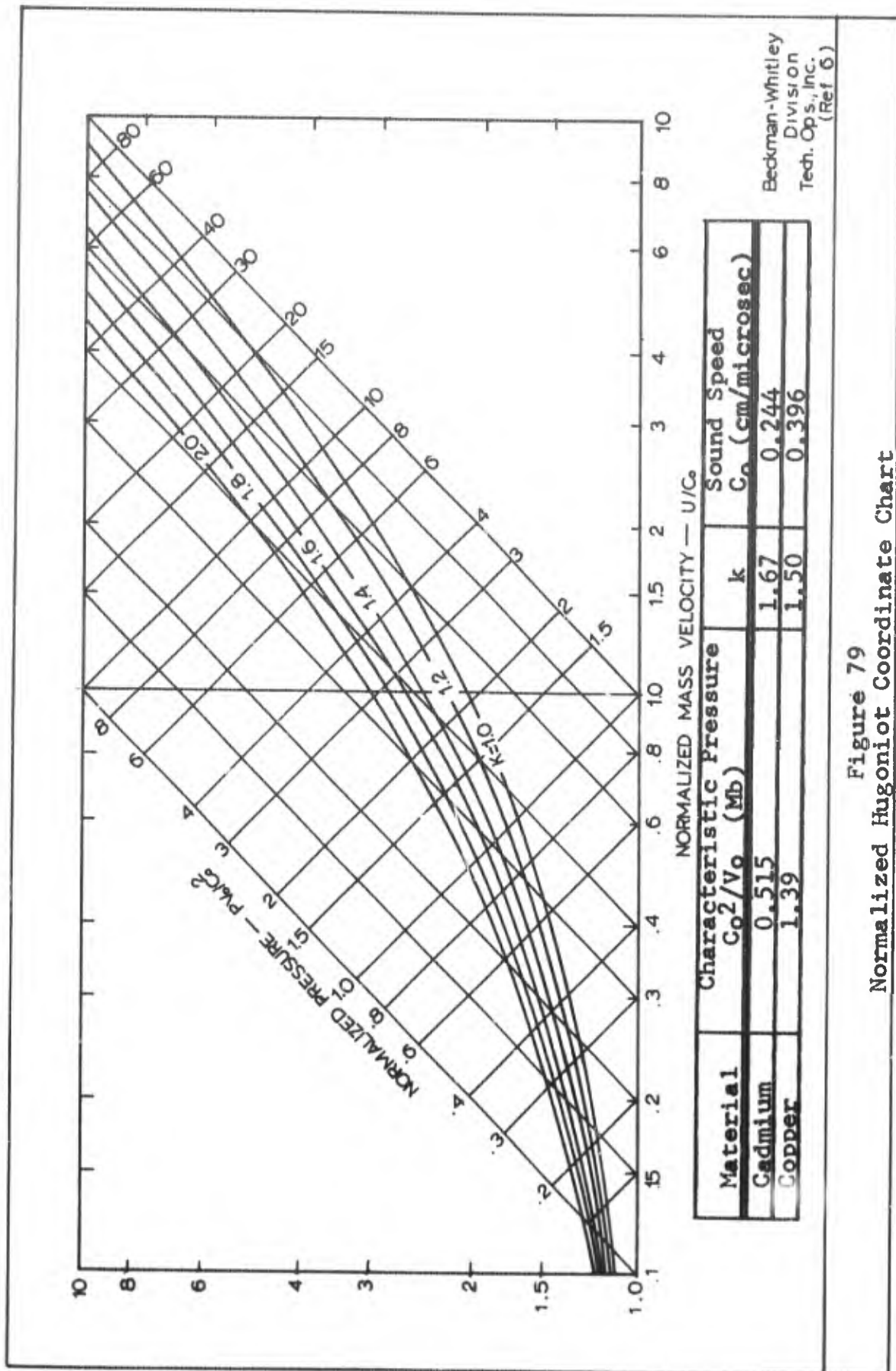Multiplying 0.7 by the sound speed C_O of cadmium gives a

117

Figure 79

Normalized Hugoniot Coordinate Chart

GSF/Mech 67-1

product of 0.17 cm/microseconds = 1.7 km/sec. But the
impact velocity for like materials is double the mass
velocity (Ref 27:9), so 3.4 km/sec impact velocities are
required to vaporize cadmium.

If the impact velocity is known, the peak pressures
generated may be computed. Copper impacting copper at
23,000 ft/sec (7 km/sec) causes mass velocities to reach
3.5 km/sec. Dividing this velocity by C_O for copper results
in a normalized mass velocity for the impact of 0.884. The
intersection of the K = 1.50 line and the normalized mass
velocity = 0.994 occurs at a normalized pressure value of
2.0. Multiplying this pressure by the characteristic
pressure 1.39 gives a product of 2.78 Mb. Since complete
melting occurs at 1.84 Mb, it is doubtful if vaporization
of copper occurs at 2.78 Mb. No data was available to
confirm this. The velocities computed using the pressures
from Table I are in good agreement.

Appendix D

Bumpers and Witness Plates Used
in the Debris Cloud Study

Figures 80 through 85 are photographs taken of the bumpers and witness plates. The right side plates are in the center of each photograph, the left plates on the bottom. The single plate below the bumper was placed just above the slot on the splitter plate. Since these plates were close to the bumper (1.315"), considerable overlapping of craters precluded any analysis of individual craters. Closeups of these plates are shown in Figure 86 and 87.

Figure 80
Bumper and Witness Plates, AFML Shot# 2209
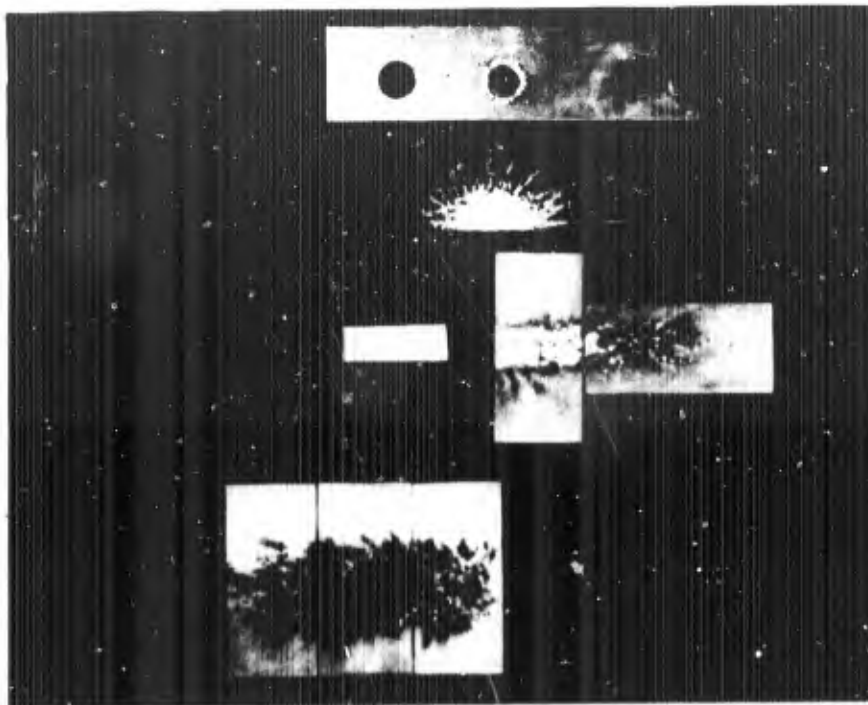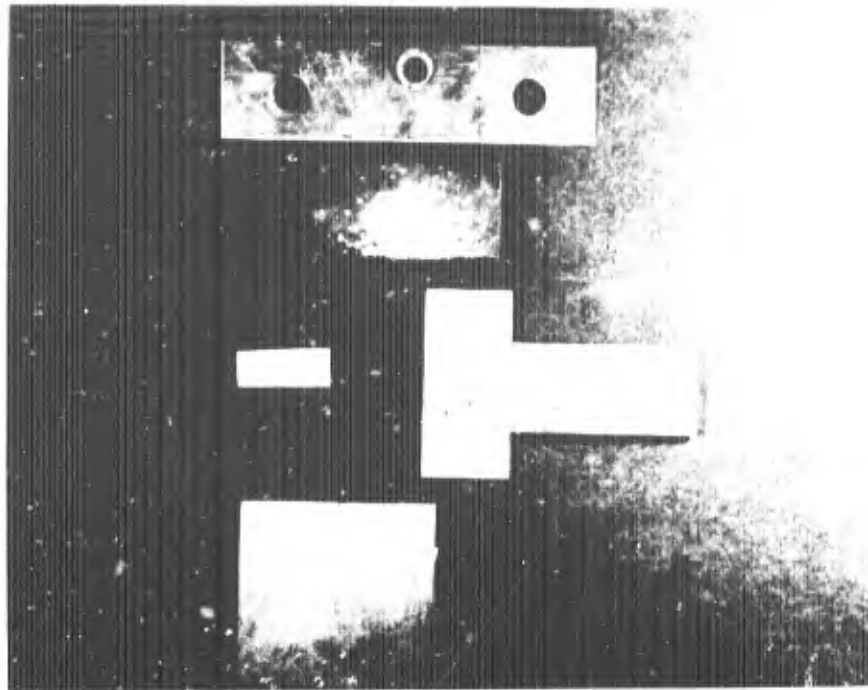
Figure 81
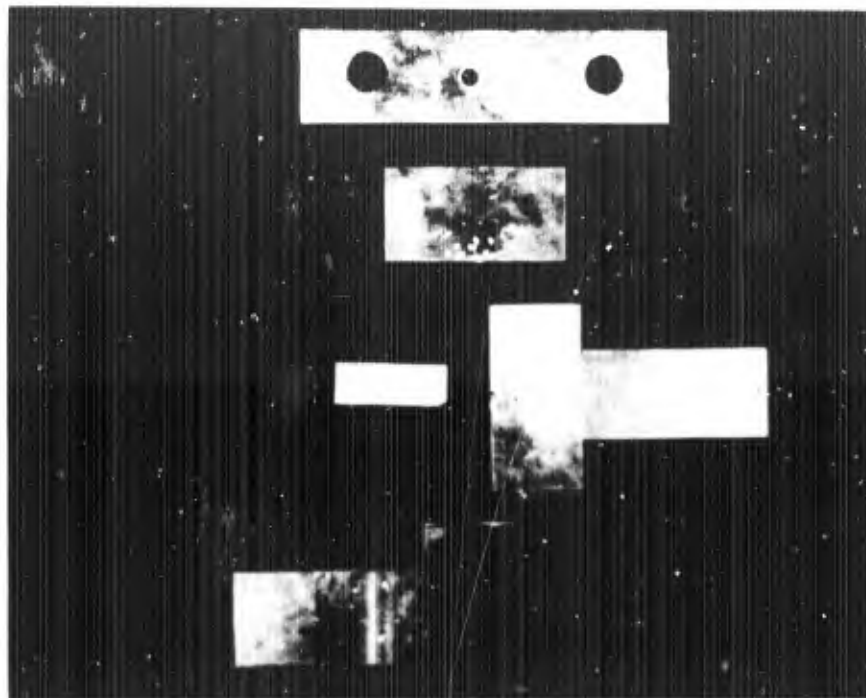Bumper and Witness Plates, AFML Shot# 2205

Figure 82
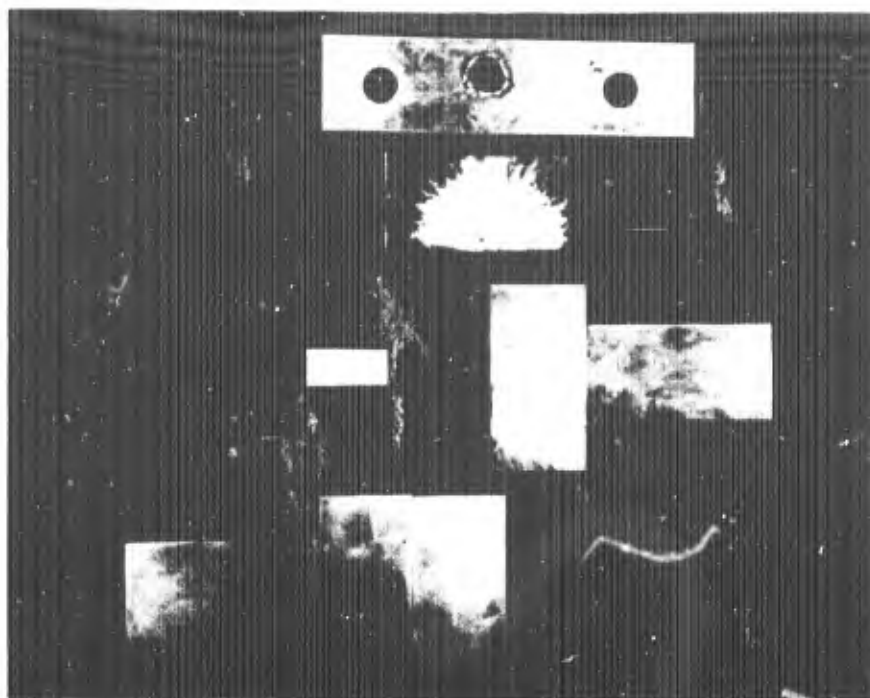Bumper and Witness Plates, AFML Shot# 1022

Figure 83
Bumper and Witness Plates, AFML Shot# 2199
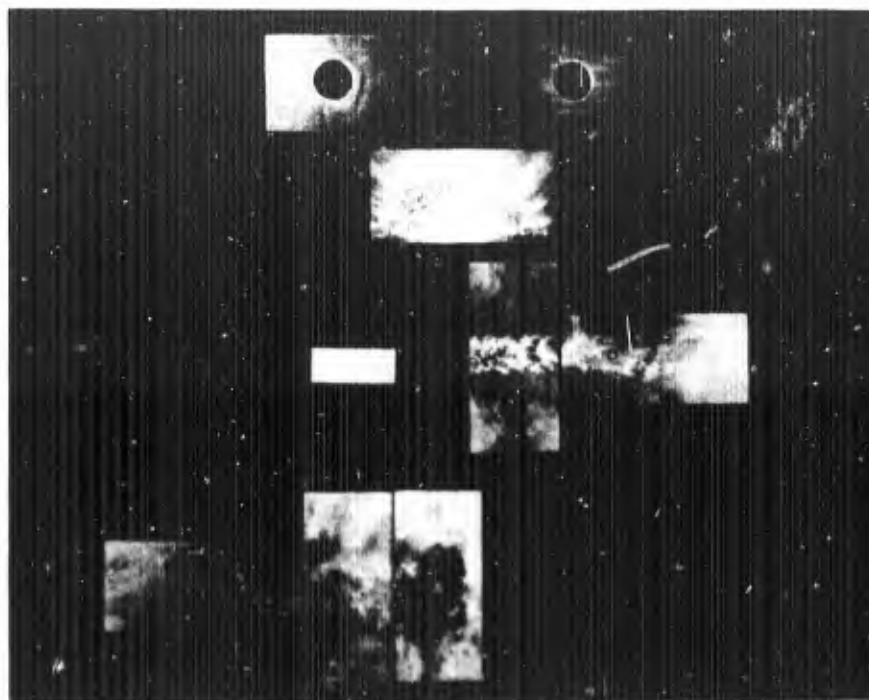
Figure 84
Bumper and Witness Plates, AFML Shot# 2214
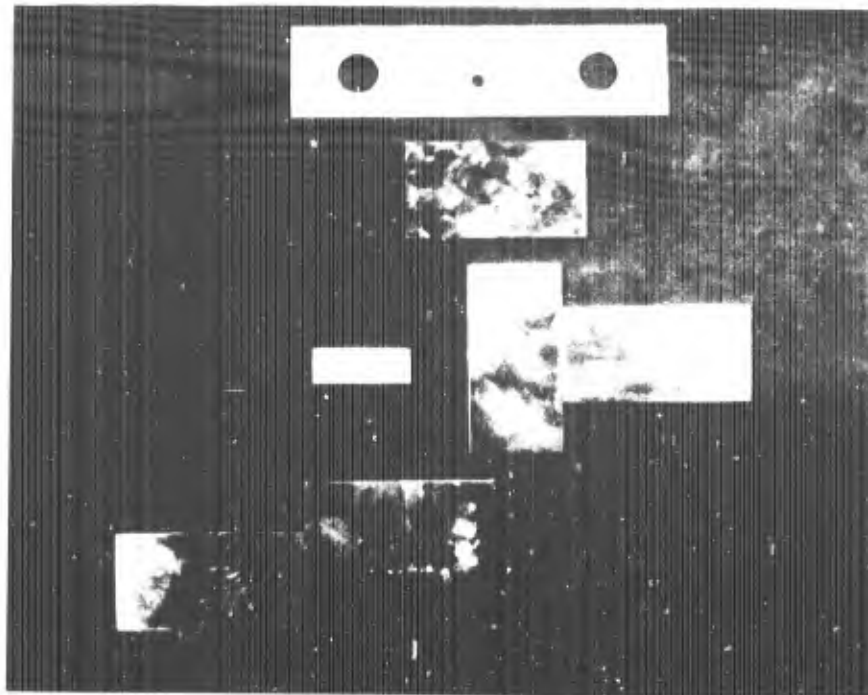
Figure 85
Bumper and Witness Plates, AFML Shot# 1026
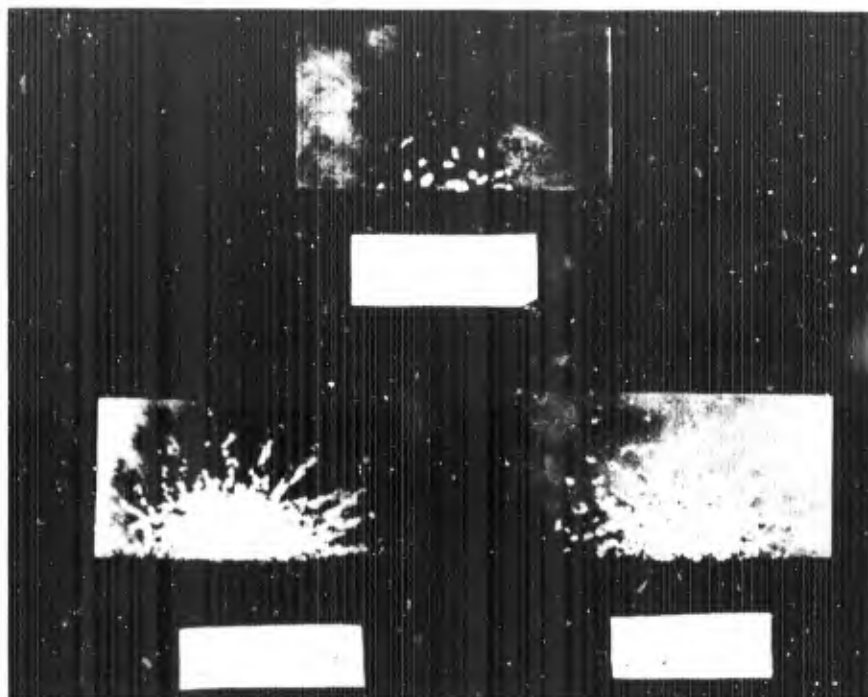
Figure 86
Witness Plates Used in Copper Bumper Tests
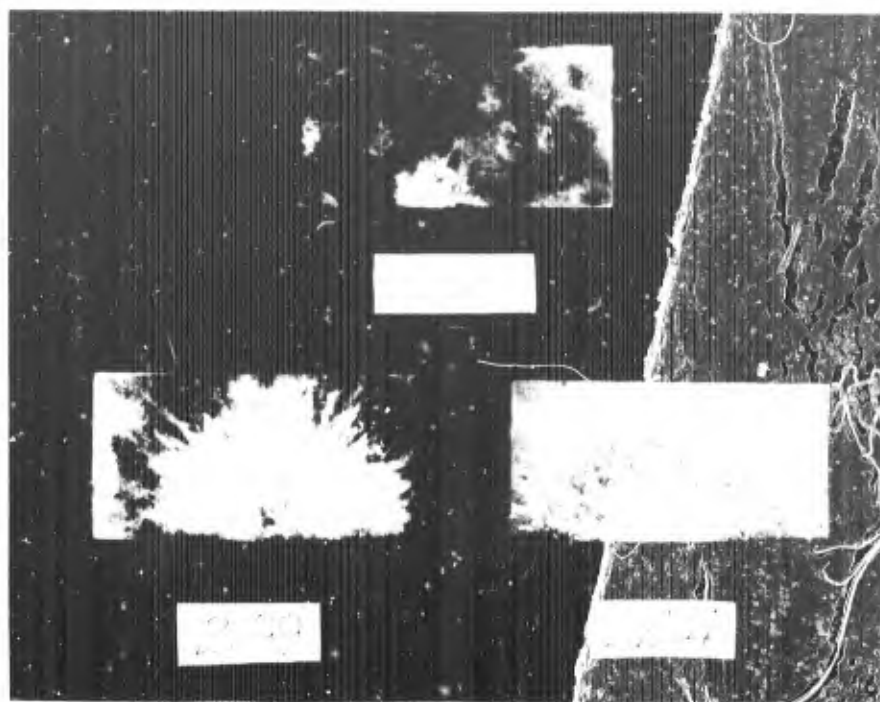
Figure 87
Witness Plates Used in Cadmium Bumper Tests

Vita

Donald Albert Carey was born on ██████████ ████ in Enid, Oklahoma. After completing his work in 1957 at Enid High School, he enrolled at the University of Oklahoma, Norman, Oklahoma. In June 1959, he entered the United States Air Force Academy and graduated in 1963 with a Bachelor of Science degree in Engineering Science. His military assignments include duty as Construction Engineer for the 6595th Aerospace Test Wing and the Air Force Western Test Range, Vandenberg AFB, California. He entered the Air Force Institute of Technology in June 1965.

Permanent address: ████████████████
████████████

This thesis was typed by Christa Carey

DOCUMENT CONTROL DATA - R & D

(Security classification of title, body of abstract and indexing annotation must be entered when the overall report is classified)

1. ORIGINATING ACTIVITY (Corporate author)	2a. REPORT SECURITY CLASSIFICATION
Air Force Institute of Technology (AFIT-SE) Wright-Patterson AFB, Ohio 45433	Unclassified
	2b. GROUP

3. REPORT TITLE

An Investigation of the Debris Cloud Produced by the Impact of Spheres on Thin Metal Sheets

4. DESCRIPTIVE NOTES *(Type of report and inclusive dates)*

AFIT Thesis

5. AUTHOR(S) *(First name, middle initial, last name)*

Carey, Donald A., Captain, USAF

6. REPORT DATE	7a. TOTAL NO. OF PAGES	7b. NO. OF REFS
May 1967	125	27

8a. CONTRACT OR GRANT NO. n/a	9a. ORIGINATOR'S REPORT NUMBER(S)
b. PROJECT NO. n/a	AFIT Thesis GSF/Mech 67-1
c.	9b. OTHER REPORT NO(S) *(Any other numbers that may be assigned this report)*
d.	n/a

10. DISTRIBUTION STATEMENT This document is subject to special export controls and each transmittal to foreign governments or foreign nationals may be made only with prior approval of the Dean, School of Engineering, Air Force Institute of Technology,(AFIT-SE), Wright-Patterson Air Force Base, Ohio 45433.

11. SUPPLEMENTARY NOTES	12. SPONSORING MILITARY ACTIVITY
	Air Force Materials Laboratory Wright-Patterson AFB, Ohio 45433

13. ABSTRACT

An experimental investigation of the debris cloud produced by the impact of 1/8" diameter spheres of copper and cadmium on 1/16" sheets of like materials was conducted. Calculations of the energy delivered to copper witness plates by solid and liquid phases of the debris cloud were made using volume-energy relationships. Velocity of the cloud front was determined through use of sequential flash X-rays. Phases of the cloud were determined by employing a combination of photographic, radiographic, and crater measurement techniques. Variations in the phase of the cloud with three selected velocities for each bumper-projectile combination were compared with the predicted phase in the velocity range of 23000 to 3000 ft/sec. Energy, energy density, momentum, and mass delivered to witness plates are determined as a function of cone angle...

DD FORM 1 NOV 65 **1473**

14. KEY WORDS	LINK A		LINK B		LINK C	
	ROLE	WT	ROLE	WT	ROLE	WT
Impact						
Hypervelocity Impact						

INSTRUCTIONS TO FILL OUT DD FORM 1473 - DOCUMENT CONTROL DATA
(See ASPR 4-211)

1. ORIGINATING ACTIVITY: Enter the name and address of the contractor, subcontractor, grantee, Department of Defense activity or other organization (corporate author) issuing the report.

2a. REPORT SECURITY CLASSIFICATION: Enter the overall security classification of the report. Indicate whether "Restricted Data" is included. Marking is to be in accordance with appropriate security regulations.

2b. GROUP: Automatic downgrading is specified in DoD directive 5200.10 and Armed Forces Industrial Security Manual. Enter the group number. Also, when applicable, show that optional markings have been used for Group 3 and Group 4 as authorized.

3. REPORT TITLE: Enter the complete report title in all capital letters. Titles in all cases should be unclassified. If a meaningful title cannot be selected without classification, show title classification in all capitals in parenthesis immediately following the title.

4. DESCRIPTIVE NOTES: If appropriate, enter the type of report, e.g., interim, progress, summary, annual, or final. Give the inclusive dates when a specific reporting period is covered.

5. AUTHOR(S): Enter the name(s) of the author(s) in normal order, e.g., full first name, middle initial, last name. If military, show grade and branch of service. The name of the principal author is a minimum requirement.

6. REPORT DATE: Enter the date of the report as day, month, year; or month, year. If more than one date appears on the report, use date of publication.

7a. TOTAL NUMBER OF PAGES: The total page count should follow normal pagination procedures, i.e., enter the number of pages containing information.

7b. NUMBER OF REFERENCES: Enter the total number of references cited in the report.

8a. CONTRACT OR GRANT NUMBER: If appropriate, enter the applicable number of the contract or grant under which the report was written.

8b, 8c, and 8d. PROJECT NUMBER: Enter the appropriate military department identification, such as project number, task area number, systems numbers, work unit number, etc.

9a. ORIGINATOR'S REPORT NUMBER(S): Enter the official report number by which the document will be identified and controlled by the originating activity. This number must be unique to this report.

9b. OTHER REPORT NUMBER(S): If the report has been assigned any other report numbers (either by the originator or by the sponsor), also enter this number(s).

10. DISTRIBUTION STATEMENT: Enter the one distribution statement pertaining to the report.

Contractor-Imposed Distribution Statement

The Armed Services Procurement Regulations (ASPR) para 9-203 stipulates that each piece of data to which limited rights are to be asserted must be marked with the following legend:

"Furnished under United States Government Contract No._____ . Shall not be either released outside the Government, or used, duplicated, or disclosed in whole or in part for manufacture or procurement, without the written permission of _____ , except for:
(i) emergency repair or overhaul work by or for the Government, where the item or process concerned is not otherwise reasonably available to enable timely performance of the work, or (ii) release to a foreign government, as the interests of the United States may require, provided that in either case the release, use, duplication or disclosure hereof shall be subject to the foregoing limitations. This legend shall be marked on any reproduction hereof in whole or in part."

If the above statement is to be used on this form, enter the following abbreviated statement:

"Furnished under U. S. Government Contract No._____ . Shall not be either released outside the Government, or used, duplicated, or disclosed in whole or in part for manufacture or procurement, without the written permission of_____ , per ASPR 9-203."

DoD Imposed Distribution Statements (reference DoD Directive 5200.20) "Distribution Statements (Other than Security) on Technical Documents," March 29, 1965.

STATEMENT NO. 1 - Distribution of this document is unlimited.

STATEMENT NO. 2 (UNCLASSIFIED document) - This document is subject to special export controls and each transmittal to foreign governments or foreign nationals may be made only with prior approval of (fill in controlling DoD office).

(CLASSIFIED document) - In addition to security requirements which must be met, this document is subject to special export controls and each transmittal to foreign governments or foreign nationals may be made only with prior approval (fill in controlling DoD Office).

STATEMENT NO. 3 (UNCLASSIFIED document) - Each transmittal of this document outside the agencies of the U. S. Government must have prior approval of (fill in controlling DoD Office).

(CLASSIFIED document) - In addition to security requirements which apply to this document and must be met, each transmittal outside the agencies of the U. S. Government must have prior approval of (fill in controlling DoD Office).

STATEMENT NO. 4 (UNCLASSIFIED document) - Each transmittal of this document outside the Department of Defense must have prior approval of (fill in controlling DoD Office).

(CLASSIFIED document) - In addition to security requirements which apply to this document and must be met, each transmittal outside the Department of Defense must have prior approval of (fill in controlling DoD Office).

STATEMENT NO. 5 (UNCLASSIFIED document) - This document may be further distributed by any holder only with specific prior approval of (fill in controlling DoD Office).

(CLASSIFIED document) - In addition to security requirements which apply to this document and must be met, it may be further distributed by the holder ONLY with specific prior approval of (fill in controlling DoD Office).

11. SUPPLEMENTARY NOTES: Use for additional explanatory notes.

12. SPONSORING MILITARY ACTIVITY: Enter the name of the departmental project office or laboratory sponsoring (paying for) the research and development. Include address.

13. ABSTRACT: Enter an abstract giving a brief and factual summary of the document indicative of the report, even though it may also appear elsewhere in the body of the technical report. If additional space is required, a continuation sheet shall be attached.

It is highly desirable that the abstract of classified reports be unclassified. Each paragraph of the abstract shall end with an indication of the military security classification of the information in the paragraph, represented as (TS), (S), (C), or (U).

There is no limitation on the length of the abstract. However, the suggested length is from 150 to 225 words.

14. KEY WORDS: Key words are technically meaningful terms or short phrases that characterize a report and may be used as index entries for cataloging the report. Key words must be selected so that no security classification is required. Identifiers, such as equipment model designation, trade name, military project code name, geographic location, may be used as key words but will be followed by an indication of technical context. The assignment of links, roles, and weights is optional.